

Physically-Based Simulation of Ice Formation

by
Theodore Won-Hyung Kim

A dissertation submitted to the faculty of the University of North Carolina at Chapel Hill in partial fulfillment of the requirements for the degree of Doctor of Philosophy in the Department of Computer Science.

Chapel Hill
2006

Approved by
Advisor: Ming C. Lin
Reader: Mark Foskey
Reader: Anselmo Lastra
Reader: David Adalsteinsson
Reader: Dinesh Manocha

ABSTRACT

THEODORE WON-HYUNG KIM: Physically-Based Simulation of Ice Formation.

(Under the direction of Ming C. Lin.)

The geometric and optical complexity of ice has been a constant source of wonder and inspiration for scientists and artists. It is a defining seasonal characteristic, so modeling it convincingly is a crucial component of any synthetic winter scene. Like wind and fire, it is also considered elemental, so it has found considerable use as a dramatic tool in visual effects. However, its complex appearance makes it difficult for an artist to model by hand, so physically-based simulation methods are necessary.

In this dissertation, I present several methods for visually simulating ice formation. A general description of ice formation has been known for over a hundred years and is referred to as the *Stefan Problem*. There is no known general solution to the Stefan Problem, but several numerical methods have successfully simulated many of its features. I will focus on three such methods in this dissertation: phase field methods, diffusion limited aggregation, and level set methods.

Many different variants of the Stefan problem exist, and each presents unique challenges. Phase field methods excel at simulating the Stefan problem *with surface tension anisotropy*. Surface tension gives snowflakes their characteristic six arms, so phase field methods provide a way of simulating medium scale detail such as frost and snowflakes. However, phase field methods track the ice as an implicit surface, so it tends to smear away small-scale detail. In order to restore this detail, I present a hybrid method that combines phase fields with diffusion limited aggregation (DLA). DLA is a fractal growth algorithm that simulates the *quasi-steady state, zero surface tension* Stefan problem, and does not suffer from smearing problems. I demonstrate that combining these two algorithms can produce visual features that neither method could capture alone.

Finally, I present a method of simulating icicle formation. Icicle formation corresponds to the *thin-film, quasi-steady state* Stefan problem, and neither phase fields nor

DLA are directly applicable. I instead use level set methods, an alternate implicit front tracking strategy. I derive the necessary velocity equations for level set simulation, and also propose an efficient method of simulating ripple formation across the surface of the icicles.

ACKNOWLEDGMENTS

First, I want to thank my advisor, Ming Lin. If not for her physically-based modeling course, I would not have found the seed of an idea that was later expanded into this dissertation, and if not for her subsequent patience and support, I would not have been able to develop and expand these ideas into their current form. Without her, this dissertation would simply not exist. I would also like to thank all of my committee members, David Adalsteinsson, Mark Foskey, Anselmo Lastra, and Dinesh Manocha, for their patience and understanding, especially since this dissertation took a bit longer than I had originally predicted.

I would also like to thank my parents and brother for their constant support throughout my entire graduate career. Maybe this year, for the first time in five years, I won't spend Thanksgiving and Christmas cloistered away, working on a paper.

Without my friends in Chapel Hill, Karl Gyllström, Andrew Leaver-Fay, and Younoki Lee, I am sure that burnout would have brutally truncated my graduate career long ago. A special thanks to Younoki for her endless supply of delicious imitation crab salad. I also want to thank my undergraduate roommate, Jeremy Kubica. Perhaps this memory is apocryphal, but first semester freshman year, you said you wanted to work in robotics, and I said I wanted to do graphics. If you're reading this, it means we now have PhDs in these fields.

My summer internships at Rhythm and Hues Studios in Los Angeles taught me what industrial-strength code and movie production pipelines looks like, for which I have to thank Jubin Dave and zuzu Spadaccini. You gave me an invaluable professional experience, and more importantly, your friendship.

Last but not least, I thank my fiancée Ivy Bigelow for her endless support, enthusiasm, and encouragement. You give this work meaning.

TABLE OF CONTENTS

LIST OF FIGURES	xv
------------------------	-----------

LIST OF TABLES	xix
-----------------------	------------

1 Introduction	1
1.1 Visual Characteristics	2
1.2 The Stefan Problem	7
1.2.1 One and Two Sided Stefan Problems	8
1.2.2 The Quasi-Steady State Approximation	9
1.2.3 Surface Tension	10
1.2.4 Thin Film Boundary Conditions	10
1.3 Thesis Statement	11
1.4 Main Results	12
1.5 Organization	13
2 Related Work	14
2.1 Early Work	15

2.2	Related Work In Physics	17
2.2.1	Phase Field Methods	17
2.2.2	Level Set Methods	20
2.2.3	Thin Film Growth	22
2.2.4	Laplacian Growth	24
2.3	Analytical Solutions to the Stefan Problem	25
2.3.1	Planar Case	25
2.3.2	Spherical Case	27
2.3.3	Parabolic Case	28
2.3.4	Cylindrical Case	30
2.4	Related Work In Graphics	32
2.4.1	Phase Transition	32
2.4.2	Modeling Winter Scenes	33
2.4.3	Pattern Formation	33
3	The Phase Field Method	36
3.1	Overview	38
3.2	The Phase Field Method	39
3.2.1	Undercooled Solidification	40
3.2.2	The Phase Field	40
3.2.3	The Kobayashi Formulation	42

3.2.4	Relation to the Stefan Problem	44
3.2.5	Improved Anisotropy	47
3.2.6	Possible Ice Crystal Shapes	48
3.2.7	Banded Optimization	48
3.2.8	Hardware Implementation	50
3.3	User Control	52
3.3.1	Seed Crystal Mapping	54
3.3.2	Freezing Temperature Mapping	54
3.4	Introducing Internal Structure	55
3.4.1	Naïve bump mapping	55
3.4.2	Adding Subdivision Creases	56
3.4.3	Morphological Operators	56
3.4.4	Control Mesh Segment Generation	59
3.4.5	Triangulation Generation	61
3.4.6	Height Field Generation	62
3.4.7	Crease Generation	62
3.4.8	Rendering	63
3.5	Implementation and Results	63
3.5.1	Implementation	63
3.5.2	Simulation Parameters	64

3.5.3	Results	64
3.5.4	Discussions and Limitations	66
3.6	Summary	67
4	A Hybrid Algorithm	74
4.1	The Process of Solidification	76
4.1.1	Three Stages of Freezing	77
4.1.2	Diffusion Limited Growth	78
4.1.3	Kinetics Limited Growth	79
4.1.4	Heat Limited Growth	81
4.2	Relation to the Stefan Problem	81
4.2.1	The Dielectric Breakdown Model	81
4.2.2	DBM as a Stefan Problem	84
4.3	A Hybrid Algorithm for Ice Growth	86
4.3.1	Phase Fields and DLA	86
4.3.2	Phase Fields and Fluid Flow	89
4.3.3	DLA and Fluid Flow	90
4.3.4	User Control	91
4.4	Faster Phase Field Methods	92
4.4.1	Second Order Accuracy In Time	94
4.4.2	Performance Analysis	95

4.5	Implementation and Results	96
4.6	Discussions and Limitations	98
4.7	Summary	100
5	Icicle Growth	107
5.1	The Stefan Problem	109
5.1.1	Background	109
5.1.2	The Classic Stefan Problem	110
5.1.3	The Thin Film Stefan Problem	111
5.1.4	The Thin Film Ivantsov Parabola	113
5.2	A Ripple Formation Model	117
5.3	A Level Set Solver	120
5.3.1	Background	120
5.3.2	The Velocity Field	121
5.3.3	Inserting the Icicle Tips	123
5.3.4	Tracking the Ripples	125
5.4	Rendering	125
5.5	Results and Validation	128
5.6	Summary	130
6	Conclusion	136

6.1	Summary of Results	137
6.2	Limitations	138
6.2.1	Phase Fields and DLA	139
6.2.2	Icicle Simulation	140
6.2.3	Rendering Issues	141
6.3	Future Work	142
A	Cg Implementation of Phase Fields	145
	Bibliography	151

LIST OF FIGURES

1.1	Taxonomy of Snowflakes	3
1.2	Snowflake Photographs	4
1.3	Combination of plate and dendritic growth	4
1.4	Photograph of frost	5
1.5	Icicles On a Fountain	6
1.6	One-sided Stefan problem	9
2.1	von Koch Snowflake	16
3.1	Closeup of ice on a stained glass window	38
3.2	Phase field system pipeline	39
3.3	Cross-section of phase fields	41
3.4	Comparison of phase field snowflakes to real snowflakes	45
3.5	Phase field controls	53
3.6	Border extraction operation	57
3.7	Structuring Elements	58
3.8	Results of modified erosion operator	58
3.9	Skeletonization structuring elements	59
3.10	Results of skeleton and border operations	60
3.11	Crease pixel types	60

3.12 Sharpening Results	61
3.13 Lilypad ice growth	65
3.14 Ice ring growth	69
3.15 Ice growth on a window panel	70
3.16 Ice growing on a red stained glass window	71
3.17 Ice growing on a stained glass window	72
3.18 Light refracting through a stained glass window	73
4.1 A microscopic view of the three stages of freezing	76
4.2 Grid anisotropy in diffusion limited aggregation.	79
4.3 Stencils and initial conditions for DBM	82
4.4 Comparison of DBM and DLA	84
4.5 Finite difference stencils for a hexagonal grid	88
4.6 A 4-armed dendrite growing in a flow	91
4.7 Phase fields with and without diagonal terms	93
4.8 Frosty ice forming on a chilled glass	102
4.9 Ice Accumulated on a car	103
4.10 Frost forming on a window	104
4.11 Comparison to hybrid algorithm to DLA and phase fields	105
4.12 Validation of hybrid algorithm against a photograph	106
4.13 Snowflake growths	106

5.1	2D slice of parabolic coordinate system	115
5.2	Ray traced icicle star	126
5.3	BSSRDF icicle star	127
5.4	Experimental validation of thin-film Ivantsov parabola	130
5.5	Icicle star	132
5.6	Icicle star forming	133
5.7	A freezing fountain	134
5.8	Ice forming on a roof	135

LIST OF TABLES

2.1	Symbols for the Makkonen model	23
3.1	Phase field constants	43
3.2	Banded vs. Unbanded Performance	50
3.3	CPU vs. GPU performance	52
4.1	Phase field performance over different resolutions	96
4.2	Timing results for simulation	97
5.1	Table of icicle symbols.	117
5.2	Icicle Growth Data	131

Chapter 1

Introduction

Many years later, as he faced the firing squad, Colonel Aureliano Buendía was to remember that distant afternoon when his father took him to discover ice.

– Gabriel Garcia Marquez, *One Hundred Years of Solitude*

Ice formations are one of the most memorable and visually arresting phenomena in nature. On cold mornings, branching frost patterns can be found on sidewalks, window panes, and car windshields. No winter scene would be complete without icicles dangling from tree branches and rooftops. These formations are interesting because they exhibit a high degree of geometric and optical complexity. As the old adage says: “No two snowflakes are alike.” The same could pedantically be said about any collection of objects, but the saying rings true for snowflakes because they span such a wide variety of geometric forms. Because ice is translucent, this geometric complexity also translates to optical complexity. Ice stands out in marked contrast to the smooth, diffuse reflections of snow because it produces glittering, highly specular light interactions.

Scientific fascination with ice formation dates back to at least the birth of modern science. Johannes Kepler first wrote of the six-fold symmetry of the snowflake almost 400 years ago (Kepler, 1611). René Descartes, a contemporary of Kepler, later wrote about the wide variety of snowflakes he observed with the naked eye and pondered their formation mechanism (Frank, 1974). Robert Hooke examined snowflakes using a

compound microscope and included sketches of what he saw in his book *Micrographia* (Hooke, 1665). At the time, a more extensive quantitative analysis of ice formation was not possible because thermodynamics was still poorly understood.

Like wind and fire, ice is viewed as elemental, so it has found considerable use as a dramatic tool in visual effects. Its use predates the adoption of digital effects in the film industry, and plays a pivotal role in such scenes as the formation of the Fortress of Solitude in the 1978 film *Superman*, and the freezing death of Jack Torrance in the 1980 film *The Shining*. More recently, digital freezing effects were used to great dramatic effect in the 2004 film *Harry Potter and the Prisoner of Azkaban*. The ominous appearance of frost was used to signify the arrival of the movie’s villains, the Dementors. A film from the same year, *The Day After Tomorrow*, follows the flight of its characters from a rapidly advancing ice age, and made extensive use of freezing effects. In this case, ice *was* the villain. Numerous other recent movies have made prominent use of digital freezing effects, such as *Die Another Day*, *The Hulk*, *The Incredibles*, *The Lion the Witch and the Wardrobe*, *Van Helsing*, and *X-Men 2*.

1.1 Visual Characteristics

The goal of this dissertation is to faithfully simulate the interesting visual features of ice, so the first step is to define which visual features give ice formations their enduring appeal. Any list of such features is at best a set of conjectures, so the remainder of the dissertation will be devoted to demonstrating that the features I have chosen do in fact reproduce much of ice’s appeal. Once this feature list has been defined, I will devise methods of efficiently simulating the mechanisms that give rise to these features.

In the case of snowflakes, a precise characterization of geometric structure can be difficult, because part of their appeal is that they often take on novel and surprising structures. Crystal growth is an active area of research, and extensive empirical observation of snowflakes has yielded the taxonomy in Figure 1.1. However, Figure 1.1 provides a larger taxonomy than necessary for visual simulation. The hollow prism

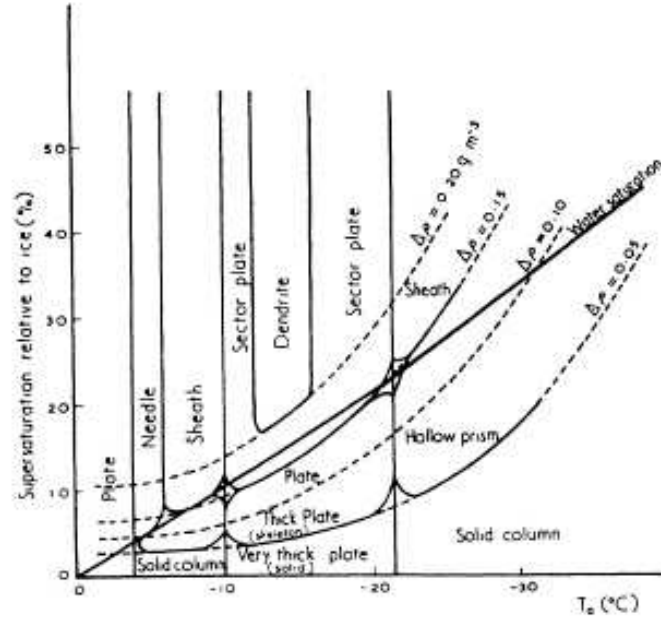


Figure 1.1: **Taxonomy of Snowflakes:** Extensive empirical observation of snowflakes have yielded a taxonomy of shapes. The widely varying geometry of snowflakes can be attributed to changing environmental conditions during formation. (From (Yokoyama and Kuroda, 1990))

and solid column types, for example, refer to three dimensional snowflakes that can be produced in laboratory settings, but are usually not observed in a typical winter scene. Instead, most snowflakes can be viewed as existing on the continuum between ‘dendritic’ and ‘sectored plate’ growth. ‘Dendritic’ literally derives from ‘tree-like’ or ‘bush-like’, and refers to thin, spindly features, such as the snowflake on the far right of Figure 1.2. ‘Sectored plate’ refers to the hexagonal growth pattern on the far left of Figure 1.2. Several examples of intermediate growth conditions in between can be seen in the center two images of Figure 1.2. Other patterns can form when the snowflake drifts between different atmospheric conditions during the growth process. An example of this can be seen Figure 1.3. The snowflake initially started in the sectored plate regime but then transitioned to the dendritic regime. Therefore, a visual simulation method should be able to accurately model the continuum of growth processes between sectored plate and dendritic growth, because this continuum encapsulates a large variety

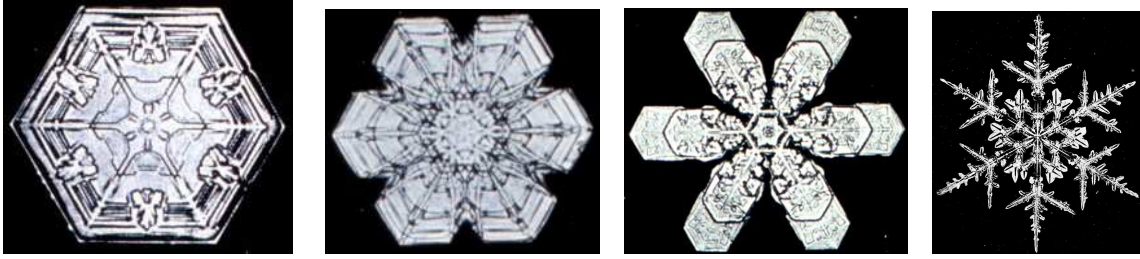


Figure 1.2: **Snowflake Photographs:** From left to right, the snowflake shapes transition from sectored plate growth to dendritic growth. Photographs are from the Wilson “Snowflake” Bentley collection. (Bentley, 1902)



Figure 1.3: **Combination of Plate and Dendritic Growth:** This snowflake began growing in conditions that favored sectored plate growth, but at some point drifted into atmospheric conditions amenable to dendritic growth. This photograph is from the Wilson “Snowflake” Bentley collection. (Bentley, 1902)

of crystal structures.

In the case of frost, the defining geometric feature is dendritic growth around the boundaries, as can be seen in Figure 1.4. Far from the boundary, the ice forms a continuous plate, so visually speaking, frost can be thought of as many snowflakes that have grown together. The actual physical processes differ significantly, but a more thorough description of these differences will be left to Chapter 4. Optically, both snowflakes and frost are characteristically translucent, and in the neighborhood of sharp features, sparkling specularities tend to appear.

To summarize, I hypothesize that the dominant visual characteristics of frost and snowflakes are:



Figure 1.4: **Photograph of frost:** The main visual geometric feature is the dendritic growth along the boundary, while the main optical feature is the translucency and the sparkling specularities. The photo is from iStockPhoto.com.

- Growth that can vary continuously between the dendritic and sectorial plate regimes,
- Automatic merging of nearby features that grow together,
- Optical translucency, with specularities in sharp regions.

Icicle growth poses challenges distinct from those in frost and snowflake growth. While similar physical processes are involved, this does not necessarily translate to similar computational methods. An icicle can be viewed as one large dendrite, and the rippling on the sides of an icicle can be viewed as dendrites that failed to grow due to a lack of water supply. A striking example of icicle growth can be seen in Figure 1.5.

To my knowledge, a taxonomy of icicle shapes equivalent Figure 1.1 has not been constructed. There is some recent work on the formation of ripples along a crystal sur-



Figure 1.5: **Icicles On a Fountain:** Photo is from BigFoto.com.

face (Ueno, 2003; Ueno, 2004), the author of these articles admits that the thermodynamics of thin film flows still has many open questions, making analysis and taxonomy construction difficult. However, the major visual features of icicles can be conjectured from photos such as Figure 1.5. The first, most high-level observation is that icicles are conical structures that are much longer than they are thick. Second, when two icicles grow near to each other, their roots merge. Lastly, the small scale rippling on the surface of icicles cause large scale optical effects, such as rippled specularities and distorted refractions.

Explicitly, the dominant visual features of icicles are:

- Conical geometry that is much longer than it is wide,
- Automatic merging of nearby icicle roots,
- Optical effects caused by surface rippling.

1.2 The Stefan Problem

All of the previously listed visual characteristics can be understood in terms of the Stefan problem. The Stefan problem was formulated in 1889 by Josef Stefan (Stefan, 1889), who is perhaps best known for the Stefan-Boltzmann law, which relates the energy radiated by a blackbody emitter to its temperature. As a prominent scientific mind at the time when the laws of thermodynamics were first becoming well understood, Stefan was in a prime position to start addressing solidification problems.

Stefan posed his problem in the context of ocean ice forming in arctic regions, but the problem has come to represent phase transition problems in general, and has found applications in fields ranging from geology to metallurgy. The richly non-linear behavior of the problem has also attracted considerable interest in mathematics (Hill, 1987; Meirmanov, 1992). An excellent historical overview of the problem is available in (Wettlaufer, 2001). While the visual characteristics just listed can be captured in the context of Stefan problems, they each require a different version of the problem, which in turn requires different computational approaches. As the Stefan problem is the theoretical thread that unifies all of these approaches, I will now provide a high level description of the problem and describe the various versions and approximations that will later be employed.

The Stefan problem is composed of two simple equations. Assume we have a heat field T defined continuously over some computational domain, and an initial ice/water interface Γ . The heat field evolves according to the heat equation

$$\frac{\partial T}{\partial t} = D \nabla^2 T, \quad (1.1)$$

where t denotes time and D denotes a diffusion constant. The symbol ∇^2 is the Laplacian operator, which expands to $\frac{\partial^2}{\partial x^2} + \frac{\partial^2}{\partial y^2}$ in 2D and $\frac{\partial^2}{\partial x^2} + \frac{\partial^2}{\partial y^2} + \frac{\partial^2}{\partial z^2}$ in 3D. The ice/water interface then evolves in the normal direction according to

$$\frac{\partial \Gamma}{\partial t} \cdot \mathbf{n} = D \frac{\partial T}{\partial \mathbf{n}}, \quad (1.2)$$

where \mathbf{n} denotes the normal direction. Fluid velocity and the coefficient of expansion of ice are assumed to be negligible. Stefan stated the 1D version of this problem, essentially approximating the ocean as a column of water. In 1D, the equations reduce to:

$$\frac{dT}{dt} = D \frac{d^2T}{dx^2} \quad (1.3)$$

$$\frac{d\Gamma}{dt} = D \frac{dT}{dx}, \quad (1.4)$$

where x is the spatial coordinate. The location of the ice front Γ is then obtained by integrating Eqns. 5.1 and 1.2. There are only a handful of known closed form solutions, and these only apply to simple geometries. Stefan originally solved the planar case, and subsequently the case of a sphere (Frank, 1949) and a parabola (Ivantsov, 1947) were derived. These cases are often referred to eponymously as the “Frank sphere” and “Ivantsov parabola” solutions. In the absence of a general analytical solution, solutions are usually obtained numerically. Depending on the approximations used and the boundary conditions assigned, various flavors of the Stefan problem can be obtained. In this dissertation, I will deal with the following variants: one and two sided, quasi-steady state, zero surface tension, and surface tension anisotropy.

1.2.1 One and Two Sided Stefan Problems

Stefan originally described the boundary conditions shown in the left half of Figure 1.6. In this case, heat diffusion only occurs in the ice, and the air and water are assumed to be at a constant temperature. Since the thermal conductivity of air and water is smaller than that of ice, the heat loss to these media is assumed to be negligible. This is known as a *one sided* Stefan problem, since it only takes into account heat diffusion on one side of the ice/water interface. The complementary case is shown on the right side of Figure 1.6, where heat diffusion is instead tracked in the water layer. In this case, we assume that solidification is taking place, which means that the interface $x = \Gamma$ must

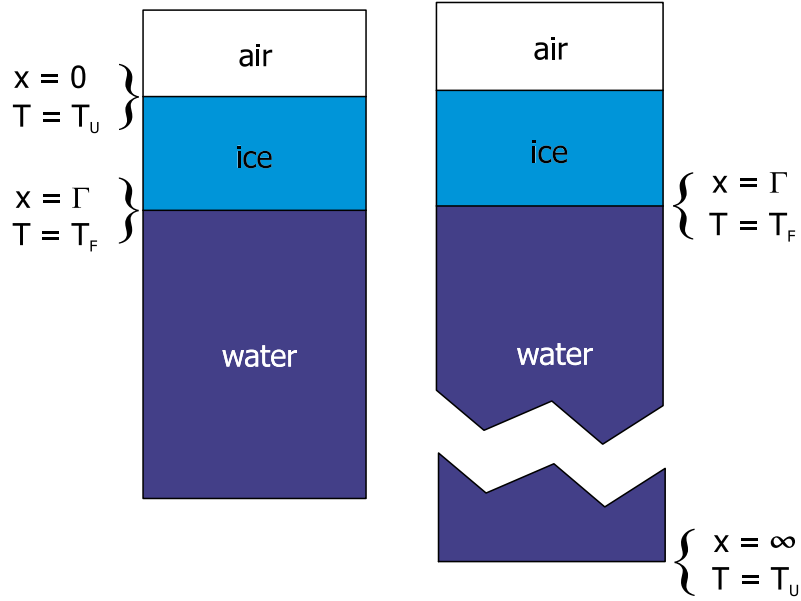


Figure 1.6: **Boundary conditions of one-sided Stefan problem:** x denotes the spatial coordinate, T is the temperature, Γ is the current position of the advancing ice front, T_f is the freezing temperature of water, and T_u is some temperature less than T_f . In the left figure, the interface evolves according to the temperature gradient in the ice; on the right, it evolves according to the gradient in the water.

be at freezing temperature. But, unlike the case in Figure 1.6, the interface evolves according to the temperature gradient in the water, not the ice. This version allows us to define the water temperature at some far away location, usually infinity.

A *two sided* Stefan problem tracks heat diffusion in both the ice and the water. This case can be more difficult to simulate because the diffusion constants of water and ice differ, and handling this discontinuity at the interface can require additional considerations. I will describe methods of simulating the two-sided Stefan problem in Chapter 3 and the one-sided problem in Chapters 4 and 5.

1.2.2 The Quasi-Steady State Approximation

Stefan observed that if the diffusion constant D is very large relative to the interface velocity $\frac{\partial \Gamma}{\partial t}$, then the heat field T can be treated as if it is essentially in equilibrium. This

is known as the *quasi-steady state* approximation, an approximation commonly used in thermodynamics to distinguish between a reversible and irreversible transformation. Eqn. 5.1 then reduces to the Laplace equation:

$$\nabla^2 T = 0. \quad (1.5)$$

This greatly simplifies integration of the Stefan problem, since the entire subfield of harmonic analysis is devoted to examining the Laplace equation, and we can now draw upon this knowledge. The quasi-steady state approximation will be employed in Chapters 4 and 5.

1.2.3 Surface Tension

Surface tension is perhaps most familiar as the force that causes bubbles to form, and allows insects to walk across water surfaces. Both of these cases are examples of surface tension at a liquid/gas interface. In a more general sense, surface tension is a force that exists along any interface, including the solid/liquid interface of ice and water. Surface tension can be incorporated into the Stefan problem by adding an additional function $s(\theta)$ to Eqn. 1.2:

$$\frac{\partial \Gamma}{\partial t} \cdot \mathbf{n} = D \frac{\partial T}{\partial \mathbf{n}} s(\theta). \quad (1.6)$$

The details of this function $s(\theta)$ and its role in ice pattern formation will be discussed in Chapter 3.

1.2.4 Thin Film Boundary Conditions

In the classic Stefan problem, the water supply is assumed to be infinite. This is because Stefan originally formulated the problem in the context of oceans freezing, where the ice freezes downwards into deep, essentially infinite regions of water. Icicle formation represents a different physical case, where a thin film of water continuously

coats the outside of the ice. This ‘thin-film’ variant of the Stefan presents a different set of challenges, and I will describe them in detail in Chapter 5.

1.3 Thesis Statement

My thesis statement is as follows:

The visual features of ice formations such as frost, snowflakes, and icicles can be simulated efficiently by solving appropriate versions of the Stefan Problem.

In support of this thesis, I have constructed three different prototype systems. In the first, I use *phase fields*, a numerical technique from computational physics. Phase field methods correspond to the *two-sided* Stefan problem with *surface tension anisotropy*. This technique captures the first two visual characteristics of frost and snowflakes: the continuum of growth regimes between dendritic and sectorial plate, and automatic merging of intersecting features. In order to address the third characteristics, the optical features of ice, I employ the photon mapping global illumination algorithm (Jensen, 2001).

Phase fields are an Eulerian simulation technique that represents the ice/water interface as an implicit surface, so the results can suffer from smoothing artifacts. In order to address this limitation, I have constructed a second system that combines phase fields with a fractal growth technique known as *diffusion limited aggregation* (DLA). DLA corresponds to the *zero-surface tension, quasi-steady state* Stefan problem. DLA is a discrete, Lagrangian simulation technique that does not suffer from smoothing artifacts. On the contrary, it can often produce features that are unnaturally sharp. By combining DLA and phase fields, I strike a middle ground between the advantages and limitations of both techniques.

The third and last system uses level set methods, an alternate implicit surface tracking scheme, to simulate icicle formation. Icicle growth corresponds to the *thin-film*,

quasi-steady state Stefan problem, and the literature on this particular type of Stefan problem is relatively sparse. There is no established technique akin to phase fields in the crystal growth literature, so I instead derive the necessary velocity equations for a level set simulation. The level set solver addresses the first two visual characteristics of icicles: structures that are longer than they are thick, and merging features. The last feature, optical effects due to rippling, are addressed by tracking arrival times along the surface of the icicle. A displacement shader uses these arrival times at render time to generate ripples using an analytical model from physics.

1.4 Main Results

Beyond capturing the major visual characteristics of a phenomena, there are other considerations that should be taken into account when constructing a visual simulation method. For example, it should include intuitive user parameters that can be used to drive the simulation towards a desired effect, it should be computationally efficient, and, if possible, it should be easy to implement. With this in mind, the following are the main results of this dissertation.

Chapters 3 and 4 present a method of simulating frost and snowflake formation. The main results of these two chapters are:

- A fast, simplified formulation of the phase field method for two-sided Stefan problems with surface tension anisotropy,
- Hybridization of phase fields with diffusion limited aggregation for improve capturing of small scale detail,
- Simple and natural aesthetic control parameters for generating desired visual effects,
- A physically-inspired, novel geometric processing step that introduces internal structure to the ice and enhances the visual realism of the final rendered image,

- A novel discrete-continuous method that combines diffusion limited aggregation and phase field methods with a stable fluid solver,
- Accelerated and simplified computations for interactive simulation of modest-scale ice crystal growth, including a mapping to GPUs.

Chapter 5 presents a method of simulating icicle growth. The main results of this chapter are:

- A level set approach to the thin-film Stefan problem,
- An analytical solution for the tip of an icicle that appears to be in agreement with experimental data,
- A non-linear, curvature-driven evolution equation for the ice front far from the icicle tip,
- A method for simulating surface ripples that avoids the need to track small scale geometry in the simulation,
- A unified simulation framework for modeling complex ice dynamics.

1.5 Organization

The organization of this dissertation will be as follows. Chapter 2 will present an overview of past and related work. Chapters 3 - 5 each deal with one of the prototype systems described in the previous section. Each of these chapters will describe the version of the Stefan problem that will be employed, and the computational methods used to solve that version. Chapter 6 will summarize the main contributions of this work and suggest future directions for research.

Chapter 2

Related Work

The study of pattern formation in solidification spans many different fields, including math, physics, material science, geology, and computer science. The body of literature is considerable, with entire journals (e.g. *The Journal of Crystal Growth*) devoted to the topic. In this section, I will give a brief a historical perspective, and then survey the works that are relevant to this dissertation.

2.1 Early Work

As mentioned in the introduction, the study of patterns in ice can be traced back to at least the 17th century with Kepler and Descartes. However, it was not until the end of the 19th century, when thermodynamics were better understood, that Stefan formulated a more quantitative model.

In 1904, Helge von Koch famously described a visual algorithm that captures the general structure of dendritic ice (von Koch, 1906). It defines simple production rules that, when applied recursively, produces a structure that is in close visual agreement with that of a snowflake (Figure 2.1). In contrast to the Stefan problem, the “von Koch snowflake”, as it is now known, is a discrete model with somewhat tenuous connections to physical mechanisms. However, due to the simplicity of the algorithm, it is easy to both understand and analyze, and is often used as the introductory example to fractal geometry.

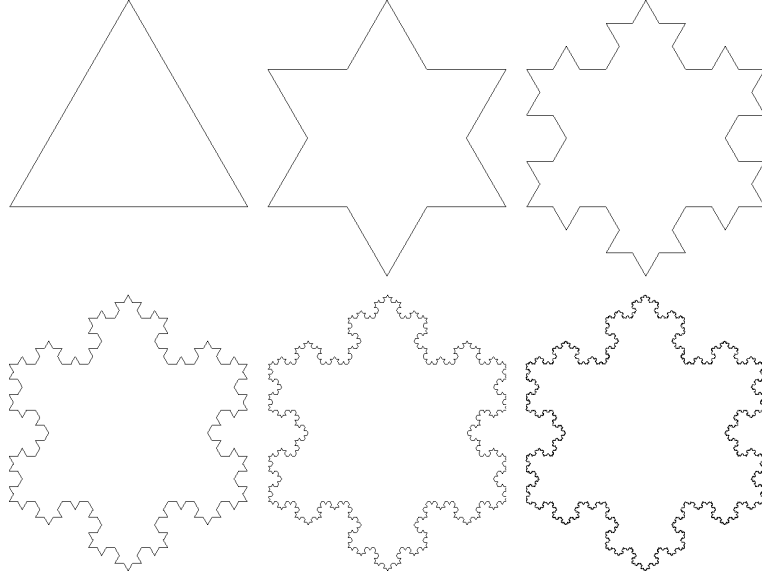


Figure 2.1: **von Koch Snowflake:** Helge von Koch defined production rules that generate structures that are qualitatively similar to those of a snowflake. While von Koch’s model is fairly simple, its easily calculated fractal dimension provides an avenue for analyzing more complex models.

Fractal geometry refers to structures that have *fractional* dimension. The canonical work on the subject is *The Fractal Geometry of Nature* (Mandelbrot, 1982). While we are accustomed to objects that have integral dimension such as 1D, 2D, and 3D, Benoit Mandelbrot famously described methods of defining in between dimensions such as 1.71D and 2.55D. The von Koch snowflake, for example, has a fractal dimension of $\frac{\log 4}{\log 3} \approx 1.26$.

The von Koch snowflake is too simple a model to constitute a complete simulation method within itself, but applying similar fractal analysis to more complex models has proved fruitful. Particularly, one of the main algorithms used in this dissertation, diffusion limited aggregation, is characterized primarily by its fractal dimension.

2.2 Related Work In Physics

Wilson “Snowflake” Bentley, a Vermont farmer with no formal scientific training, developed a technique in 1885 for photographing snowflakes and constructed an extensive catalog of over 5000 snowflake images. Some of these photographs were later compiled and published as a book (Bentley and Humphreys, 1962). Purportedly inspired by Bentley’s photographs, Japanese physicist Ukichiro Nakaya developed a method of growing snowflakes in a laboratory, and published an extensive study of crystal shapes entitled *Snow Crystals, Natural and Artificial* (Nakaya, 1954). In his book, Nakaya described a crystal taxonomy and the relationship between crystal shape and atmospheric conditions. Nakaya’s work also gave rise to additional questions, such as why the transition between different growth regimes was so abrupt.

2.2.1 Phase Field Methods

Addressing solidification problems is difficult for several reasons. The complexity of crystal structures make them resistant to analytical methods because even the selection of an appropriate coordinate system becomes difficult. The Stefan problem involves a free boundary, which means that the equations must be integrated in terms of a boundary condition that is also one of the unknowns. Finally, there is a jump in physical values at the ice/water interface, and representing this discontinuity is challenging.

Early methods attempted to simulate solidification using a boundary layer model (Ben-Jacob et al., 1983; Ben-Jacob et al., 1984), which explicitly tracked the location of the ice/water interface. While this solves the problem of resolving the ice/water discontinuity, it can only be used to model very simple crystals, because problems occur if the interface folds over onto itself. Sethian (Sethian, 1999) describes this problem and those like it by describing explicit tracking methods as ‘marker and string’ methods. We can imagine the boundary as represented by a discrete set of marker points, with string run between adjacent points. During simulation, the markers are moved, and the string continues to stretch between them. The problem occurs if two of the markers cross over

each other, and the string literally becomes tangled. There are various mathematical methods for untangling or ‘de-looping’ of the results, but they are both inelegant and extremely difficult to implement.

The *phase field* method was first suggested by Langer (Langer, 1986) as a model of solidification. It is an implicit simulation method that does not explicitly track the location of the ice/water interface. Instead, it addressed the issue of the infinitely sharp ice/water discontinuity by smearing the interface out into a region of fast but finite transition that is resolvable on a regular grid. Langer based his work on earlier work by Halperin et al. (Halperin et al., 1974) and used the term ‘phase field’ that was coined by Fix (Fix, 1983).

Phase fields were first used to successfully simulate crystal growth of varying morphology by Kobayashi (Kobayashi, 1993), and since then have become the preferred simulation method in crystal growth. The simulations can be very computationally expensive however, so various techniques have been applied to the problem. Adaptive mesh refinement techniques (Provatas et al., 1999) have been used to increase the resolution of the solution around regions of interest. Additionally diffusion Monte Carlo techniques (Plapp and Karma, 2000) have been used to track the heat field far from the interface, resulting in significant computational savings. Far from the interface, heat is tracked as a set of particles whose dynamics are much cheaper to compute than flow over a mesh.

The phase field method is not directly derived from the Stefan problem, but instead follows from a free energy derivation that appeals more directly to thermodynamics. As the phase field method composes a significant portion of this dissertation, I will provide an overview of the derivation here.

While there is more than one method of deriving the phase fields equations, the most commonly cited one remains the energy derivation from the original paper on the topic (Langer, 1986). A geometric derivation has also been suggested (Beckermann et al., 1999), but I will adhere to the energy derivation here. There are several places in the derivation where different functions can be chosen. In these cases, I will use the

choices made by Kobayashi (Kobayashi, 1993), since it is his formulation that is used in this dissertation.

The free energy F over some volume V of ice and water can be written as:

$$F = \int_V \left(f(T, p) + \frac{\varepsilon^2}{2} |\nabla p|^2 \right) dV. \quad (2.1)$$

The variable p is the phase variable, where $p = 0$ denotes water and $p = 1$ denotes ice, f is the energy density, and ε is a gradient entropy coefficient. Intuitively, the integral sums the energy density f over the entire volume, but gives special treatment to regions that contain non-zero phase gradients. By definition, these regions correspond to the ice/water interface. An equation for the evolution of the phase variable p can then be obtained by taking the variational derivative of F and applying the relation:

$$\tau \frac{\partial p}{\partial t} = - \frac{\delta F}{\delta p}. \quad (2.2)$$

This relation yields:

$$\tau \frac{\partial p}{\partial t} = \nabla \cdot (\Phi \nabla p) + \frac{\partial f}{\partial p}. \quad (2.3)$$

In 1D, $\Phi = \varepsilon^2$, and in 2D the symbol expands to the diffusion tensor:

$$\Phi = \begin{bmatrix} \varepsilon^2 & -\varepsilon \frac{\partial \varepsilon}{\partial \theta} \\ \varepsilon \frac{\partial \varepsilon}{\partial \theta} & \varepsilon^2 \end{bmatrix}. \quad (2.4)$$

There are several possibilities for the function f , but Kobayashi uses the function

$$f(T, p) = \frac{p^4}{4} - \left(\frac{1}{2} - \frac{m}{3} \right) p^3 + \left(\frac{1}{4} - \frac{m}{2} \right) p^2. \quad (2.5)$$

Inserting this function into Eqn. 2.6, we obtain the final evolution equation for p :

$$\tau \frac{\partial p}{\partial t} = \nabla \cdot (\Phi \nabla p) + p(1 - p) \left(p - \frac{1}{2} + m \right). \quad (2.6)$$

For the symbol m , Kobayashi selects the function $m(T) = \frac{\alpha}{\pi} \tan^{-1}(\gamma(T_e - T))$,

where α , π , and γ are constants, and T_e is the freezing temperature of water. Explicitly multiplying through the diffusion tensor gives the 2D evolution equation:

$$\tau \frac{\partial p}{\partial t} = \nabla \cdot (\varepsilon^2 \nabla p) - \frac{\partial}{\partial x} \left(\varepsilon \varepsilon' \frac{\partial p}{\partial y} \right) + \frac{\partial}{\partial y} \left(\varepsilon \varepsilon' \frac{\partial p}{\partial x} \right) + p(1-p) \left(p - \frac{1}{2} + m \right). \quad (2.7)$$

Subsequent work has rigorously proved that in the limit, $\lim_{\varepsilon \rightarrow 0} \tau \frac{\partial p}{\partial t}$, the phase field equations do indeed converge to the Stefan problem with surface tension (Caginalp and Chen, 1992).

2.2.2 Level Set Methods

Level set methods, an alternate implicit front tracking strategy, has also been successful in simulating crystal formation. Level set methods were first developed by Osher and Sethian (Osher and Sethian, 1988) as a general front tracking strategy, and have since found numerous applications including computational fluid dynamics (Foster and Metaxas, 1996), lithography (Adalsteinsson and Sethian, 1995b; Adalsteinsson and Sethian, 1995c; Adalsteinsson and Sethian, 1997), and computer vision (Malladi et al., 1995). Both Osher (Osher and Fedkiw, 2003) and Sethian (Sethian, 1999) have written books that exhaustively describe level set methods, the wide variety of techniques that have been developed surrounding them, and their numerous applications.

Whereas phase fields smear out the location of the ice/water interface, level set methods track the precise position of this interface. Instead of tracking a phase order parameter p , the level set method tracks the evolution of some implicit function ϕ , usually a signed distance function. Whereas the phase field method essentially relies on a reaction equation to correctly evolve the interface, level set methods construct a velocity field \mathbf{v} over the entire computational domain and then evolve ϕ according to

$$\frac{\partial \phi}{\partial t} + \mathbf{v} \cdot \nabla \phi = 0.$$

The nomenclature of phase field and level set methods can unfortunately overlap, because in a general sense ‘level sets’ refer to the isosurface of an implicit function. Therefore the interface location in phase fields is sometimes referred to as the ‘0.5 level set’ or the ‘zero level set’, depending on if the p parameter is defined over $[0,1]$ or $[-1,1]$. To avoid confusion, I will only use the term ‘level set’ in this dissertation when referring to the level set method.

Since phase fields only converge to the Stefan problem in the limit, it has been argued that they are only a first order accurate tracking method (Gibou et al., 2003). Level set methods were first applied to the problem of solidification in by Sethian and Strain (Sethian and Strain, 1992) using a boundary integral approach. A simpler method was later suggested by Chen et. al. (Chen et al., 1997) and later extended in a pair of articles (Gibou et al., 2003; Gibou and Fedkiw, 2005) to second and fourth order accuracy.

The strategy followed level set simulation of the Stefan problem is slightly different from that of the phase field method. While both use an implicit function to track the interface, the level set approach essentially constructs a temporary explicit representation every timestep. Since the implicit function used is a signed distance function instead of a phase order parameter, it is possible to locate the explicit interface with much higher accuracy than in phase field methods. Once this is done, the boundary is set according to the the Gibbs-Thomson relation,

$$T_I = \varepsilon_c \kappa - \varepsilon_v V_n$$

where T_I is the temperature at the interface, ε_c is a surface tension coefficient, κ is the local curvature, ε_v is the molecular kinetic coefficient, and V_n is the normal velocity of the interface.

Once these quantities have been defined along the interface, they must be incorporated back into the implicit level set simulation. A problem arises here because the Gibbs-Thomson relation only defines velocities along the ice/water interface, while level

set simulator require a velocity to be defined over the entire computational domain. This problem is overcome by interpolating the computed interface velocities back into their corresponding grid cells, and then extending the values over the entire simulation domain using an extension velocities method (Adalsteinsson and Sethian, 1999).

While the level set approach does yield higher numerical accuracy, it utilizes a good deal more numerical machinery than the phase field method. For simplicity, I use the phase field method in chapters 3 and 4. However, for the case of icicle growth, some of the features of level set methods become necessary, so I use them in chapter 5.

2.2.3 Thin Film Growth

All of the above work deals with growth in the presence of a large water supply. The previous work in phase fields and level set methods assume that the crystal is growing in an infinite bath of supercooled water, and Nakaya's snowflake work assumes that a large supply of water vapor is present in the atmosphere. Icicle growth instead deals with the case where the water supply is severely limited.

In glaciology, there exists some work on the problem of thin-film ice growth. Several analytical models exist for icicle formation (Maeno et al., 1994; Makkonen, 1988; Szilder and Lozowski, 1994), but these models are concerned with accurately capturing the ratio of an icicle's length to its radius. These models are derived using an energy balance approach using a plethora of environmental variables that are of limited value to the simulations addressed in this dissertation. For example, the Makkonen model (Makkonen, 1988) is composed of the two equations

$$\begin{aligned}
& -ht_a + h \frac{0.622L_e}{c_p p_a} (e(0^\circ C) - Re(t_a)) - \sigma \times at_a = \\
& \frac{3.74c_w}{d^2} \left[W_0 - \pi LD \left[\rho_a \frac{1}{2} \frac{dD}{dt} + h \frac{0.622}{c_p p_a} (e(0^\circ C) - Re(t_a)) \right] \right] \times \\
& \left[\frac{dL}{dt} - \frac{1}{2} \frac{dD}{dt} \right]^{0.588} + \frac{2L_f \rho_i \delta (d - \delta)}{d^2} \frac{dL}{dt},
\end{aligned}$$

symbol	definition
h	convective heat-transfer coefficient
t_a	air temperature
L_e	latent heat of evaporation
c_p	specific heat of water
p_a	air pressure
$e(0^\circ C)$	saturation water-vapor pressure
R	Relative humidity
$e(t_a)$	saturation water-vapor pressure
σ	Stefan-Boltzmann constant
d	diameter of pendant drop
W_0	mass flux of water to tip
ρ_a	density of icicle walls
ρ_i	ice density
δ	wall thickness at tip

Table 2.1: Symbols for the Makkonen (Makkonen, 1988) model.

and

$$\frac{dD}{dt} = \frac{-h_w t_a + h_w \frac{0.622 L_e}{c_p p_a} [e(0^\circ)C - R e(t_a)] - \sigma a t_a}{\frac{1}{2} \rho_a L_f (1 - \lambda)}.$$

The symbols are summarized in Table 2.1. The model involves pressures and densities that ideally would be abstracted away in a visual simulation model. To this end, I will forgo the glaciology models and instead derive a novel equation for icicle tip dynamics in Chapter 5. The analytical models from glaciology are not directly applicable to visual simulation, as they would merely generate simple cones and cannot capture surface rippling effects. Thin film ice formation is also a topic of interest in mechanical engineering, as ice forming on the wing of an aircraft is a hazardous scenario. The Messinger model (Messinger, 1953) is the standard method of determining when ice will form, and is an energy balance model that is also not directly applicable to visual simulation. Myers and Hammond (Myers and Hammond, 1999) recast the problem as a thin film Stefan problem, but only solve the 1D case.

Until very recently, the physics of ripple formation on crystal surfaces was a poorly

understood phenomena. However, Ogawa and Furukawa (Ogawa and Furukawa, 2002) recently proposed a model of ripple formation which was subsequently refined by Ueno in a pair of articles (Ueno, 2003; Ueno, 2004). The former model only applies to a cylinder, and the latter model was derived for an inclined plane. Ueno’s model will later be used in Chapter 5 to simulate ripple formation along the surface of an icicle.

2.2.4 Laplacian Growth

Laplacian growth is a general class of physical phenomena that includes ice growth, lightning formation, liquid surface tension, quasi-steady state fracture, and river formation, among others. The unifying notion is that patterns form according to a field that satisfies the Laplace equation (Eqn. 1.5). In the case of ice formation, this field corresponds to a quasi-steady state heat field. In other phenomena, the correspondence differs. In lightning and surface tension for example, the field corresponds to electric potential and fluid pressure.

A Laplacian growth simulation technique that has received a good deal of attention in the physics literature is diffusion limited aggregation, usually abbreviated as DLA (Witten and Sander, 1981). Originally formulated as a model of aggregating metal particles, it has since found success in various other phenomena, including snowflake growth (Family et al., 1987; Nittmann and Stanley, 1987). One of the defining characteristics of DLA is that it produces fractal structures. In 2D, DLA produces structures of approximately $D \approx 1.71$, and in 3D, $D \approx 2.55$.

The DLA algorithm is simple enough that it can be described informally. Given a discrete 2D grid, a single particle representing the crystal (or ‘aggregate’) is placed in the center. A particle called the ‘walker’ is then placed at a random location along the grid perimeter. The particle walks randomly along adjacent grid cells until it either is adjacent to the crystal or falls off the grid. If it is adjacent to the crystal, it sticks and becomes part of the crystal. A new walker is then inserted at the perimeter and the random walk is repeated. The process repeats until the desired aggregate size is achieved.

At first glance, it is not obvious that DLA corresponds to a Stefan problem, as it does not involve any differential equations. However, there are several algorithms that generate results that are visually indistinguishable from the results of DLA. One of these algorithms, the *dielectric breakdown model* (DBM) (Niemeyer et al., 1984) utilizes the Laplace equation (Eqn. 1.5) where DLA uses a random walk. I will later use DBM in Chapter 4 to describe the relationship of DLA to a Stefan problem.

2.3 Analytical Solutions to the Stefan Problem

There are a handful of known analytical solutions to the Stefan problem, and they only apply over simple geometries. However, I will use these solutions and their derivations later in chapter 5 to derive thin-film equivalents, so I will describe the classical ‘infinite water’ derivations here.

2.3.1 Planar Case

The planar case of the Stefan problem involves one coordinate, usually denoted as the negative z direction. This is because Stefan originally formulated the problem in terms of ocean ice forming, and the ice forms first at the surface of the water and gradually thickens downwards into an infinitely deep ocean. There are several different approaches to solving the 1D equations, but I will use the ‘moving-frame’ approach described in Saito (Saito, 1996). In this case we assume that the global coordinate is z , but introduce a moving variable $z' = z - Vt$, where V is velocity and t is time. In this way, at any time t , $z' = 0$ denotes the current location of the interface. In terms of this moving frame, the diffusion equation becomes

$$\frac{1}{D} \frac{\partial T}{\partial t} = \nabla^2 T + \frac{2}{l_D} \frac{\partial T}{\partial z'}$$

where D is again the thermal diffusion constant and $l_D = \frac{2D}{V}$. Applying the quasi-steady state approximation, we obtain

$$\nabla^2 T + \frac{2}{l_D} \frac{\partial T}{\partial z'} = 0.$$

By specifying an infinitely far away boundary condition $T(z' = \infty) = 0$, this can be integrated to

$$T(z') = Ae^{-\frac{2z'}{l_D}},$$

where A is an as yet undetermined constant of integration. The second equation in the 1D Stefan problem can now be written as:

$$\frac{dz'}{dt} = -D \frac{dT}{dz}.$$

In this form, it can be solved by plugging in the $T(z')$ to obtain:

$$\frac{dz'}{dt} = -D \frac{2A}{l_D} = AV.$$

Since $V = \frac{dz'}{dt}$, this means that the constant A must be equal to 1. We then apply the Wilson-Frenkel law:

$$\frac{dz'}{dt} = K((T_u) - T_i - d\kappa),$$

where K is the kinetic coefficient, T_u is the undercooling of the water, T_i is the temperature at the interface, d is the capillary length, and κ is the curvature. Applying this to the velocity equation, we obtain the final velocity of the planar interface:

$$\frac{dz'}{dt} = K(T_u - 1).$$

The feature to note is that this value is a constant, so for the planar case, the ice/water interface advances at a uniform velocity.

2.3.2 Spherical Case

The case of a sphere was solved by Frank (Frank, 1949), and is thus sometimes referred to as the ‘Frank sphere’ case. Again, I follow the derivation given by Saito (Saito, 1996). The case is again 1D, but instead of the cartesian coordinate z , we have the radial coordinate r , and the moving frame is r' instead of z' . The diffusion equation in spherical coordinates is:

$$\frac{1}{D} \frac{\partial T}{\partial t} = \left(\frac{\partial^2}{\partial r^2} + \frac{2}{r} \frac{\partial}{\partial r} \right) T.$$

Again applying the quasi-steady state approximation, we obtain:

$$\left(\frac{\partial^2}{\partial r^2} + \frac{2}{r} \frac{\partial}{\partial r} \right) T = 0.$$

Similar to the planar case, we specify an infinitely far away boundary condition $T(r' = \infty) = 0$, and obtain the solution $T(r) = \frac{A}{r}$. A is again an undetermined constant of integration. Applying the second equation of the Stefan problem, we obtain:

$$\frac{dr'}{dt} = \frac{DA}{(r')^2}.$$

Again applying the Wilson-Frenkel law, we obtain:

$$\frac{dr'}{dt} = K \left(T_u - \frac{A}{r'} - \frac{2d}{r'} \right).$$

Using these two equations, the constant of integration A is uniquely determined as:

$$A = \frac{(r')^2 \left(T_u - \frac{2d}{r'} \right)}{r' + \frac{D}{K}}.$$

The final velocity equation is then:

$$\frac{dr'}{dt} = \frac{D \left(T_u - \frac{2d}{r'} \right)}{r' + \frac{D}{K}}.$$

The detail to note is that below a certain radius, $\frac{2d}{T_u}$, the sphere will not grow. Unlike

the planar case, when the sphere does grow, it does not have a constant velocity, and instead the velocity slows as the radius increases.

2.3.3 Parabolic Case

In the parabolic case, we assume that the growing crystal takes the form of a parabola, and obtain an expression for the velocity of the tip. The original solution was obtained by Ivantsov (Ivantsov, 1947), but again I follow the derivation in Saito (Saito, 1996). To characterize the position of the tip, we use the same z and z' coordinates from the planar case, but in this case z' denotes the location of a parabola tip, not a plane. We then define a parabolic coordinate system around the z axis:

$$\begin{aligned}\xi &= r - z' \\ \eta &= r + z' \\ \theta &= \arctan(x/y).\end{aligned}$$

In this case, r is defined as $r = \sqrt{x^2 + y^2 + (z')^2}$. The parabolic version of the quasi-steady state heat equation can be written as:

$$\frac{1}{\eta + \xi} \left(\frac{\partial}{\partial \eta} \eta \frac{\partial T}{\partial \eta} + \frac{\partial}{\partial \xi} \xi \frac{\partial T}{\partial \xi} \right) + \frac{1}{4\eta\xi} \frac{\partial^2 T}{\partial \theta^2} + \frac{1}{l_D} \frac{1}{\eta + \xi} \left(\eta \frac{\partial T}{\partial \eta} - \xi \frac{\partial T}{\partial \xi} \right) = 0.$$

If we assume circular symmetry, this reduces to:

$$\frac{\partial}{\partial \eta} \left(\eta \frac{\partial T}{\partial \eta} \right) + \frac{1}{l_D} \left(\eta \frac{\partial T}{\partial \eta} \right) = 0.$$

Denoting the current location of the interface as η_i , the second equation of the Stefan problem translates to:

$$\eta_i + \xi \frac{\partial \eta_i}{\partial \xi} + \frac{\eta_i + \xi}{2V} \frac{\partial \eta_i}{\partial t} = -l_D \left(\eta_i \frac{\partial u}{\partial \eta} - \xi \frac{\partial \eta_i}{\partial \xi} \frac{\partial T}{\partial \xi} - \frac{\eta_i + \xi}{4\eta_i \xi} \frac{\partial \eta_i}{\partial \theta} \frac{\partial T}{\partial \theta} \right).$$

Using the boundary condition $T(\eta_i) = T_u$, the temperature field integrates to:

$$T(\eta) = T_u + C \int_R^\eta \frac{e^{-\frac{x}{l_D}}}{x} dx.$$

The symbol R denotes the radius of curvature of the parabola tip and C is a constant of integration. Using the boundary condition $T(\eta = \infty) = 0$, we can solve for the value of C ,

$$C = -\frac{T_u}{\int_R^\infty \frac{e^{-\frac{x}{l_D}}}{x} dx},$$

and obtain the heat solution:

$$T(\eta) = T_u \left(1 - \frac{\int_R^\eta \frac{e^{-\frac{x}{l_D}}}{x} dx}{\int_R^\infty \frac{e^{-\frac{x}{l_D}}}{x} dx} \right).$$

Inserting this heat solution into the second equation of the Stefan problem, we obtain what is known as the ‘Ivantsov relation’:

$$T_u = \frac{R}{l_D} e^{\frac{R}{l_D}} \int_R^\infty \frac{e^{-\frac{x}{l_D}}}{x} dx.$$

The relation is usually simplified using the change of variables $P = \frac{R}{l_D}$ and exponential notation $E_1(P) = \int_P^\infty \frac{e^{-x}}{x} dx$ to obtain:

$$T_u = P e^P E_1(P). \quad (2.8)$$

For small undercoolings, this relation is sometimes approximated in 3D as $T_u \approx P(-\log P - \gamma)$, where γ is the Euler-Mascheroni constant, and in 2D as $T_u \approx \sqrt{\pi P}$.

The feature to note is that the Ivantsov relation is that given an undercooling T_u , it can only be solved for the product of the radius of curvature and the velocity, RV . The tip velocity, the quantity that we are looking for, cannot be solved for directly. Experimental data shows that tip velocities are uniquely determined by the undercooling however, suggesting that an additional constraint is missing.

A good deal of effort has been devoted to determining the nature of this additional constraint. ‘Microscopic solvability theory’ (see for example (Brener and Mel’nikov, 1991)) suggests that the missing constraint is surface tension. Fortunately, in the case of icicle growth, experimental measurements show that the radius of the icicle tip stays relatively stationary under a wide variety of undercoolings, so in the case of this dissertation, an appeal to microscopic solvability theory is unnecessary.

2.3.4 Cylindrical Case

The cylindrical case corresponds to the case where a small column of undercooled water is surrounded by ice. I will follow the derivation given by Hill (Hill, 1987) here. The heat equation in cylindrical coordinates is:

$$\frac{\partial T}{\partial t} = D \left(\frac{\partial^2 T}{\partial r^2} + \frac{1}{r} \frac{\partial T}{\partial r} + \frac{1}{r^2} \frac{\partial^2 T}{\partial \theta^2} + \frac{\partial^2 T}{\partial y^2} \right).$$

Applying the quasi-steady state approximation and assuming homogeneity in all but the radial direction, this reduces to:

$$\frac{\partial^2 T}{\partial r^2} + \frac{1}{r} \frac{\partial T}{\partial r} = 0.$$

The solution must be of the form

$$T(r, t) = A + B \log r.$$

As before, the interface r' is constrained to the freezing temperature T_f , but instead of applying the Wilson-Frenkel law at the interface, we apply Newton cooling:

$$T(1, t) + \beta \frac{\partial T(1, r)}{\partial r} = 1.$$

In terms of the unknowns these constraints translate to:

$$\begin{aligned}
A + B \log 1 + \beta \frac{B}{1} &= A + \beta B = 1 \\
A + B \log r' &= T_f.
\end{aligned}$$

We can then solve for A and B :

$$\begin{aligned}
A &= -\frac{(1 - T_f) \log r'}{\beta - \log r'} \\
B &= \frac{1 - T_f}{\beta - \log r'}
\end{aligned}$$

Thus the heat field solves to:

$$T(r, t) = \frac{\log r - (1 - T_f) \log r'}{\beta - \log r'}$$

Inserting this into the second equation of the Stefan problem yields:

$$\frac{dr'}{dt} = -D \frac{\partial T}{\partial r'} = \frac{-D}{r'(\beta - \log r')}.$$

This equation can be integrated if first inverted,

$$\frac{dt}{dr'} = \frac{-r'(\beta - \log r')}{D},$$

and then integrated with respect to r' to get an ‘arrival time’ equation:

$$t(r') = \frac{1}{4D} (2(r')^2 \log r' - (1 + 2\beta)(1 - (r')^2)).$$

The identity $\int x \log x \, dx = \frac{x^2}{2} (\log x - \frac{1}{2})$ was applied in order to perform this integration. Intuitively, this equation describes the time at which the interface will arrive at some radius r' . Instead of performing this final integration, I will later use a thin-film variant of the $\frac{dr'}{dt}$ equation, because this form is better suited for a level set simulation.

2.4 Related Work In Graphics

2.4.1 Phase Transition

Phase transition is a relatively new topic in computer graphics, because until recently, robust, efficient solvers for objects of a single state were not commonly available. Clearly, it would be difficult to simulate an object transitioning from solid to liquid in the absence of robust rigid body and fluid simulators.

In particular, recent techniques used for fluid simulation are relevant to this dissertation, since I use many of the same techniques to track the rapidly evolving ice surface. Early work in fluid simulation solved the Navier-Stokes equations using the Marker-In-Cell (MAC) method (Foster and Metaxas, 1996) from computational fluid dynamics (Harlow and Welch, 1966), and also efficiently solved the shallow water equations (Kass and Miller, 1990).

In his seminal 1999 paper, Stam described a fast, unconditionally stable method of simulating the Navier-Stokes equations (Stam, 1999b). Subsequently, considerable research effort has been devoted to building on Stam’s ideas and formulating alternative approaches. Free boundaries were added to take into account pouring and splashing (Enright et al., 2002b; Foster and Fedkiw, 2001), and the concept of ‘vorticity confinement’ was introduced to counteract numerical smearing (Fedkiw et al., 2001). An efficient method of simulating smoke and water on an octree data structure was also introduced (Losasso et al., 2004). I will later use similar techniques for icicle simulation.

With this increased interest in fluid simulation, the problem of phase transition has also received attention. Carlson et al. (Carlson et al., 2002) presented a MAC method of simulating variable viscosity fluids which could handle situations such as wax melting. The key idea was to treat solid objects as liquids with very high viscosity, and a similar approach was taken in later work (Carlson et al., 2004) to simulate the interaction of rigid objects with fluid. Alternatively, Wei et al. (Wei et al., 2003) presented a Lattice-Boltzmann based methods for simulating melting. Subsequently, Rasmussen et al. (Rasmussen et al., 2004) described an IMEX scheme for the viscous

forcing terms involved in melting simulations, and Losasso et al. (Losasso et al., 2005) described a method of melting Lagrangian solids into Eulerian liquids.

Other work has also dealt with visco-elastic objects that possess viscosities much higher than water, but still exhibit flowing behavior (Goktekin et al., 2004; Clavet et al., 2005). These works do not appear to handle large viscosity transitions however, so the methods are not directly applicable to solidification.

2.4.2 Modeling Winter Scenes

The problem of modeling a winter scene has received attention in graphics because it gives rise to a unique set of challenges. Fallen snow has a specific geometric shape that cannot be captured by simply offsetting existing scene geometry. More sophisticated, physically-based approaches have been attempted such as the use of metaballs (Nishita et al., 1997), and a ‘visible sky’ algorithm (Fearing, 2000) that is similar to the ambient occlusion algorithm in global illumination. Recent work has also successfully modeled the appearance of snow falling from the sky (Langer et al., 2004).

Modeling ice formation in these scenes has not been as closely examined. To my knowledge, the only work that bears some resemblance to that presented here is by Kharitonsky and Gonczarowski (Kharitonsky and Gonczarowski, 1993). They described a random-walk model of icicle growth, where water droplets walk along an ice surface and freeze with a certain probability. However, their approach does not naturally handle the formation of more than one icicle. More seriously, the notion that icicles form as the aggregate of discrete droplets is not empirically supported.

2.4.3 Pattern Formation

While the specific goal of this dissertation is the modeling of ice formations, in a more general sense, the problem of solidification is one of *pattern formation*. Formally, physicists define pattern formation as when “nonlinearities conspire to form spatial patterns that sometimes are stationary, travelling or disordered in space and time.”

(Bodenschatz et al., 2003). In this sense, the work in this dissertation is one of many pattern formation algorithms in computer graphics. The patterns that form in fluid simulation, for example, fall into this category due to the non-linear advection term. Visual phenomena that arise as a consequence of flow, such as sand dunes and rust patterns (Dorsey et al., 1996; Chen et al., 2005) meet this criteria as well.

Closely related to the phase field equations to be presented in Chapter 3 are reaction-diffusion systems. Pattern formation in reaction-diffusion systems was first described by Turing (Turing, 1952). The notion is counter-intuitive, because diffusion is usually thought of as a physical mechanism that smears out detail, not one that gives rise to it. However, Turing showed that when coupled with the appropriate reaction terms, sharp, standing wave solutions could be obtained. The formation mechanism has since been dubbed ‘Turing instability’ in physics. Reaction-diffusion was introduced to graphics by two articles that were published concurrently: (Witkin and Kass, 1991) and (Turk, 1991). The first article (Witkin and Kass, 1991) described how to simulate reaction-diffusion over a rectilinear grid. However, when this grid is stretched over a model, it experiences significant distortion, so a distortion correction technique was described as well. The second article (Turk, 1991) circumvented the distortion problem by generating a Voronoi diagram on the surface of the model in lieu of a rectilinear grid and then solved the reaction-diffusion equations over the diagram instead. Reaction-diffusion equations have the form:

$$\frac{\partial A}{\partial t} = D_A \nabla^2 A + R(A).$$

The symbol A denotes some chemical, D_A is its diffusion constant, and $R(A)$ is some reaction equation. A reaction-diffusion system is obtained when two chemicals are coupled via their reaction terms. For example:

$$\begin{aligned}\frac{\partial A}{\partial t} &= D_A \nabla^2 A + R(A, B) \\ \frac{\partial B}{\partial t} &= D_B \nabla^2 B + R(A, B).\end{aligned}$$

In fact, the phase field equations can be viewed as a special case of reaction diffusion. In both cases, non-trivial patterns form from initially homogeneous concentrations due to non-linearities in the reaction equations.

DLA, the algorithm that will be presented in Chapter 4 has also been applied to pattern formation in other phenomena, such as lichen growth (Sumner, 2001; Desbenoit et al., 2004). DBM, which also be described in Chapter 4 has been used to simulate lightning (Kim and Lin, 2004). In both of these cases, the non-linearity arises from the implicit presence of Eqn. 1.2 in the simulation.

Algorithms similar to DLA have also been developed in graphics. The non-linearities in these algorithms are not as readily apparent as in DLA, but given the algorithmic and visual similarities, they seem likely. Ballistic deposition, a simplified version of DLA, has been used to model the formation of patinas (Dorsey and Hanrahan, 1996), and a novel venation algorithm that bears resemblance to DLA has been proposed (Runions et al., 2005).

Chapter 3

The Phase Field Method

In this chapter, I describe one method of solving the Stefan problem, the *phase field* method. The general approach of the phase field method was derived independent of the Stefan problem, using an approach that appeals more directly to thermodynamics. A summary of this free energy approach is available in the previous chapter. I will provide an overview of the phase field equations and describe how they intuitively map to the Stefan problem.

Additionally, I present techniques to simplify the phase field computation and make the problem of simulating ice crystal growth more tractable. I also show how the phase field method allows a user parameterization that a visual effects artist can use to manipulate the ice crystal growth. The phase field method often has smoothing artifacts as a result of its implicit representation, and it can only compute the outermost ice/water boundary. Therefore, a novel intermediate geometric processing step is introduced to add sharp edges and medial ridges to the interior of the ice. Finally, the simulated images are rendered using photon mapping (Jensen, 2001).

The basic simulation and rendering framework has been applied to several different scenarios. Fig. 3.1 shows an example image generated by the described method.

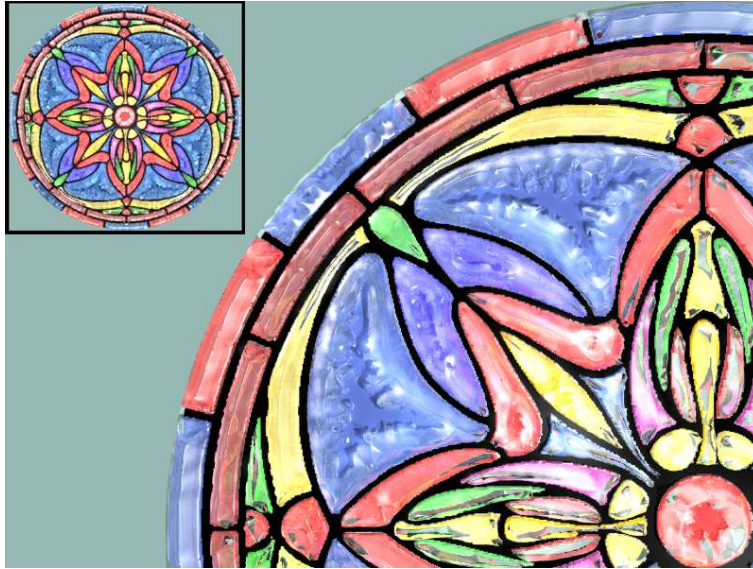


Figure 3.1: **Detail of ice grown on a stained glass window.** The inset shows the full window.

3.1 Overview

I will give a brief overview of the overall computational framework and the basic design of each step involved.

I use a simple and powerful implicit simulation technique from the crystal growth literature, known as the *phase field* method. This method can take $O(N^3)$ time, where N is the resolution of a single grid dimension. To obtain reasonable accuracy, N must be fairly large, making the computation quite expensive. I reduce the computation time significantly by using two acceleration techniques. The first is based on the observation that most ice crystals are very thin. I can simulate growth in 2D and add 3D detail later, reducing the computation time from $O(N^3)$ to $O(N^2)$. Second, I further improve the performance of the simulation by performing banded computation around the “front” of the ice and water interface, instead of over the entire grid.

I then adapt the phase field method to include aesthetic controls for a visual effects artist to manipulate. This is achieved by user control of the seed crystal and freezing temperatures input into the phase field simulation.

The visually salient features of our target object are used for the seed crystal. The features are extracted with edge detection and used to set the initial conditions of the simulation. In addition to seeding the simulation, I also influence the simulation throughout by manipulating the freezing temperature.

Due to the smoothing artifacts of the phase field method and the lack of internal detail given by the evolving interface, a novel intermediate geometric processing step is introduced to add sharp features prior to rendering. This is performed by first computing the border and medial axis of the ice with morphological operators. Given the resulting medial axis and boundary edges, I generate a constrained conforming Delaunay triangulation upon which a subdivision step is performed to introduce creases and edges (DeRose et al., 1998). Finally, the triangles are rendered using photon mapping (Jensen, 2001).

Fig. 3.2 shows the overall system pipeline of our computational framework.

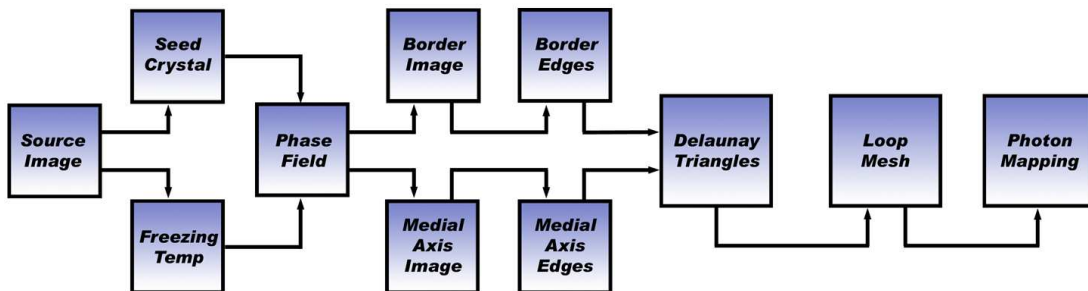


Figure 3.2: The overall system pipeline.

3.2 The Phase Field Method

In this section, I describe the *phase field* method, a numerical technique used to simulate undercooled ice growth. Phase fields are an implicit simulation technique that naturally track the complex geometry of a growing ice crystal. Additionally, they meet one of

the major objectives of this dissertation described in Chapter 1, as they are able to simulate the range of growth regimes between dendritic and sectorial plate growth.

Subsections [3.2.1] - [3.2.3] give an overview of the method, and present Kobayashi's formulation (Kobayashi, 1993). The relationship of phase field methods to the Stefan problem are described in subsection [3.2.4]. In subsections [3.2.5] - [3.2.8] I will present my own analysis and optimizations.

3.2.1 Undercooled Solidification

An undercooled liquid is a liquid that has been cooled below its freezing temperature, but has been cooled sufficiently slowly for it to remain in its liquid state. When a small amount of solid material, known as the seed crystal, enters a container filled with undercooled liquid, the liquid transitions to solid radially outwards from the initial seed in a rapid and unstable reaction. Due to this instability, the growth of the crystal can be influenced by small perturbations, such as surface tension or minute impurities in the liquid. These factors can lead to the complex branching, or "dendritic", behavior we see in ice.

3.2.2 The Phase Field

In the phase field method, the undercooled liquid is represented implicitly as a two or three-dimensional grid. This is also known as an 'Eulerian' representation. Many papers in computer graphics describe Eulerian simulation in detail (Witkin and Kass, 1991), as does any general applied linear algebra text (Demmel, 1997). For simplicity and tractability, I limit the simulations to two dimensions.

Two separate fields are tracked using this discrete representation: A temperature field T , records the amount of heat in a given cell, and a phase field p records the current phase of a given cell. For a given grid coordinate (x, y) , T_{xy} and p_{xy} are defined as the corresponding values in the temperature and phase fields.

For a given (x, y) , if $p_{xy} = 0$, the cell is filled with water, and if $p_{xy} = 1$, the

cell contains ice. If p_{xy} is between $[0, 1]$, then it is at an intermediate stage between the two states. While phase is usually thought of as a binary state, either water or ice, on the microscopic level there is a continuum of states along the ice front. The phase field method makes the computation of solidification tractable by magnifying this microscopic continuum so that it is visible macroscopically.

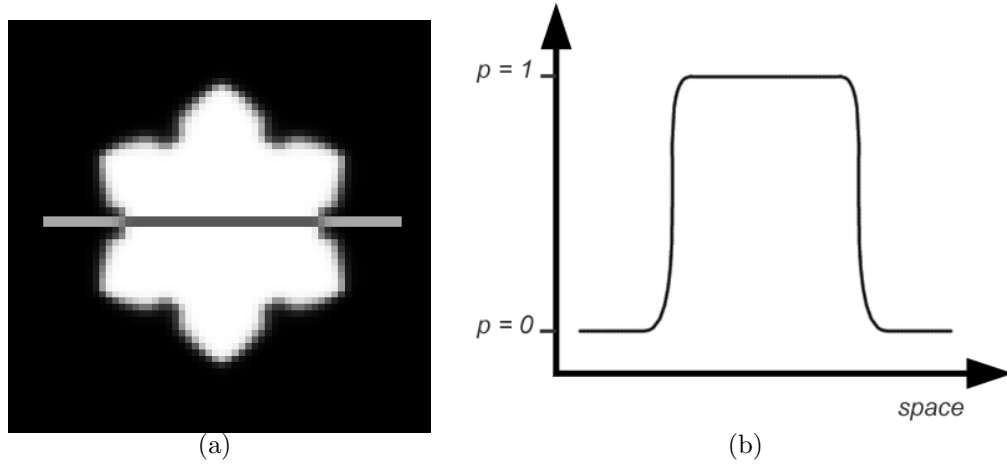


Figure 3.3: (a) A phase field in which white is $p = 1$ (ice), and black is $p = 0$ (water). The gray band in the middle is the section shown in profile in (b). (b) Cross section from (a) in profile. Note that while the transition from water to ice is abrupt, it is not instantaneous.

Fig. 3.3(a) is an example of a partially reacted phase field, and Fig. 3.3(b) is a cross section from Fig. 3.3(a). The horizontal axis of Fig. 3.3(b) is the spatial dimension, and the vertical axis is the phase dimension. In actuality, the transition from $p = 1$ (ice) to $p = 0$ (water) should be a microscopically thin, virtually instantaneous step function. Instead, the microscopic transition has been magnified, and we can see a region of quick but finite transition. Once the interface has been magnified to a resolution where non-integral values of p_{xy} appear on the grid, we can evolve the interface by applying a pair of partial differential equations.

3.2.3 The Kobayashi Formulation

The first paper to report successful simulation of a wide variety of ice growth patterns using phase fields is by Kobayashi (Kobayashi, 1993). His formulation is similar to the reaction-diffusion equations (Witkin and Kass, 1991; Turk, 1991) for texture synthesis in computer graphics. In reaction-diffusion, the propagation of chemicals through a medium is described using a pair of PDEs of the form:

$$\frac{\partial C}{\partial t} = D\nabla^2 C + R.$$

On the right hand side, $D\nabla^2 C$ represents diffusion, and R represents an arbitrary reaction function. The a^2 is a spatially-variant anisotropy term. The PDE for Kobayashi's temperature field fits this form:

$$\frac{\partial T}{\partial t} = D\nabla^2 T + K \frac{\partial p}{\partial t}. \quad (3.1)$$

The diffusion term remains the same, since we are in fact simulating heat diffusion. In this case, $R = K \frac{\partial p}{\partial t}$, where K is a latent heat constant. This R term models the process where, as water transitions to ice, it produces heat.

The phase field term in Kobayashi's formulation is significantly more complex than the previous equations:

$$\begin{aligned} \tau \frac{\partial p}{\partial t} = & \nabla \cdot (\varepsilon^2 \nabla p) - \frac{\partial}{\partial x} \left(\varepsilon \frac{\partial \varepsilon}{\partial \theta} \frac{\partial p}{\partial y} \right) + \frac{\partial}{\partial y} \left(\varepsilon \frac{\partial \varepsilon}{\partial \theta} \frac{\partial p}{\partial x} \right) + \\ & p(1-p) \left(p - \frac{1}{2} + m(T) \right). \end{aligned} \quad (3.2)$$

The first portion is a diffusion term:

$$\nabla \cdot (\varepsilon^2 \nabla p) - \frac{\partial}{\partial x} \left(\varepsilon \frac{\partial \varepsilon}{\partial \theta} \frac{\partial p}{\partial y} \right) + \frac{\partial}{\partial y} \left(\varepsilon \frac{\partial \varepsilon}{\partial \theta} \frac{\partial p}{\partial x} \right)$$

that is significantly more complex than the standard Laplacian. The standard Laplacian

diffusion term ($\nabla^2 C$) is the sum of the diagonal elements of the *Hessian* matrix:

$$\begin{bmatrix} \frac{\partial^2 p}{\partial x^2} & \frac{\partial^2 p}{\partial x \partial y} \\ \frac{\partial^2 p}{\partial y \partial x} & \frac{\partial^2 p}{\partial y^2} \end{bmatrix}. \quad (3.3)$$

The Kobayashi diffusion term is also the sum of elements from the Hessian, but while the off-diagonal entries usually cancel each other out, the Kobayashi formulation involves a diffusion tensor where this cancelation does not occur. The placement of the anisotropy term is also different, between the first and second partials. As a result, the diagonal terms are abbreviated as a gradient and divergence operator ($\nabla \cdot (\varepsilon^2 \nabla p)$) instead of a pure Laplacian. This difference is significant, because $\nabla \cdot (\varepsilon^2 \nabla p) = \varepsilon^2 \nabla^2 p + \nabla \varepsilon^2 \cdot \nabla p$. As a result, this different anisotropy placement accounts for both the Laplacian of the phase term and the gradient of the anisotropy term.

Kobayashi also presents a complex and general model of anisotropy. First, we define θ as the orientation of the front at a given grid cell, $\theta = -\nabla p$. In two dimensions, this reduces to $\theta = -\cos^{-1}(\frac{\frac{\partial p}{\partial x}}{|\nabla p|})$. The anisotropy term is then

$$\varepsilon(\theta) = \bar{\varepsilon}(1 + \delta \cos(j(\theta_0 - \theta))) \quad (3.4)$$

where $\bar{\varepsilon}$, δ , j , and θ_0 are constants. The constant j is the degree of anisotropy, which defines preferred directions of growth. δ is the strength of anisotropy, which defines the speed of growth in the preferred directions. θ_0 is a fixed reference direction, and $\bar{\varepsilon}$ is the scaling factor that determines how much the microscopic front is magnified. The values used for these and other constants is given in Table 3.1. The $\frac{\partial \varepsilon}{\partial \theta}$ term is also necessary in Eqn. 2, but this can be obtained by taking the analytical derivative of Eqn. 3.4.

α	γ	T_e	j	θ_0	$\bar{\varepsilon}$	τ	D
0.9	10.0	1.0	4.0	$\frac{\pi}{2}$	0.01	0.0003	1.0

Table 3.1: Simulation Constants. **Top:** Equation symbols; **Bottom:** Values used

Next we examine the reaction term in Eqn. 2.

$$p(1-p) \left(p - \frac{1}{2} + m(T) \right), \quad (3.5)$$

where the m term is defined as:

$$m(T) = \frac{\alpha}{\pi} \arctan(\gamma(T_e - T)). \quad (3.6)$$

Eqn. 3.5 models the energy potentials in the system. The details of this equation are probably of limited use to a graphics audience, so we will instead present some basic intuition. When $m = 0$, Eqn. 3.5 is positive over $0.5 < p < 1$ and negative between $0 < p < 0.5$. So, the energy is in a “meta-stable” state where values of p are encouraged to stay the same. Conversely, when $m = 0.5$, Eqn. 3.5 is positive for all $0 < p < 1$. So, if a grid cell has $m = 0.5$, no matter what its p value, it is encouraged to transition towards ice. As the temperature of a grid cell increases, its m increases towards 0.5, and it becomes more likely to transition to ice.

Despite the complexity of the above discussion, Eqns. 1 and 2 are all that are necessary to simulate ice growth. I will not present a method of synthesizing ice onto 3D objects here, because the 2D texture synthesis methods presented by Witkin et al. (Witkin and Kass, 1991) and Turk (Turk, 1991) can both be applied without modification.

3.2.4 Relation to the Stefan Problem

The phase field method as just described corresponds to the *two sided* Stefan problem with *surface tension anisotropy*. This flavor of the Stefan problem is defined by its complex boundary conditions, and is considered difficult because it involves tracking an evolving ice/water boundary while simultaneously enforcing conditions along this boundary. The strength of the phase field method is that it instead embeds these boundary conditions in the evolution equations. By integrating the evolution equations, the boundary conditions are automatically enforced.

Compare the phase field heat equation (Eqn. 3.1) with the usual heat equation

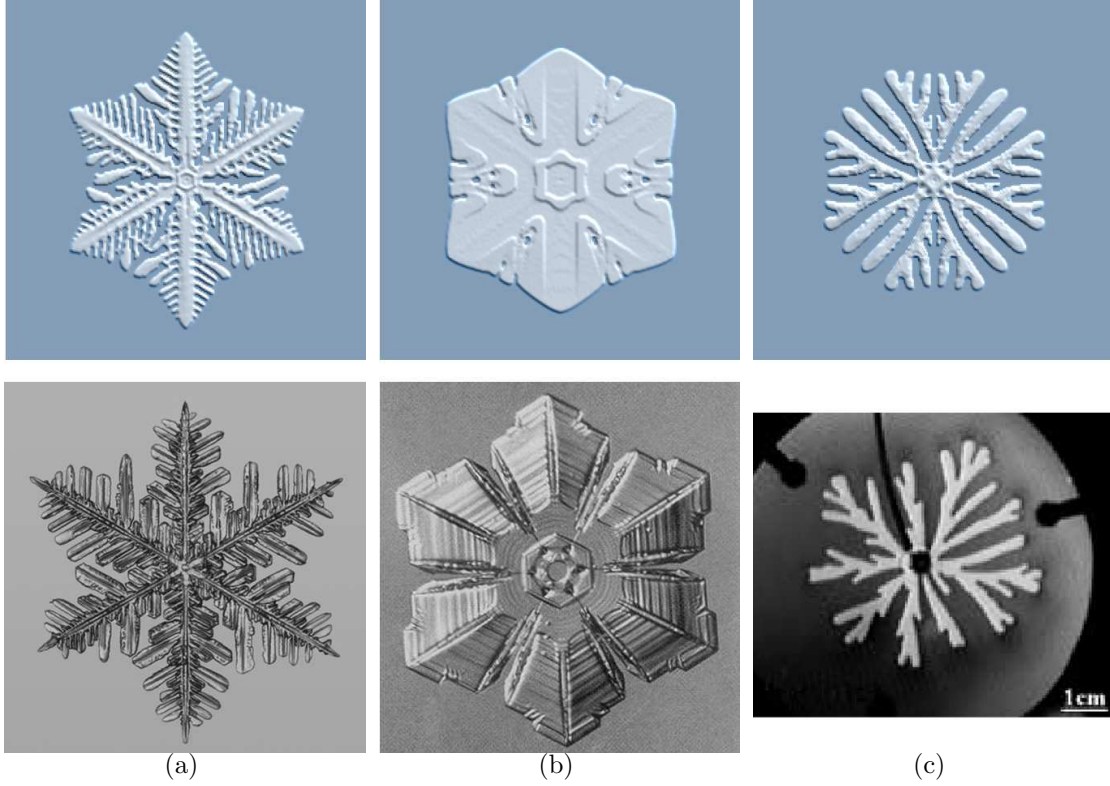


Figure 3.4: **Top:** Different simulated structures from the ice morphology. **Bottom:** Photographs for comparison. (a) *Dendritic* growth (b) *Sectorial Plate* growth (c) *Isotropic* growth. Isotropic growth is not usually found in nature, because it is rare that no bias acts on growth. However, it can be produced in a laboratory using an electric field, as in this photo from Buka (Buka et al., 2001).

(Eqn. 5.1) associated with the Stefan problem:

$$\begin{aligned}\frac{\partial T}{\partial t} &= D\nabla^2 T + K\frac{\partial p}{\partial t} \\ \frac{\partial T}{\partial t} &= D\nabla^2 T.\end{aligned}$$

Clearly the only difference is the $K\frac{\partial p}{\partial t}$ term, which corresponds to the latent heat released during the liquid to solid phase transition. The $\frac{\partial p}{\partial t}$ term is only non-zero along the ice/water boundary, so this term only ‘activates’ along the interface, essentially becomes a boundary condition. Other simulation methods, such as level set methods

(Gibou et al., 2003) instead extract the location of the ice/water boundary explicitly, compute quantities along the boundary, and then insert these quantities back into the simulation. While there are many advantages to this approach, it is a good deal more complex than simply Euler integrating Eqn. 3.1.

The phase evolution equation can be viewed in a similar manner. For simplicity, let us first examine the zero surface tension case of Eqn. 3.2, where $\varepsilon = 0$.

$$\tau \frac{\partial p}{\partial t} = p(1-p) \left(p - \frac{1}{2} + m(T) \right). \quad (3.7)$$

Again, this equation is only non-zero along the boundary. The $p(1-p)$ portion of the cubic forces roots to occur at $p = 0$ and $p = 1$, guaranteeing that this equation is only non-zero at in between values of p .

If we re-introduce the surface tension function $\varepsilon(\theta)$, a compact method of writing Eqn. 3.2 is:

$$\tau \frac{\partial p}{\partial t} = \nabla \cdot (\Phi \nabla p) + p(1-p) \left(p - \frac{1}{2} + m(T) \right), \quad (3.8)$$

where Φ is the diffusion tensor:

$$\Phi = \begin{bmatrix} \varepsilon^2 & -\varepsilon \frac{\partial \varepsilon}{\partial \theta} \\ \varepsilon \frac{\partial \varepsilon}{\partial \theta} & \varepsilon^2 \end{bmatrix}. \quad (3.9)$$

This equation corresponds to the interface evolution of the Stefan problem (Eqn. 1.6),

$$\frac{\partial \Gamma}{\partial t} \cdot \mathbf{n} = D \frac{\partial T}{\partial \mathbf{n}} s(\theta), \quad (3.10)$$

where $s(\theta) = \varepsilon(\theta)^2$. The correspondence is perhaps not immediately apparent, but can be illustrated using a simpler anisotropy function, $s(\theta) = \varepsilon(\theta)^2 = 1$. In this case, the isotropic interface equation is retrieved,

$$\frac{\partial \Gamma}{\partial t} \cdot \mathbf{n} = D \frac{\partial T}{\partial \mathbf{n}}, \quad (3.11)$$

and the phase evolution equation reduces to

$$\tau \frac{\partial p}{\partial t} = \nabla^2 p + p(1-p) \left(p - \frac{1}{2} + m(T) \right). \quad (3.12)$$

The phase evolution equation is now essentially a diffusion equation, a physical process that naturally evolves in the normal direction. Therefore, we can think of p as a smeared out version of Γ , and view the $\cdot \mathbf{n}$ term on the left hand side of Eqn 3.11 as implicit in the ∇^2 term in Eqn. 3.12. We do not want p to smear out Γ too much however, since it is still supposed to correspond to a sharp interface. The cubic equation on the right hand side of Eqn. 3.12 can be thought of as a ‘sharpening’ term that prevents the diffusion operator from smearing out the interface too badly.

This intuition remains essentially the same even if a more complex anisotropy function is used. The smeared out Γ function evolves via diffusion, and the only difference is that the diffusion has been biased in certain preferred directions.

3.2.5 Improved Anisotropy

Eqn. 3.4 affords both simpler and richer controls for general texture synthesis than the anisotropy term described by Witkin and Kass (Witkin and Kass, 1991). Witkin and Kass’ formulation limits the number of preferred growth directions to 0, 2, or 4, and all the directions must be either parallel or orthogonal. Additionally, the strength of anisotropy in parallel directions must be the same. For example, if we prefer fast growth along the x axis, we cannot specify different speeds for the positive and negative directions.

Using the constant j in Eqn. 3.4, we can specify an arbitrarily high degree of anisotropy, and with a slight modification, specify a different speed for each direction. This is accomplished by defining a separate δ_i for each i^{th} cosine lobe, and limiting the influence of δ_i to the range $\frac{i*2\pi}{j} \leq \theta < \frac{(i+1)*2\pi}{j}$.

3.2.6 Possible Ice Crystal Shapes

In Fig. 4, I show the results of the simulation, starting from a point source of ice in the center. By varying the K and δ simulation parameters, I can produce the “isotropic”, “sectored plate”, and “dendritic” types from the ice morphology. For comparison, I provide photos of snowflakes that illustrate these same types. Although snowflakes form from vapor, not undercooled melts, the process of solidification is similar, and serve to show that our results are in close agreement with naturally occurring structures.

3.2.7 Banded Optimization

A good deal of the computation in the simulation is extraneous, because in many cases a large portion of the phase field grid is homogeneously ice or water. Eqn. 3.1 and 3.2 are only nonzero in regions where the phase field is heterogeneous, so any computation time spent in homogeneous regions is wasted.

Some of the optimization techniques that have been proposed for phase field methods. For example, adaptive mesh refinement techniques (Provatas et al., 1999) have been used to increase the resolution of the solution around regions of interest. Additionally diffusion Monte Carlo techniques (Plapp and Karma, 2000) have been used to track the heat field far from the interface, resulting in significant computational savings. Far from the interface, heat is tracked as a set of particles whose dynamics are much cheaper to compute than fluxes over a mesh. However, these techniques also deal with the accurate simulation of solidification at scales much smaller than the mesh resolution. Since I am only concerned with visual simulation, these smaller scales are not of interest.

The optimization that is of interest in the adaptive mesh and DMC methods is the localization of computation to the grid cells along the interface. This goal can be achieved using a simple method, similar to the “narrow band” optimization method used for level set methods (Adalsteinsson and Sethian, 1995a). In the narrow band level set method, instead of solving over the entire computational domain, computation is

restricted to a narrow band of grid cells surrounding the region of interest. The region of interest in level set methods is usually a small neighborhood around the $\phi = 0$ level set. In phase fields, a similar method could be used because the region of interest is the $p = 0.5$ isocontour. Since all computation takes place using finite differencing, the interface can move a maximum of one grid cell per iteration. If I restrict computation to grid cells that had a nonzero derivative on the previous iteration and their corresponding neighbors, then I will restrict computation of Eqn. 3.1 and 3.2 to only those grid cells that could potentially change. This simple and effective optimization offers the same computational localization as the adaptive mesh and DMC methods, while adding minimal implementation complexity.

Table 3.2 compares banded and unbanded performance. I used the simulation from Figure 3.2(a) as the test case, and ran all of the simulations to the same physical time on a 1.73 Ghz Pentium 4. As the resolution was increased, the number of iterations are increased because the size of the timestep is reduced to maintain numerical stability. As the resolution increases, the performance gain of the banded method appears to level off at about 5.5x. This performance gain will vary based on the input, but significant performance gains should be observed in all but the most pathological cases.

At first glance, it appears that the performance gain should continue to increase as the resolution increases. While this may be true for the narrow band level set method, it is not for narrow band phase fields. In narrow band level sets, a neighborhood several grid cells thick need to be maintained around the interface. As the resolution increases, the grid cell sizes decrease and the physical thickness of the narrow band decreases as well. In the case of phase fields, I am tracking a band of values where the time derivative is non-zero, such as regions with significant heat flow. These regions do not shrink as the grid is refined. The fractional area of the simulation domain that they occupy remains static, which is why the speed gain levels off as the resolution increases. The narrow band takes up about 20% of the simulation domain, regardless of the grid resolution. Faster performance at lower resolutions can probably be attributed to memory hierarchy effects.

Grid Size	Iterations	Unbanded	Banded	Speedup
128^2	500	8s	1s	8.0x
192^2	750	22s	2s	11.0x
256^2	1000	45s	4s	11.0x
320^2	1250	1m 14s	8s	9.2x
384^2	1500	2m 15s	19s	7.1x
448^2	1750	3m 10s	28s	6.8x
512^2	2000	4m 28s	42s	6.3x
576^2	2250	6m 2s	59s	6.1x
640^2	2500	8m 22s	1m 20s	6.3x
704^2	2750	10m 15s	1m 45s	5.9x
768^2	3000	12m 47s	2m 16s	5.6x
832^2	3250	15m 57s	2m 50s	5.6x
896^2	3500	20m 41s	3m 39s	5.7x
960^2	3750	23m 20s	4m 18s	5.4x
1024^2	4000	29m 39s	5m 19s	5.6x

Table 3.2: Banded vs. Unbanded Performance. I ran the same simulation at different resolutions. Higher resolutions required more iterations because of timestep restrictions. The speed gained from the banded version appears to level off at about 5.5x.

If the simulation is run long enough, the ice will expand to engulf most of the simulation domain. In this case, most of the domain will also be near a $p = 0.5$ isocontour, and the banded optimization will offer no significant speed advantage. However, almost all simulations start with little to no ice anywhere in the domain, and this is when the localization of the banded optimization offers the most drastic performance benefits. From a design standpoint, the initial stage of ice growth are also the part of the simulation that must run the fastest. When designing ice patterns, the ability to quickly preview the results of a parameter change is crucial to a smooth workflow.

3.2.8 Hardware Implementation

Recently, the efficient solution of PDEs has become practical on programmable graphics hardware. Kobayashi’s equations can be plugged directly into the general solution framework presented by Harris et al (Harris et al., 2002). Programmable graphics hardware, also known as graphics processing units (GPUs) excel at certain types of

computation, eclipsing the performance of equivalent algorithms on traditional CPUs many times over. This performance boost stems from the fact that GPUs were designed to exploit the SIMD (Single Instruction, Multiple Data) nature of scanline rendering. Scanline rendering is an inherently parallel computation, since each individual pixel in a rendered frame only depends on the scene geometry, and does not rely on the values of neighboring pixels. Therefore, the values of multiple pixels can be computed simultaneously, and the same result as a serial computation is obtained. By using multiple ‘pixel pipelines’, graphics hardware exploits this parallelism and processes several pixels in the same clock cycle. Although the clock speeds of GPUs is still currently less than those of CPUs, this parallelism results in significantly higher performance.

While earlier generations of graphics hardware only allowed a limited set of functions to be performed on the hardware, newer generations have allowed the use of more general programs. Many algorithms besides scanline rendering contain an inherent parallelism, so by mapping them to graphics hardware, large performance benefits can be obtained. Such applications include collision detection (Govindaraju et al., 2003), paint simulation (Baxter et al., 2004), and direct (Galoppo et al., 2005) and iterative (Bolz et al., 2003) linear solvers.

The phase field method also maps well to graphics hardware. Since it deals mainly with finite differences, its domain of data dependence is restricted, allowing SIMD computation. Notably, solidification using the level set method does not share the same natural mapping to GPUs, because it usually involves computing a distance field using the fast marching method (Sethian, 1999), which is an inherently serial operation. While alternate methods of computing distance fields on the GPU do exist (Sud et al., 2004), the fact remains that phase fields do not require any similarly special considerations. Instead, phase fields can be computed using two fragment programs, which are short enough to be listed in Appendix A.

On a high level, the GPU simulation proceeds in two stages. There are two textures, a ‘phaseField’ texture with the p and T variables respectively packed into the red and green channels, and an ‘eField’ texture that contains the value of ε from Eqn.

3.2. The textures are drawn as a screen-filling quad so that there is a one-to-one correspondence between pixels and texels. When the GPU executes a fragment program on a pixel, it is then running the fragment program on a texel. Multiple values from ε are computed simultaneously by running a fragment program over each of the texels in the ‘phaseField’ texture and computing the appropriate gradients by performing neighbor lookups. The neighbor lookups are efficient because they are essentially texture filtering operations, which GPUs are designed to perform quickly. The ‘eField’ texture is then sent to a second fragment program that computes the update for the p and T fields. The finite difference formulas for p and T also correspond to essentially texture filtering operations, so these updates can be done efficiently as well.

On a GeForceFX, I experienced as much as a factor of 9 speedup, making interactive simulation possible on non-trivial grid resolutions. Table 3.3 compares the two implementations. The timings are all for an unbanded implementation.

Grid Size	CPU (Hz)	GPU (Hz)	Speedup
64 x 64	250	624	2.50x
128 x 128	25	236	9.44x
256 x 256	8	67.47	8.43x
512 x 512	3.5	17.67	5.05x
1024 x 1024	1.08	3.77	3.49x

Table 3.3: CPU vs. GPU performance. CPU: 1.8 Ghz Pentium 4; GPU: GeForceFX 5800 Ultra

Banded optimization can also be implemented on hardware by terminating the fragment program as soon as the homogeneous phase case is detected. However, current GPUs do not yet appear to support this functionality, so we are unable to obtain timing information that leverages this optimization.

3.3 User Control

One of the goals of this simulation is to introduce a user parametrization into the simulation, so that a visual effects artist can suggest a general shape and the simulation

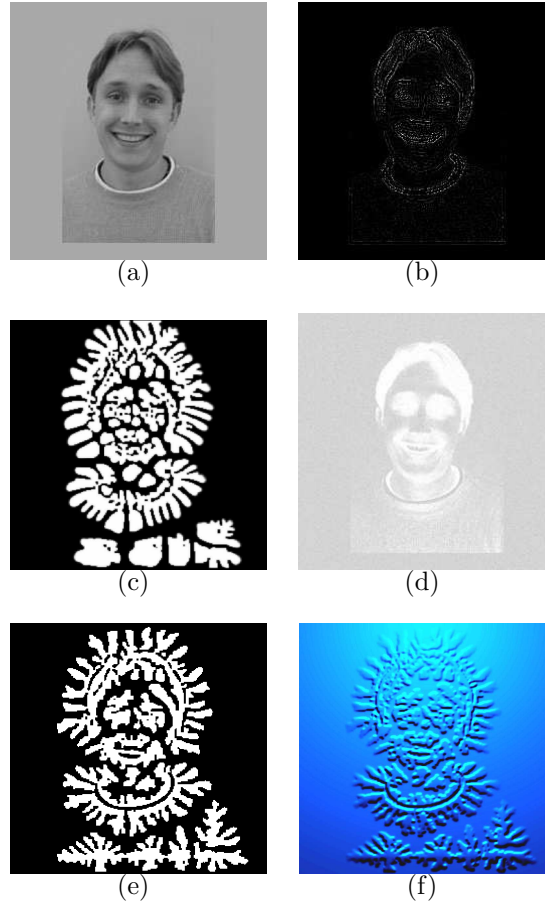


Figure 3.5: Left to right, top to bottom: (a) The source image; (b) the seed crystal texture; (c) simulation results after seed crystal mapping; (d) freezing temperature mapping: White regions are the original T_e value, while darker regions are lesser values; (e) the ice grown with a mapped seed crystal and freezing temperature; (f) the bump mapped ice.

can then grow an ‘icy’ version of the shape. The phase field method supports such a parameterization through the manipulation of its seed crystal and freezing temperature.

The seed crystal allows the user to guarantee that primary shape features are present in the final ice, and the freezing temperature allows the user to provide further simulation hints by rating the importance of secondary features. The settings for these parameters can be generated automatically using the methods suggested below, or interactively to give the user greater control over the final result. In order to illustrate how this works, I will grow ice in the shape of Fig. 3.5(a) as an example.

3.3.1 Seed Crystal Mapping

First, the user selects the most visually important features and maps them to the seed crystal. In this case, I decided that the edges of Fig. 3.5(a) were the most important visual feature. However, the user is free to select any arbitrary feature as the most important.

Fig. 3.5(b) was extracted using Canny edge detection (Canny, 1986). I map these visually important features to the seed crystal to guarantee that these features are present in the final ice, preserving the general shape of the original image. However, if the simulation is run on this seed crystal configuration, as shown in Fig. 3.5(c), the desired shape is quickly lost.

The seed crystal mapping only influences the initial condition of the simulation, so an additional parameter that influences the simulation at every timestep is also necessary in order for the goal shape to be preserved. The freezing temperature provides such a parameter.

3.3.2 Freezing Temperature Mapping

By varying the freezing temperature over the temperature field, we can model the presence of impurities in the undercooled liquid. Recall that salt causes ice to melt because it lowers the freezing temperature of the H_2O , and ice then transitions back to water if the surrounding environment is no longer cold enough to freeze it. Similarly, if salt were present in a undercooled liquid as it was freezing, the H_2O would be more reluctant to freeze in salty regions than in regions of pure water.

If we want to promote ice growth in a specific region of the phase field, we set the freezing temperature of that region as high as possible, to T_e . If we want to suppress all ice growth in a region, we can set the temperature of that region to zero. To rate the importance of regions with respect to one other, we can set their freezing temperatures between 0 and T_e .

For example, in Fig. 3.5(d), white regions represent T_e , while greyer regions repre-

sent progressively lower freezing temperatures. The hair, eyes, and collar in Fig. 3.5(d) are whiter than their surrounding regions, so these regions freeze over first before the simulation starts branching out into the greyer regions.

I automatically generated the freezing temperature texture in Fig. 3.5(d) by first populating the texture uniformly with the default T_e values, and then subtracted a scaled version of the original image. This method rates dark regions higher than light regions and produced good results. However, this is only one rating method, and since the simulation can use any arbitrary texture, the user can impose any desired rating method.

3.4 Introducing Internal Structure

In this section, I introduce physically-inspired internal structure to the results of the physically-based simulation. In the process, I will produce triangles from the results of the simulation that can be sent to a photon map renderer. This way I can capture one of the most striking features of ice, the caustics. Additionally, I will produce a subdivision surface representation that is capable of meeting the dense polygonal requirements of high-end visual effects work.

The phase field method provides the position of a growing ice border. However, there is also a good deal of interesting details that resides on the interior of ice as well. These details are apparent in the ‘snowflake’ images and simulations presented in Fig. 3.2.3. However, as the scale of the simulation is increased, these details are quickly lost, creating unnaturally flat ice.

3.4.1 Naïve bump mapping

In order to capture this internal detail, I first bump mapped the ice according to the $\frac{\partial p}{\partial t}$ of the ice. As water transitions to ice, it expands slightly, and this degree of expansion was approximated at each time step by increasing the height of the ice by the amount of phase transition. This is how the internal structures in Fig. 3.2.3 were produced.

However, this is a coarse approximation of the actual freezing process. The bumps in actual ice arise because of the expansion coefficient of water, which causes H_2O to increase slightly in volume as it freezes. This expansion coefficient arises due to forces at the water/air interface, not at the ice/water interface that $\frac{\partial p}{\partial t}$ is derived from. However, modeling the expansion coefficient is still an open problem in chemistry (Rebelo et al., 1998), and in my literature search I could not find a scientific model suitable for visual simulation and rendering. Consequently, I add a phenomenological step to introduce these additional features.

3.4.2 Adding Subdivision Creases

Once the simulation has run to completion, I introduce sharp internal structures by inserting creases into the ice at visually expected locations. The introduction of creases into a surface is a well-studied technique in modeling, specifically using subdivision surfaces (DeRose et al., 1998). I introduce creases into the ice by stretching a subdivision surface over the ice and then repeatedly subdividing to introduce creases both at the border and along the medial axis.

The border is an obvious location to introduce detail, since it accentuates the border generated by the simulation. I introduce creases at the medial axis because we expect ice to have sharply faceted, crystalline features. Phenomenologically, the medial axis is a good candidate location for this crease because it is the location of visually interesting features in other natural growth phenomena, such as the veins in leaves. More formally, the medial axis is guaranteed to be distant from the border, so we are assured a good distribution of creases.

3.4.3 Morphological Operators

I isolate both the border and medial axis through the use of morphological operators. This is a simple way to isolate both of these features, given that the final ice is stored as a nearly binary raster image. The image is easily converted to a purely binary image

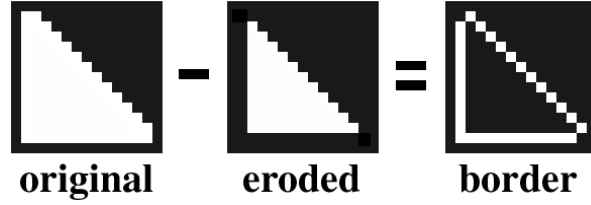


Figure 3.6: Border extraction operation

by thresholding all ($p \geq 0.5$) to 1 and ($p < 0.5$) to 0. In addition, morphological operators guarantee connectivity properties that greatly simplify the construction of a subdivision control mesh.

Morphological operations can be viewed as binary convolution. In place of the multiplications and additions of normal convolution, logical ANDs and ORs are respectively performed. The convolution kernels in morphological operations are referred to as “structuring elements”. See Jahne (Jahne, 1997) for a more detailed description.

I use erosion, one of the simplest morphological operations, to isolate the border of the ice. If we run a single iteration of erosion on an image, then a single layer of white pixels around all white regions is deleted. If we then subtract this eroded image from our original image, we are left with the border pixels of all the white regions in the original image. This process is shown in Fig. 3.6.

The usual structuring element for erosion is given in Fig. 3.7(a). However, we use a sparser version, given in Fig. 3.7(b). As shown in Fig. 3.8, the use of the sparser structuring element does not give us the thick band of pixels that are present using the traditional element. Instead, we get a sparser set of pixels with simpler connectivity, which as we will see later, leads to a simpler subdivision control mesh.

I also use morphological operators to extract the medial axis of the ice. While there exist many ways to extract the medial axis, using morphological operators is very simple and guarantees the same connectivity properties as erosion, resulting in a simple subdivision control mesh. The use of morphological operators is slower than other medial axis algorithms, but the difference is negligible compared to the running time of the phase field simulation. Therefore, the extra overhead is insignificant in the

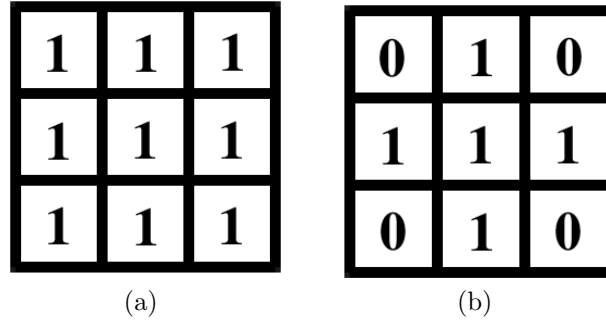


Figure 3.7: (a) 3 x 3 structuring element for morphological erosion; (b) The sparser operator we use

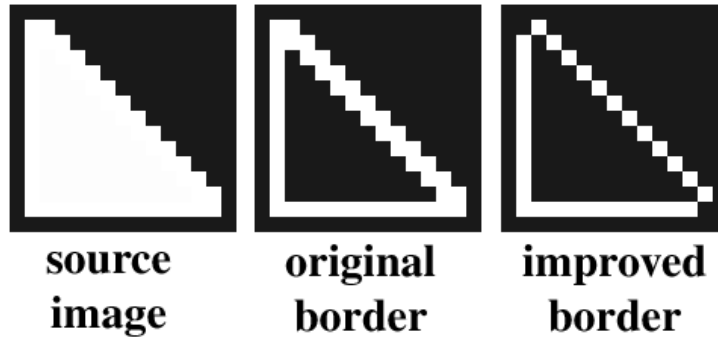


Figure 3.8: Results of modified erosion operator

overall computation time.

In morphological terms, the isolation of the medial axis is known as the “skeletonization”. The skeletonization operators in Fig. 3.9 are slightly more complex than the erosion operator. In addition to convolving by all eight structuring elements, the final value of the pixel is determined by ORing the results of all eight convolutions. The skeletonization operators also include “don’t care” pixels. The image pixels that fall under the “don’t care” pixels are ignored in all of the logical operations. In Fig. 3.9, the “don’t care” pixels are denoted with empty pixels.

The structuring elements in Fig. 3.9 are each run repeatedly until no further changes

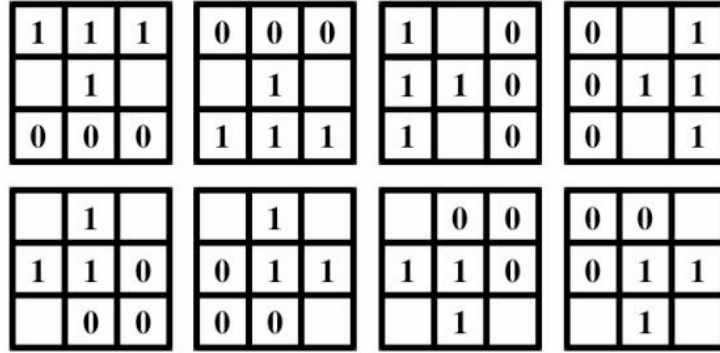


Figure 3.9: Skeletonization structuring elements

take place. When this occurs, the pixels that remain are those along the medial axis. Note that the “thick” formations in Fig. 3.8 are also guaranteed not to occur in the skeletonized image. I obtained Fig. 3.10(a) and (b) from the ice image, using the border and skeletonization morphological operators.

3.4.4 Control Mesh Segment Generation

To construct the control mesh for the subdivision surface, I first extract a set of line segments from the border and medial axis images. These line segments will be the crease edges in the subdivision surface, and their extraction is accomplished by performing a depth-first search of the white pixels in the images. According to Hoppe (Hoppe, 1994), there are three different vertex types at the endpoints of subdivision creases: “dart”, “crease” and “corner” vertices. We can automatically tag our vertices to the correct type during the depth first search.

For the medial axis image, we can create a minimally connected mesh by exploiting the properties given by the morphological operators, as shown in Fig. 3.11. Any white pixel with only one white neighbor is a “dart” vertex, any white pixel with two white neighbors is a “crease” vertex, and any white pixel with more than two neighbors is a “corner” vertex. I run a similar algorithm on the border image, but since we are not guaranteed to have any dart pixels, we can start the traversal from any white pixel.

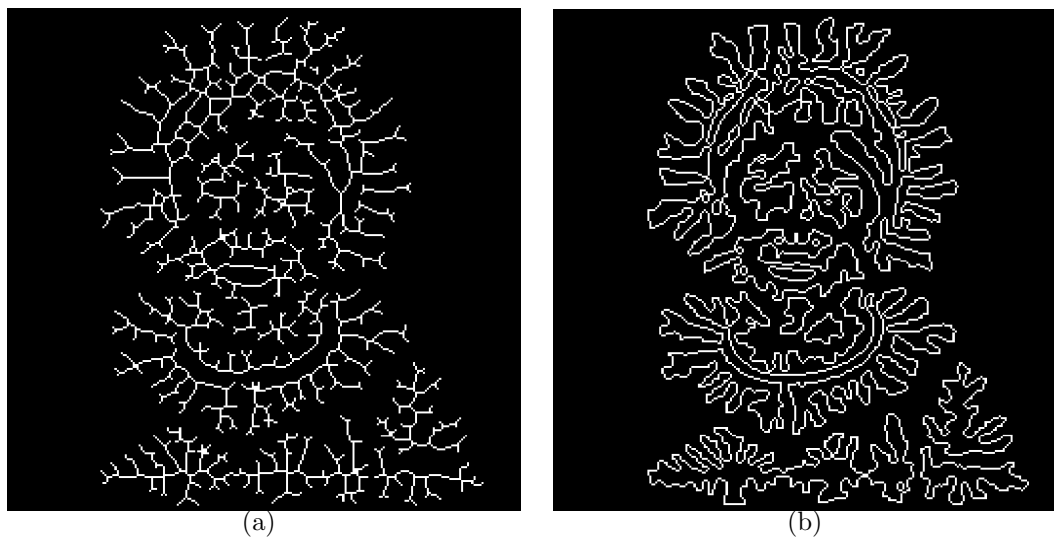


Figure 3.10: (a) Ice with skeletonization applied; (b) Ice with border operation applied

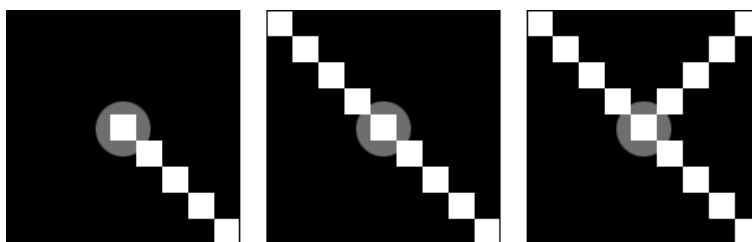


Figure 3.11: Crease pixel types (left to right): dart, crease, corner

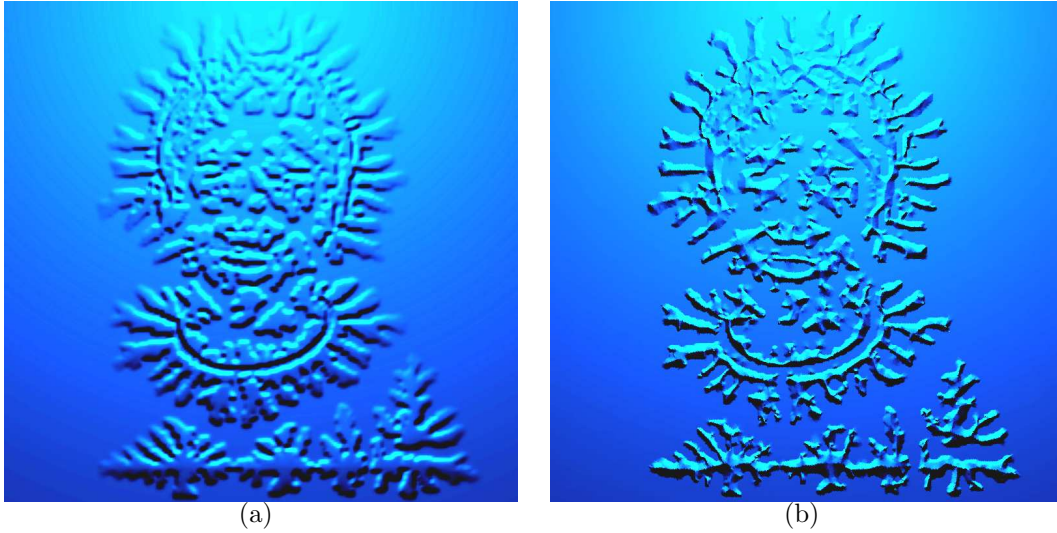


Figure 3.12: (a) The original bump mapped surface, (b) The sharpened ice surface after subdivision

Since there are not many darts or corners, I insert new vertices every so often, according to a “stride” length.

Note that if any of the “thick” structures from Fig. 3.8 had been present, then both dart and crease pixels would have two neighbors, and we would need a more complex search scheme. If we want to add more detail to the skeleton segments or avoid intersections with the border segments, we can add a “stride” to its tree traversal as well. In practice, setting the skeleton stride to the same as the border stride produced good results.

3.4.5 Triangulation Generation

Subdivision algorithms can only be run over tessellated surfaces, and the base primitive of the tessellation can vary. Several schemes can easily support creases, but I chose Loop subdivision because its base primitives are triangles, and there is a clearer path to generating triangles from the ice than generating other primitives.

A Delaunay triangulation algorithm takes a set of points and generates a set of triangles that contain the input points as vertices. I would specifically also like to

input a set of line segments, and generate a triangulation that contains both the points and lines. A specific variety of Delaunay triangulation, known as the “constrained Delaunay triangulation,” accomplishes this task. In practice, the basic constrained Delaunay triangulation generated many “needle” triangles, so I used the constrained conforming Delaunay triangulation instead.

3.4.6 Height Field Generation

Once we have a two dimensional triangulation of the ice, I must assign height values to the vertices in the triangulation. The obvious choice is to sample values from the original bump map. However, since the original bump map is very smooth, the limit surface of a subdivision mesh based on its values can also be very smooth.

In order to guarantee the appearance of creases in the limit surface, I assign the height values according to a linear interpolation that approximates a faceted surface. I generate this approximation by first calculating the distance to the nearest border and medial axis pixels for all pixels. I then assign a height value to the pixel by linearly weighting the heights of the nearest border and medial pixels by their relative distance from the current pixel. The heights of the border and medial pixels are taken from the original bump map. This approximation is very much like the *contour connection* approach in (Jones and Chen, 1994) and is simply a linear interpolation between the medial axis and border contours.

Note that for more performance-driven applications, such as games, this height field can be used as a normal map in place of the more expensive subdivision surface representation.

3.4.7 Crease Generation

If the linear interpolation is used to set the height values of the triangulation, then the creases are present in the ice from the very beginning, and can be further refined through subdivision. As specified in (DeRose et al., 1998), the creases can be made

infinitely sharp or made arbitrarily smooth. If the mesh is already too dense for further subdivisions, then the vertices of the triangulation can be positioned directly to the limit surface, using the masks given in (Hoppe, 1994). The results of the crease introduction step are shown in Fig. 3.12.

3.4.8 Rendering

Much of the interesting visual detail of ice is contained in the caustics generated by the refracting medium. To capture this detail, I used photon mapping for rendering (Jensen, 2001) the meshes generated by the detail reconstruction algorithm.

3.5 Implementation and Results

In this section, I give implementation details and present results generated on different scenes using my approach.

3.5.1 Implementation

All the pipeline stages were implemented in less than 5000 lines of C++ code, excluding the third party libraries cited below. Excluding the runtime library infrastructure, the hardware implementation took less than 100 lines of Cg code.

For the Constrained Delaunay Triangulations, I used Jonathan Shewchuk’s *Triangle* package (Shewchuk, 1996), a freely available Delaunay triangulation library that proved to be very well documented, easy to use, and highly optimized.

For rendering, I used POV-Ray 3.5, a freely available rendering application that supports a large shading language in addition to a nice photon map implementation.

In our banded optimization step, I found that I could not limit the band to cells with strictly greater than zero derivatives on the previous iteration. Since I use finite differencing to compute the derivatives, numerical noise quickly propagates through the field, giving slightly non-zero values everywhere. Instead, I limited the band to those

grid cells with a previous derivative greater than 10^{-7} .

3.5.2 Simulation Parameters

As mentioned earlier, the phase field simulation was run with the settings given in Table 3.1. The simulation ran successfully at the resolutions up to and including 2048 x 2048.

The time step was fixed to 0.0002 at all times. At larger steps, the numerical noise in the simulation quickly compounded. Other higher-order methods, such as Midpoint and Runge-Kutta Four integration, were attempted as well. However, they were unable to increase the timestep size by a factor that would have justified their cost.

3.5.3 Results

I successfully simulated ice growth in several scenes. All simulations took place on a 512 x 512 grid with the exceptions of Fig. 3.15, which was 512 x 800. The graphics hardware implementation runs at practically interactive rates, though its performance varies with the grid resolution.

The first scene is a pond with ice growing on a lily pad, as shown in Fig. 3.13. I ran this simulation for 800 iterations, taking a total of 45 seconds on a GeForceFX 5800 Ultra and averaging 0.06 seconds per iterations. The constant K was set to 1.2 and δ was set to 0.1. The scene was seeded with the veins of the lily pad, and the melting temperature was perturbed by the grey scale intensity of the original lily pad image.

The second scene is a stained glass window, with ice growing inwards from the lead frame. Since the lead would cool faster than the glass, this is a logical place to seed the ice. I ran the simulation for 600 iterations, taking a total of 34 seconds on the same GPU, taking approximately 0.06 seconds per iteration. The constant K was set to 1.2, and δ was set to 0.04. I also inserted a small amount of random noise into the freezing temperature map to promote non-uniform growth. Fig. 3.1 shows a detailed view on a portion of the stained glass with ice grown on it. See Fig. 3.17, Fig. 3.16 and 3.18 for a

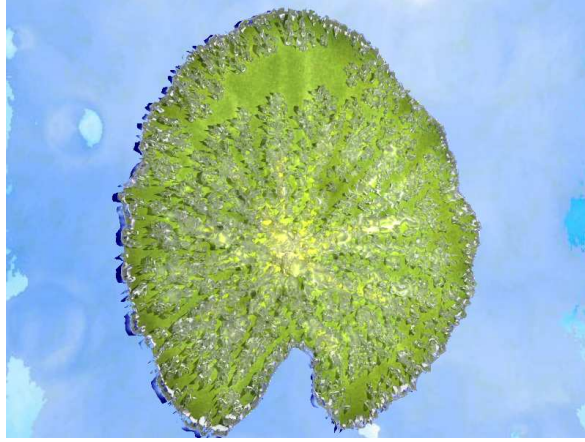


Figure 3.13: **Ice crystals grown on a lily pad:** The entire simulation took 45 seconds, with an average of 0.06 seconds per iteration.

sequence of snapshots from the simulation. Figures 3.17 and 3.16 are the same, except that the glass has been set to red in Fig. 3.16 to bring sharper relief to the ice pattern. Figure 3.18 shows the inside of the church as ice grows on the outside of the window. As the ice grows, the caustic cast by the window takes on an increasingly complex shape. This rendering is possible specifically because subdivision surfaces were used to explicitly generate triangles for photon mapping to trace.

The ring example, shown in Fig. 3.14(b), was run on the same GPU for 2300 iterations, taking a total of 130 seconds and averaging 0.06 seconds per iteration. The constant K was set to 1.2 and δ was set to 0.1. In order to promote non-uniform growth, noise was added to the melting temperature. Growth was prohibited on the inside and outside of the ring by mapping the melting temperature to a value lower than the T field could attain. In this way, growth can be clamped using solely user input, and no special considerations are necessary in the core phase field simulation. The bright ‘halo’ surrounding the ice is a caustic generated by the combined approach of subdivision surfaces and photon mapping.

A larger stained glass window with a more complex pattern is shown in Fig. 3.15. As before, the simulation was seeded along the lead frame of the stained glass, which would cool faster than the glass. I ran this simulation for 500 iterations, taking a total

of 50 seconds on the same processor, and averaging 0.1 seconds per step. The constant K was set to 1.2 and δ was set to 0.1.

3.5.4 Discussions and Limitations

Validating the results of the simulation is very challenging, as the simulation is very sensitive to noise. In fact, it is this sensitivity that gives rise to such interesting structures. Very specialized equipment is necessary to run any meaningful experiments, which I unfortunately do not have access to. However, the physical validity of the phase field methods has been proven repeatedly by researchers who have access to such equipment in the computational physics and crystal growth communities.

The reconstruction of the lost internal detail is only physically plausible, not physically based. Further study is necessary to validate and refine this process.

The user parameterization I have presented is capable of preserving a desired shape, but the phase field model can support additional parameters for greater user control. The latent heat constant K , and the strength of anisotropy δ , both influence the growth speed and the final shape of the ice, and their spatial mapping could be used to achieve different effects. Mapping the θ_0 parameter could also be used to suggest shapes, such as ice growth in a spiral. Additional work is necessary to determine useful input ranges for these parameters, and the effect that these settings have on performance.

With respect to rendering, I assumed homogeneous ice when in fact ice can exhibit subsurface scattering, spatially variant densities, and contain pockets of air in the form of bubbles or cracks. Some of these issues will be discussed further in chapter 5. The problem of subsurface scattering in inhomogeneous media is still an open question in rendering however, and solving this problem fully is beyond the scope of this dissertation.

The phase field method simulates several, but not all, forms of ice crystal growth. The method does not extend naturally to fully 3D ice formation such as icicles, and a fairly different approach will be necessary to capture these effects. The effect of external forces, such as gravity, wind, and fluid flow, also have the potential to produce

interesting results, and these possibilities will be examined in the next chapter.

While phase fields capture a wide variety of growth types, the size of the features that they can resolve has some strict limitations. The width of the smeared out solid to liquid transition region is directly proportional to the value of the $\bar{\epsilon}$ variable from Eqn. 3.4. The underlying grid must be able fine enough to resolve features on this length scale. Consequently, the width of the smallest dendrite tips that can be resolved is several times larger than $\bar{\epsilon}$, which is already several times larger than the width of a single grid cell.

Moreover, the surface tension anisotropy function introduces a damping force that smears out small scale detail. This is a physical force that is independent of the simulation method used. However, it is clear that in typical winter scenes, dendrite arms that are much smaller than those prescribed by the surface tension function are common. Therefore, other factors must be at work that introduce this additional detail. I will describe these additional factors and suggest a method of simulating them in the next chapter.

3.6 Summary

In Chapter 1, I hypothesized that the main visual characteristics of frost and snowflakes are:

- Growth that can vary continuously between the dendritic and sectorial plate regimes,
- Automatic merging of nearby features that grow together,
- Optical translucency, with specularities in sharp regions.

These characteristics were addressed in this chapter using the following techniques:

- A physically-based ice growth model, the *phase field method* that is capable of generating a wide variety of crystal shapes, ranging from dendritic to sectorial plate.

- User controls for the phase field method that allow simple and intuitive manipulation of the simulation.
- A physically-inspired, novel geometric processing step that introduces internal structure to the ice and enhances the visual realism of the final rendered image.
- A banded optimization method and a mapping to graphics hardware that enables interactive simulation of modest-scale ice crystal growth.

In the next chapter, I will combine the phase field method with two additional techniques: diffusion limited aggregation (DLA) and fluid solvers. The combination of these three techniques will produce visual results that none of the techniques could have captured alone.

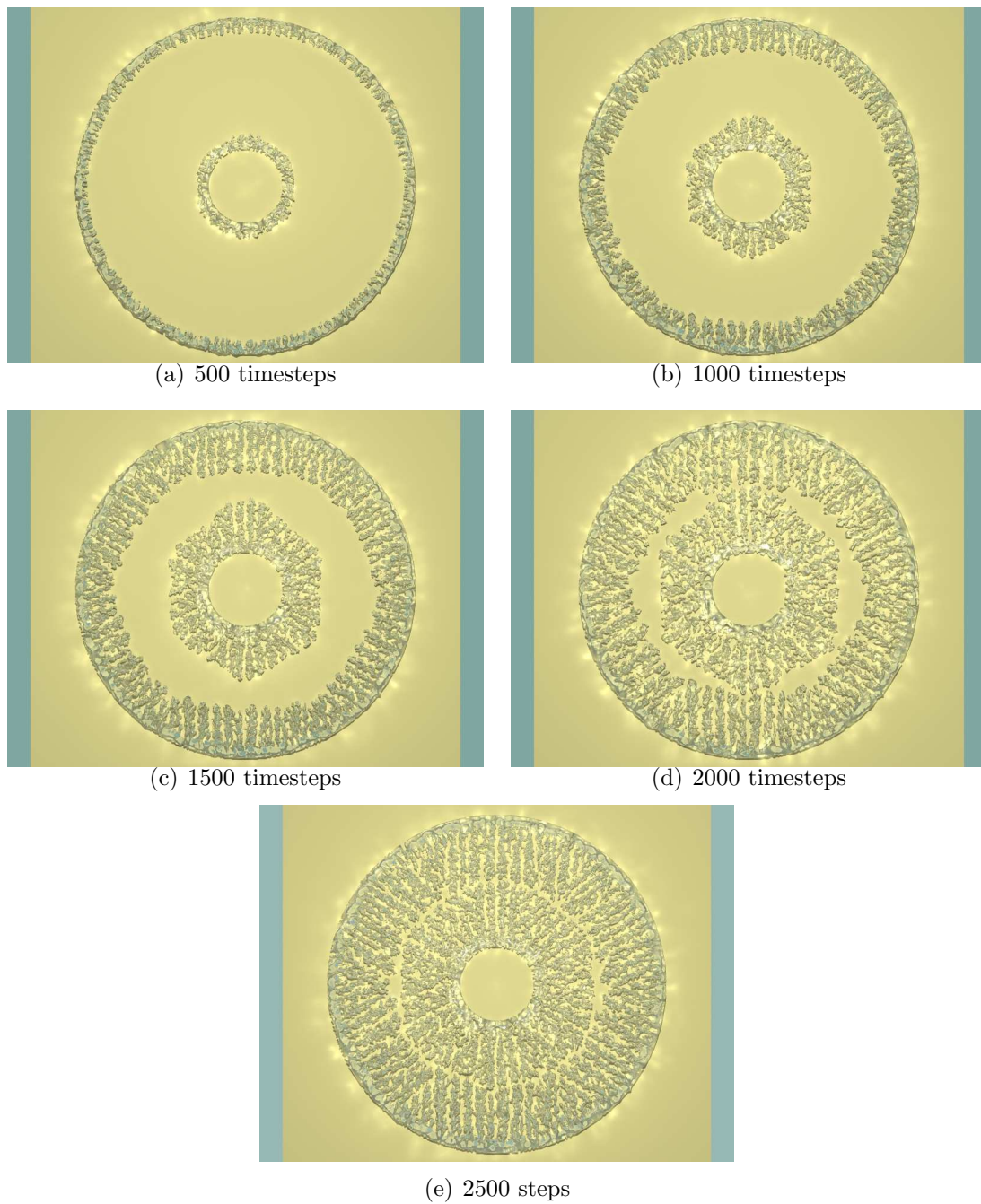


Figure 3.14: **Ice crystals grown in a ring.** The entire simulation took 130 seconds.

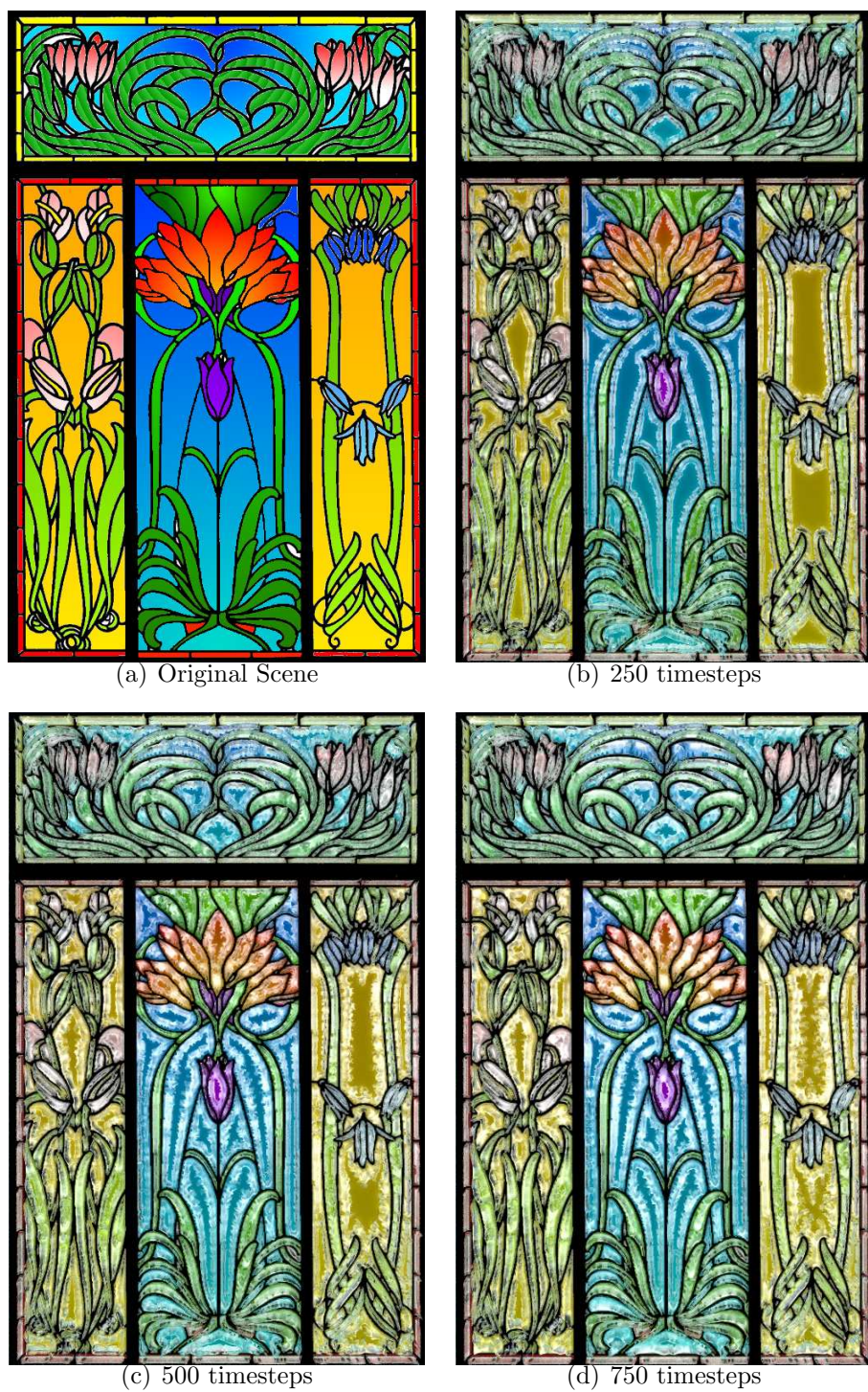
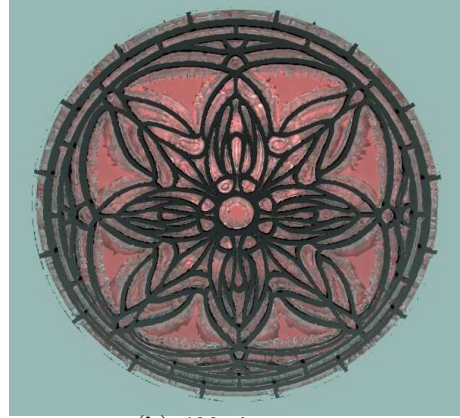


Figure 3.15: **Ice crystals grown on a window panel.** Growth was started along the metal frame of the window. The entire simulation took 50 seconds.



(a) The original scene



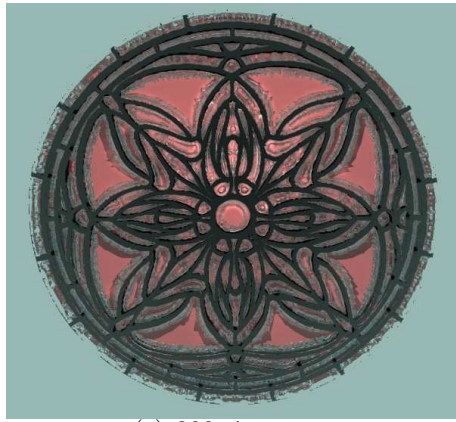
(b) 400 timesteps



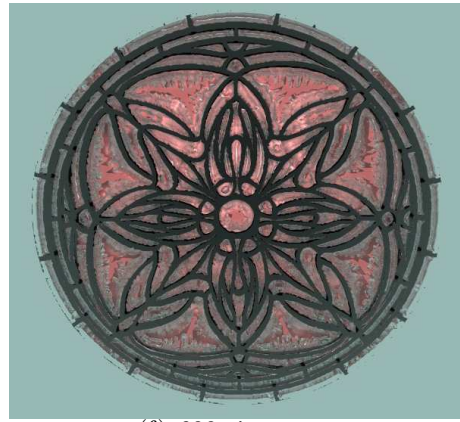
(c) 200 timesteps



(d) 500 timesteps



(e) 300 timesteps



(f) 600 timesteps

Figure 3.16: **Ice growing on a red stained glass window.** The ice crystals form starting from the lead frames. This is the same simulation as the previous figure, but the glass is set to dark red so that the ice formations are more visible. The entire simulation took 34 seconds.



(a) Original Scene



(b) 340 timesteps



(c) 540 timesteps

Figure 3.17: **Ice growing on a stained glass window.** Note how the ice crystals form starting from the lead frames. The entire simulation took 34 seconds.

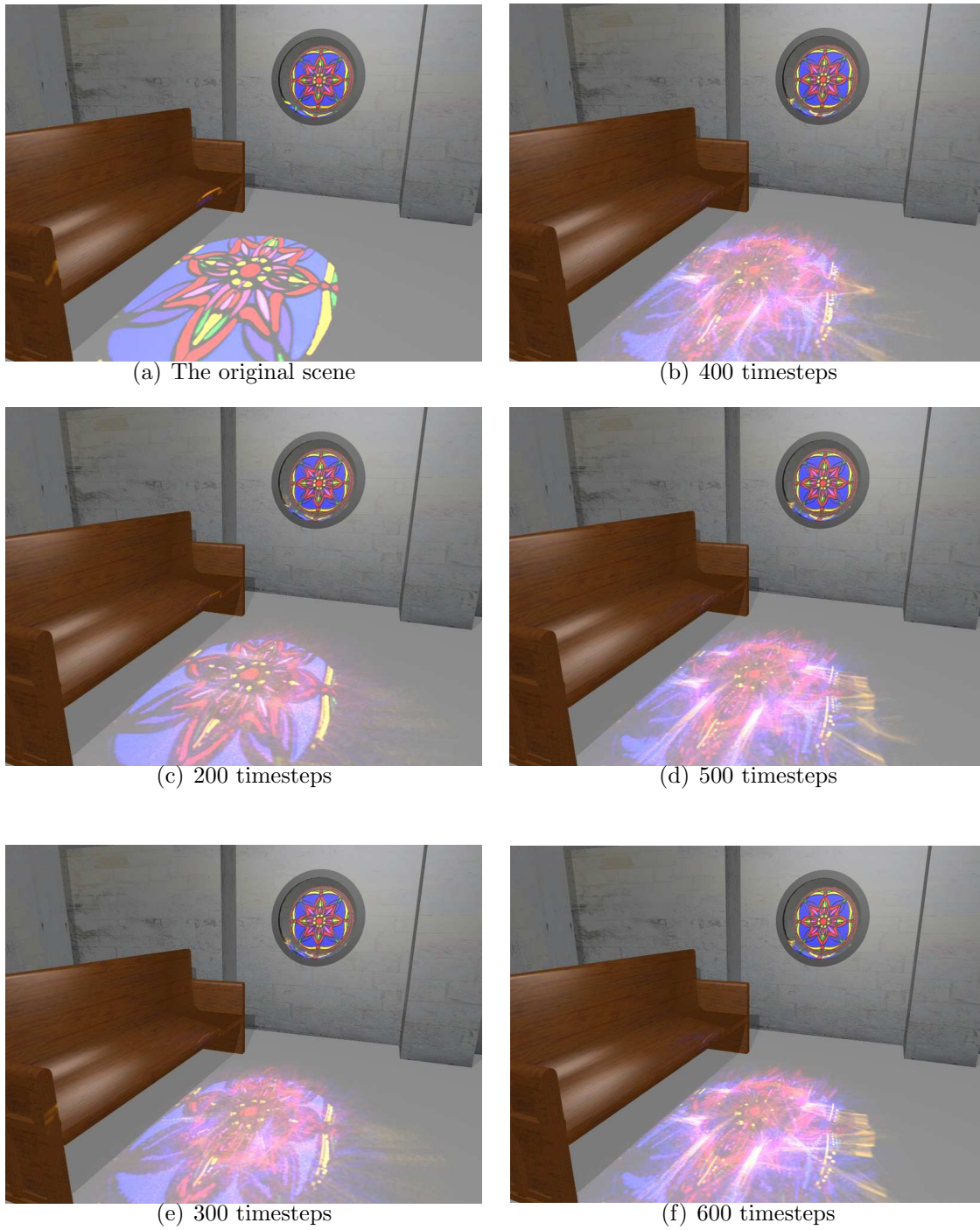


Figure 3.18: **Light refracting through a stained glass window.** Note how the caustic changes as the refractive surface of the ice becomes more complex.

Chapter 4

A Hybrid Algorithm

The phase field method described in the previous chapter successfully simulates the continuum of regimes between sectorial plate and dendritic growth. However, it has trouble handling features that are smaller than a certain threshold. This does not appear to be an issue of merely increasing the grid resolution, because surface tension forces inherently impose a lower limit on the width of dendrites. But, features that are thinner than this lower threshold commonly occur in nature, so some additional physical processes must be at work.

I hypothesize that in typical winter scenes, two simultaneous cases of the Stefan problem are actually occurring. The first is the Stefan problem with surface tension anisotropy from the previous chapter, and second is the *zero surface tension, quasi-steady state* Stefan problem. This second problem corresponds essentially to vapor deposition from the surrounding air. There is an algorithm known as diffusion limited aggregation (DLA) that handles this form of the Stefan problem. I will present a hybrid algorithm that combines phase fields and DLA, thus modeling these two growth cases simultaneously. Since I am now modeling the air surrounding an ice crystal, I will incorporate a flow simulation as well. The resulting growth patterns could not be produced by any of these individual techniques alone.

The overall algorithm design is motivated by the thermodynamics of crystallization, which is commonly broken down into three stages. Phase fields, DLA, and fluid solvers each simulate only one stage of the crystallization process, but by combining all three

techniques, the entire process can be simulated accurately. Additionally, I present a method of simplifying one of the techniques, the phase field method, by posing the problem as an advection-reaction-diffusion equation. An efficient solution method is possible for this simplified formulation that accelerates the phase field method by more than a factor of two. Finally, I will show how the hybrid algorithm can be parameterized to provide intuitive user control.

The original DLA algorithm does not involve any differential equations, so drawing a relation to Stefan problems can be difficult. Instead I will describe an alternate formulation of the same algorithm, known as the *dielectric breakdown model* (DBM). Drawing a relation between DBM and the Stefan problem is straightforward, and from there it can be argued that the same relation holds for DLA.

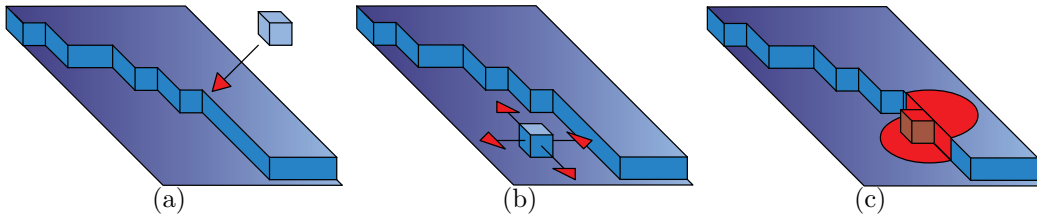


Figure 4.1: A microscopic view of the three stages of freezing. (a) In **chemical diffusion** a water molecule arrives at the crystal (b) During **surface kinetics**, the molecule walks the surface until it finds a *kink site* where it can form 2 bonds (c) In **heat conduction** it forms hydrogen bonds with the crystal and releases heat.

4.1 The Process of Solidification

The hybrid algorithm is motivated by the process of solidification, so I will first summarize the three stages of freezing, and then describe how each individual stage can be simulated. In the next section, I will show how these three simulation techniques can be integrated to account for the entire process.

4.1.1 Three Stages of Freezing

Given a free water molecule and an ice crystal, the process of solidification proceeds in the three stages illustrated in Figure 4:

- First, the water molecule is transported to the surface of the crystal. This is called the *chemical diffusion* stage.
- Second, in order for the water molecule to be considered frozen, it must form two hydrogen bonds with the crystal. The molecule walks along the surface of the crystal until it finds a *kink site* where it can form these bonds. This is called the *surface kinetics* stage.
- Finally, when the molecule forms its hydrogen bonds, it releases a small amount of heat that then diffuses through space. This is called the *heat conduction* stage.

If all three of these processes occur at perfectly balanced rates, then we encounter the *ideal growth* case. However, ideal growth is rarely found in nature, and the process is usually limited by the slowest of the three stages.

When the first stage is slowest, *diffusion limited* growth occurs. An example of this type of growth would be a crystal surrounded by water vapor. If a water molecule happens to collide with the crystal, then it can find a kink site and release heat. However, these collisions are a relatively rare occurrence, so they become the limiting factor.

When the second stage is slowest, *kinetics limited* growth occurs. This type of growth can occur when a crystal is submerged in an undercooled liquid. Recall from chemistry that an undercooled liquid is one whose temperature has slowly been lowered below its freezing temperature. Since the crystal is already surrounded by water molecules, the chemical diffusion rate is no longer a factor. Instead, the limiting factor is the speed at which water molecules can find kink sites on the surface.

When the third stage is slowest, the crystal growth literature also refers to the case as kinetics limited growth. For clarity, we will refer to it here as *heat limited* growth.

If the crystal is surrounded by a fluid flow, then the flow of heat around the crystal is altered. This phenomenon influences the growth of the crystal because the number of kink sites available on a crystal surface is proportional to the magnitude of the local heat gradient. Consequently, for sections of the crystal facing into the flow, heat is pushed back against the crystal, creating a sharp heat gradient that promotes growth. Conversely, for sections facing away from the flow, heat is carried away from the surface, smearing out the gradient and suppressing growth.

For further details on the stages of solidification, the reader is referred to a comprehensive book by Saito (Saito, 1996).

4.1.2 Diffusion Limited Growth

The diffusion limited growth case can be modeled by diffusion limited aggregation (DLA). The basic DLA algorithm was first described by Witten and Sander (Witten and Sander, 1981), and is simple enough to be described informally. Given a discrete 2D grid, a single particle representing the crystal (or ‘aggregate’) is placed in the center. A particle called the ‘walker’ is then placed at a random location along the grid perimeter. The particle walks randomly along adjacent grid cells until it either is adjacent to the crystal or falls off the grid. If it is adjacent to the crystal, it sticks and becomes part of the crystal. A new walker is then inserted at the perimeter and the random walk is repeated. The process repeats until the aggregate achieves the size the user desires. If we think of the aggregate as an ice crystal and the walker as a particle of water, then the correspondence to the diffusion limited case is straightforward.

The DLA (Witten and Sander, 1981) algorithm is referred to as an ‘on-lattice’ algorithm because it takes place on a 2D grid. However, on-lattice algorithms are susceptible to grid anisotropy artifacts. As shown in Figure 4.2(a), as the aggregate grows larger, four distinct arms emerge. These arms have no physical justification, and are purely an artifact of the grid representation. ‘Off-lattice’ algorithms have been developed (Meakin, 1983) that do not suffer from this artifact, but they can be more expensive to compute. I use on-lattice DLA because it simplifies the integration with

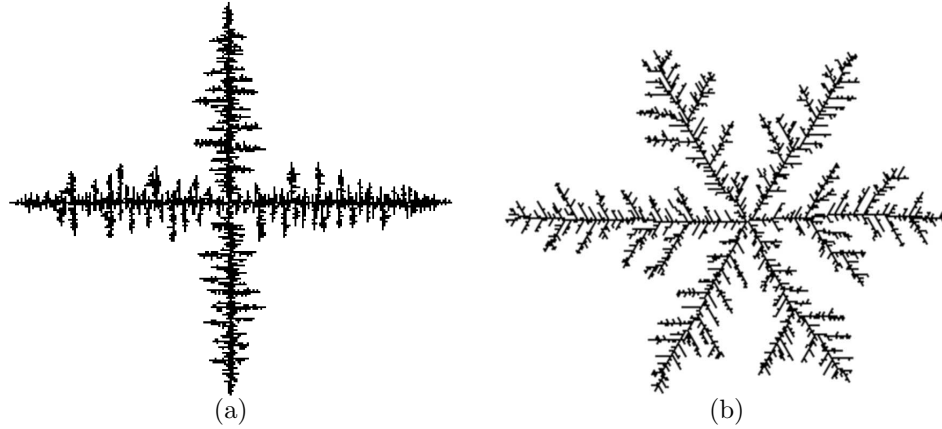


Figure 4.2: Grid anisotropy in diffusion limited aggregation. (a) The four arms of a square grid are non-physical. (b) The six arms of a hexagonal grid mirror the structure of H_2O . For clarity, anisotropy has been exaggerated by setting the value of n in Sec. 4.3.4 to 20.

the phase field methods and the fluid solver, which also take place on grids.

However, this selection means that the simulation will suffer from grid anisotropy. Fortunately, it is possible to make the artifacts correspond to the characteristics of water. By simulating on a hexagonal grid instead of a square grid, we can obtain the 6 distinct arms of a snowflake (Figure 4.2(b)). This resemblance is no coincidence, because the 2 hydrogen bonds necessary for ice formation induces a hexagonal lattice. By simulating on a hexagonal grid, I am mirroring this aspect of ice.

4.1.3 Kinetics Limited Growth

The phase field model of solidification (Kobayashi, 1993) simulates precisely the kinetics limited case: growth of a crystal in an undercooled melt.

This situation may seem rare, but in fact it frequently occurs. In most natural settings, as water reaches its freezing temperature, the molecules already located near a crystal will freeze virtually instantly. However, it will take some time for the ice front to expand and engulf all the water molecules. During this time, the unfrozen molecules will cool further, becoming undercooled.

As described in the previous chapter, the phase field equations are a pair of coupled partial differential equations (PDEs):

$$\begin{aligned} \tau \frac{\partial p}{\partial t} = & \nabla \cdot (\varepsilon(\theta)^2 \nabla p) - \frac{\partial}{\partial x} \left(\varepsilon(\theta) \frac{\partial \varepsilon(\theta)}{\partial \theta} \frac{\partial p}{\partial y} \right) \\ & + \frac{\partial}{\partial y} \left(\varepsilon(\theta) \frac{\partial \varepsilon(\theta)}{\partial \theta} \frac{\partial p}{\partial x} \right) + p(1-p) \left(p - \frac{1}{2} + m(T) \right) \end{aligned} \quad (4.1)$$

$$\frac{\partial T}{\partial t} = \nabla^2 T + K \frac{\partial p}{\partial t} \quad (4.2)$$

where:

$$\varepsilon(\theta) = \bar{\varepsilon}(1 + \delta \cos(j(\theta_0 - \theta))) \quad (4.3)$$

$$m(T) = \frac{\alpha}{\pi} \arctan(\gamma(T_e - T)) \quad (4.4)$$

To review from Chapter 3, the phase field model simulates solidification by tracking two quantities over a 2D grid: temperature, T , and phase, p . While the model generalizes to three dimensions, the full 3D case is not as common in nature, so I will not address it here. The variable T tracks the amount of heat within the grid cell. The variable p tracks the phase of the grid cell, and is defined over the continuous range $[0, 1]$. The value 0 represents water, and 1 represents ice. Phase is usually thought of as a binary quantity, so this continuum of phase values can be counterintuitive. A continuum of states that is crucial to the solidification process exists on the microscopic level, but computing their values directly would result in an intractably stiff set of equations. Phase fields alleviate some of the numerical problems by magnifying the continuum, such that the stiffness is resolvable on the simulation grid. The quantities $\frac{\partial p}{\partial t}$ and $\frac{\partial T}{\partial t}$ are computed by replacing the derivatives with finite differences, and the result is then used to step the simulation using forward Euler integration. Because the equations are still quite stiff, the timestep is limited to 0.0002. I will present a simplification that allows a larger timestep in Section 4.4.

4.1.4 Heat Limited Growth

As described by Anderson (Anderson et al., 2000), the flow of heat around a crystal can significantly influence its final shape. I will show how to produce the same visual characteristics using a Stam-style fluid solver (Stam, 1999b; Fedkiw et al., 2001). Such simulators are commonly available and provides a simple, practical alternative for modeling heat limited growth.

4.2 Relation to the Stefan Problem

Drawing a direct relationship between DLA and the Stefan problem can be difficult, because the Stefan problem is inherently a differential formulation, and DLA does not involve any differential equations. Describing a high-level relation between the two is straightforward however, and the similarity between the two is a commonly acknowledged fact in physics (Sander, 2000).

Rather than give a loose description of the relationship here, I appeal to an alternate formulation of DLA, the *dielectric breakdown model* (DBM) which does involve differential equations. The relationship between DBM and the Stefan problem is straightforward, and can be described in more rigorous terms than the casual relation usually drawn with DLA. While I am not aware of a direct proof of equivalence between DLA and DBM, a wide range of data suggests that this is the case, and it is widely believed that they are in fact equivalent (Mandelbrot and Evertsz, 1990). Therefore, reducing DBM to a Stefan problem is equivalent to performing a similar reduction on DLA.

4.2.1 The Dielectric Breakdown Model

DBM was first described by Niemeyer et al. (Niemeyer et al., 1984) to simulate the branching patterns that occur in electric discharge. While the model can be applied to many natural phenomena, I will describe it intuitively in terms of electrical discharge. The simulation proceeds in three steps:

1. Calculate the electric potential ϕ on a regular grid according to some boundary condition.
2. Select a grid cell as a ‘growth site’ according to ϕ .
3. Add the growth site to the boundary condition.

One application of these three steps is considered a single iteration of DBM. The algorithm is iterated until the desired growth structure, or *aggregate*, is obtained.

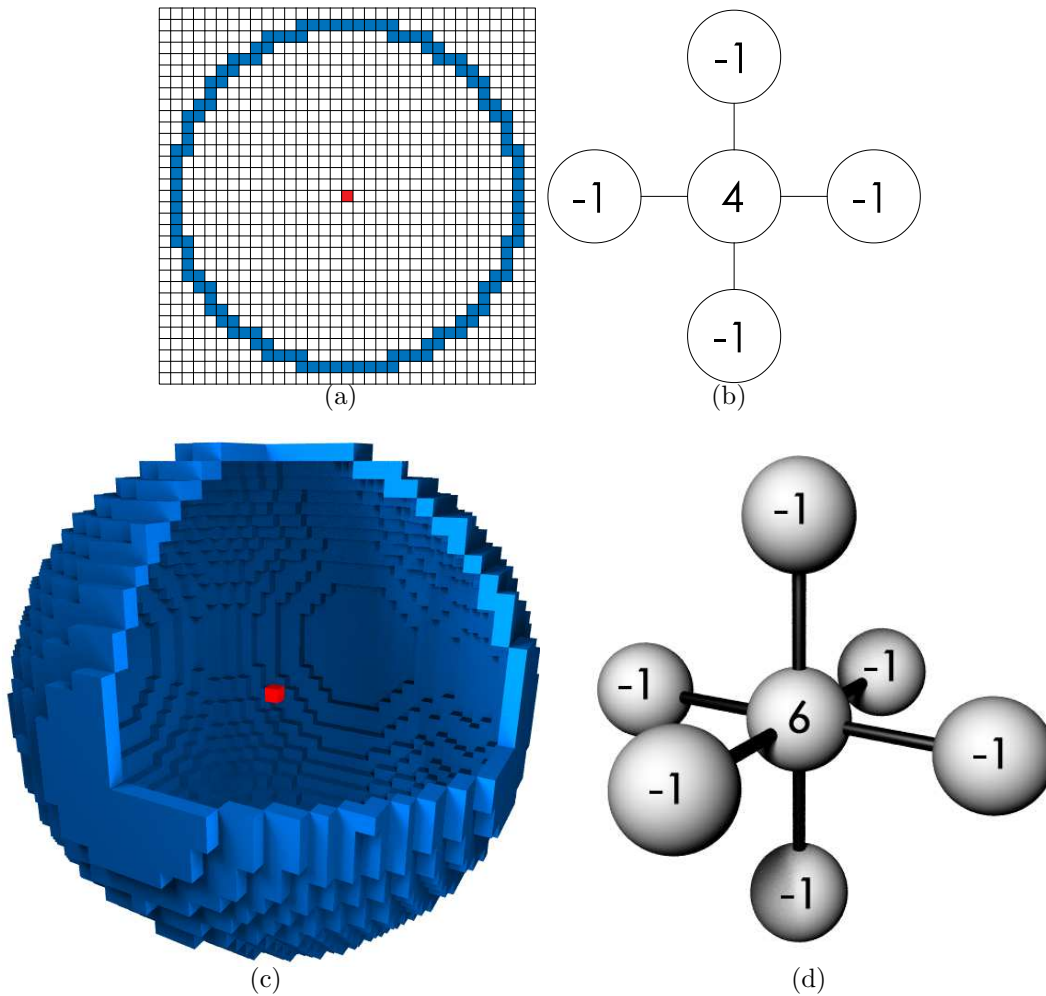


Figure 4.3: (a) Initial conditions for 2D DBM. Red: $\phi = 0$, Blue: $\phi = 1$ (b) 2D Laplace stencil (c) Initial conditions for 3D DBM (Octant cut away for clarity). (d) 3D Laplace stencil

The 2D initial boundary conditions described in (Niemeyer et al., 1984) are shown in Figure 4.3(a). The red cells represent a boundary condition of $\phi = 0$, and the blue cells are $\phi = 1$. Intuitively, $\phi = 0$ corresponds to a region of negative charge, and $\phi = 1$ a region of positive charge. The potentials ϕ in the neutral white cells are obtained by solving the Laplace equation,

$$\nabla^2 \phi = 0, \quad (4.5)$$

according to these boundary conditions. In 2D, the Laplace equation can be solved by constraining the values of the grid cells according to the 5 point Laplacian stencil (Figure 4.3(b)). These constraints produce a linear system that can then be solved with an efficient solver such as conjugate gradient (Shewchuk, 1994). For more information on this standard problem, consult any number of applied linear algebra textbooks (Demmel, 1997).

Once the potential ϕ is known, a growth site must be selected. All grid cells that are adjacent to negative charge are considered candidate growth sites. The growth site is then selected randomly, weighted according to the local potential at each candidate site. The weighted probability function is given in Eqn. 4.6,

$$p_i = \frac{(\phi_i)^\eta}{\sum_{j=1}^n (\phi_j)^\eta} \quad (4.6)$$

where i is the index of some candidate growth site, n is the total number of candidate growth sites, ϕ_i is the potential at site i , and p_i is the probability of selection for site i . Once the site has been selected, it is set to $\phi = 0$, and treated as a boundary condition in subsequent iterations. The algorithm proceeds until the desired growth structure is obtained. Three-dimensional growth can be obtained by instead solving the 7 point Laplacian stencil (Figure 4.3(d)) over a 3D grid, with an initial enclosing sphere instead of a circle (Figure 4.3(c)). The initial boundary condition in Fig. 4.3 is arbitrary, and could be set to other configurations to produce different discharge patterns.

The η term in Eqn. 4.6 is a user parameter that controls the dimension of the growth structure. At $\eta = 0$, a fully 2D growth structure known as an *Eden cluster* is produced (Eden, 1961), and at $\eta = 4$, a 1D line is obtained (Hastings, 2001). Therefore, by tuning η between 0 and 4, the entire spectrum of structures between 1 and 2 dimensions can be obtained. Similarly, in three dimensions, the spectrum between 1D and 3D can be obtained by tuning η . In both 2D and 3D, if η is set to 1, aggregates with fractal dimensions identical to DLA are obtained.

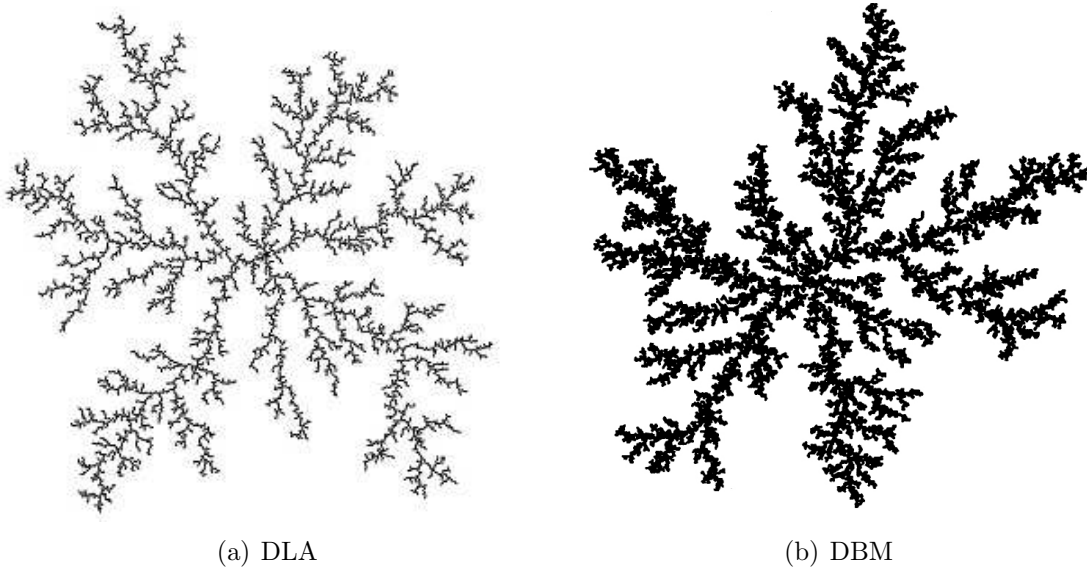


Figure 4.4: Comparison between DBM and DLA: For $\eta = 1$, the fractal dimension of the two aggregates are the same, $D \approx 1.71$.

4.2.2 DBM as a Stefan Problem

While DBM was originally formulated in terms of electric discharge, it can also be viewed as a model of solidification. If we replace the electric potential ϕ with a heat field T , Eqn. 4.5 becomes the quasi-steady state heat equation (Eqn. 1.5). Therefore, solving for the electrostatic potential corresponds directly to solving for the quasi-steady state heat field. DLA can then be viewed as a Monte Carlo solution technique for the same quantity, as it is commonly known that random walks reduce to the heat equation

(Haji-Sheikh, 1988).

This establishes the correspondence between the first equation of the Stefan problem, DBM, and by extension, DLA. The question is now how the growth site selection step of DBM corresponds to the second equation in the Stefan problem (Eqn. 1.2):

$$\frac{\partial \Gamma}{\partial t} \cdot \mathbf{n} = D \frac{\partial T}{\partial \mathbf{n}}.$$

In step 2 of DBM, we select a growth site according to ϕ . In terms of heat, this is equivalent to selecting a growth site according to T . This seems like a different growth criteria than Eqn. 1.2, where the growth rate is proportional to $\frac{\partial T}{\partial \mathbf{n}}$, not T . However, recall that the boundary of the aggregate in DBM is set to $\phi = 0$. Let us denote $\phi_{\text{candidate}}$ as the potential at some candidate site, and $\phi_{\text{aggregate}}$ as the potential at its adjacent aggregate site, and Δx as the distance between the two sites. If we then calculate $\frac{\partial \phi}{\partial \mathbf{n}}$ at the candidate site using finite differences, we obtain:

$$\frac{\phi_{\text{candidate}} - \phi_{\text{aggregate}}}{\Delta x} = \frac{\phi_{\text{candidate}} - 0}{\Delta x} = \frac{\phi_{\text{candidate}}}{\Delta x} \quad (4.7)$$

Since the growth site is selected *proportional* to ϕ , we can set the constant Δx to any arbitrary value. If we set $\Delta x = 1$, we obtain $\frac{\partial \phi}{\partial \mathbf{n}} \approx \phi_{\text{candidate}}$. In other words, due to the $\phi = 0$ boundary condition, the potential at each candidate site is also a first order approximation of the derivative in the normal direction. Therefore, due to the way the boundary conditions of DBM are formulated, selecting growth sites based on ϕ is equivalent to selecting sites based on $\frac{\partial \phi}{\partial \mathbf{n}}$.

The growth site selection process of DBM can then be viewed as a Monte Carlo solution method for Eqn. 1.2. Since sites with large derivatives are selected more often, they develop faster and have greater ‘velocity’ than regions with small derivatives. This is precisely the relation that Eqn. 1.2 describes. DLA can be thought of in an equivalent manner, except that in this case, solving the heat equation and selecting a growth site has been folded into the same Monte Carlo step. Statistically, more particles will walk into regions of high heat, so these regions will receive more particles and grow with a

higher ‘velocity’. Again, this is precisely the relation described by Eqn. 1.2.

4.3 A Hybrid Algorithm for Ice Growth

In each of the growth types described in section 4.1, a simplifying assumption is made. Diffusion limited growth assumes the presence of water vapor, and the absence of liquid water and fluid flow. Kinetics limited growth assumes the presence of liquid water, and the absence of vapor and fluid flow. Heat limited growth assumes the presence of liquid and fluid flow, but the absence of vapor. These simplifications are apparent in the results from each algorithm. DLA forms a branching pattern that can look more like fungus than ice (Figure 4.11(a)), and phase field methods produce branches that look too smooth and thick (Figure 4.11(b)). Adding fluids to either alone do not alleviate these problems.

It seems that an environment containing all three factors (vapor, liquid, and fluid flow) would be the most common case. If ice is forming on a window, there most likely exists water vapor in the air, moisture on the window, and at least a small amount of wind. To properly simulate ice growth, we should account for all of these factors.

I have developed a novel, hybrid algorithm that takes into account all three factors by coupling the simulation techniques for each of the three growth types. I will present the algorithm in three parts: the coupling of phase field methods and DLA, then phase fields and fluid flow, and finally DLA and fluid flow.

4.3.1 Phase Fields and DLA

Here I choose to use DLA instead of the DBM algorithm from the previous section because it is both more computationally tractable and provides a more natural correspondence to the physical situation at hand. The random walkers from DLA map intuitively to actual ice particles undergoing Brownian motion in the neighborhood of the crystal. This correspondence also becomes important later when integrating DLA with fluids. While in principle it is possible to instead apply DBM, it requires that

the Laplace equation be explicitly solved every time a particle is to be added to the simulation. It is possible that instead of the Laplace solution, I could use the heat field from the phase field simulation as an alternate solution. However, this also means the heat field would need to be iterated after the addition of every particle. In addition to adding considerable computational expense to the simulation, this would also introduce a timescale consideration to the simulation that DLA could previously ignore.

Three new steps are necessary to integrate phase field methods with DLA.

- Placement of the walker onto the p (phase) field;
- Release of heat when a walker sticks;
- Introduction of a humidity term.

In the original DLA algorithm, the crystal can only grow when a walker sticks to the crystal. However, in our hybrid setting, the phase field simulation may have also altered the position of the crystal. So, I perform the random walks on the grid for the p variable in the phase field simulation. If the walker is adjacent to a cell with $p > 0.5$, then the particle sticks, and I set the value of that cell to $p = 1$.

When a walker sticks, it forms hydrogen bonds with the crystal, releasing a small amount of heat. The freezing walker will release less heat than if the liquid has frozen, because walker itself is already frozen, and the bonds will only form along the seam between itself and the crystal. We must modify Equation 4.2 to account for this heat release:

$$\frac{\partial T}{\partial t} = \nabla^2 T + K \left(\frac{\partial p}{\partial t} \right)_{PF} + L \left(\frac{\partial p}{\partial t} \right)_{DLA} \quad (4.8)$$

where $\left(\frac{\partial p}{\partial t} \right)_{PF}$ is the rate of change in p due to the phase field simulation, and $\left(\frac{\partial p}{\partial t} \right)_{DLA}$ the rate of change due to DLA. I use a setting of $L = \frac{K}{6}$ because bonds have only formed along one face of the hexagonal grid cell.

Lastly, I introduce a humidity term, H , because the original DLA simulation does not contain any notion of time. At every timestep, H walkers are released into the

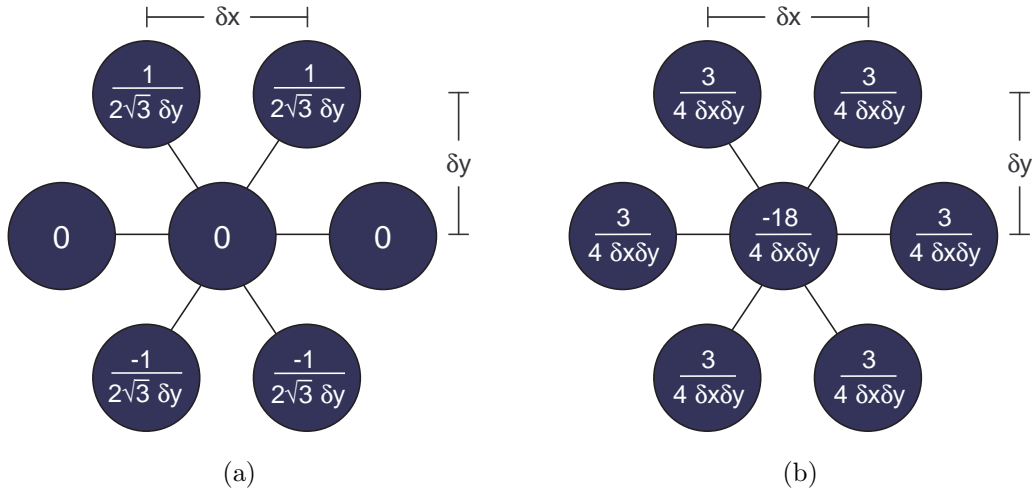


Figure 4.5: Finite difference stencils for a hexagonal grid. (a) y derivative (b) Laplacian. Stencil for x derivative remains the same.

simulation domain. Increasing H corresponds to increasing the humidity of the environment. Note that H represents the *total* number of walkers released, not just those that stick to the crystal. The correct setting for H is more of an aesthetic question than a physical question, and is discussed further in 4.3.4.

If DLA is performed on a hexagonal grid, then it is possible to simulate phase fields on a square grid, and interpolate between the two representations. However, this approach will introduce smoothing artifacts into the simulation. This problem can be overcome by running phase fields on a hexagonal grid as well. The only modification necessary is to switch from square finite difference stencils to hexagonal stencils. The weights on the hexagonal stencil can be computed by taking the Taylor expansion and solving using the method of undetermined coefficients (Atkinson, 1989). The stencils are shown in Figure 4.5.

Integrating phase field methods and DLA may seem incorrect at first, because if liquid water is present, then kinetics limited growth should dominate. But, if we observe that kinetics limited growth and diffusion limited growth can co-exist at different scales, this is no longer true. Because the vapor particles are much larger than the liquid

molecules, the freezing vapor front will expand much faster than the freezing liquid front. Once the vapor has filled the domain with branches, the liquid will take over and freeze everything into a solid plate.

4.3.2 Phase Fields and Fluid Flow

Anderson, et al. (Anderson et al., 2000) derived a model that couples the phase field equations and the Navier-Stokes equations. Rather than using this more complex formulation, I have found the major features of solidification in a flow can be captured by simply advecting the heat field with the “Stable Fluid” solver described in (Stam, 1999b).

Anderson, et al. (Anderson et al., 2000) does not present any simulation results visually, so I will instead compare our results to those of Al-Rawahi and Tryggvason (Al-Rawahi and Tryggvason, 2002). Since this paper does not use a phase field model, exactly matching simulation parameters for comparison is difficult. But, the paper observes the following features of growth in a flow:

- Fast growth in regions facing upstream (into flow)
- Stunted growth in regions facing downstream (away from flow)
- Asymmetric growth in regions perpendicular to the flow.

I can reproduce all of these features using the coupling of phase fields methods and a “Stable Fluid” solver.

I treat the crystal as an internal obstacle in the fluid solver. After each pair of phase field and DLA steps, I set any grid cell with $p > 0.5$ to an obstacle in the fluid domain. I then set the velocities in the obstacle interior to zero, and along the obstacle boundary to the no-slip condition. The velocity field u is then advanced as described by Stam (Stam, 1999b). For a lucid description of implementing internal obstacles and various boundary conditions, please refer to Griebel et al. (Griebel et al., 1997).

The resultant velocity field u can be used to advance a density field. In this case, the density field is the temperature field T from the phase field simulation. Note that if the fluid solver implements a diffusion constant for the density field, it must be set to zero. Observe that the PDE for a temperature field T (Eqn. 4.2) and the PDE for a moving density field ρ (Eqn. 4.9) both contain the diffusion operator ∇^2 .

$$\frac{\partial \rho}{\partial t} = -(u \cdot \nabla)\rho + \kappa \nabla^2 \rho \quad (4.9)$$

If the diffusion constant κ in Eqn. 4.9 is nonzero, then the temperature field T will incorrectly be diffused twice; once by Eqn. 4.2 and once by Eqn. 4.9. If κ is set to zero in Eqn. 4.9, the correct result is obtained.

In the examples of (Al-Rawahi and Tryggvason, 2002), the crystals are grown from a dot of ice in the center. The left wall is set to an inflow condition, and the other walls are set to an outflow condition. The equivalent of the j parameter from the phase field equations is set to 4, meaning that four axis-aligned dendrite arms are desired. The arms are positioned so that one is growing upstream, one downstream, and two perpendicular to the flow. The results of their simulation are shown in Figure 4.6(a), and the three growth features mentioned earlier are clearly visible. The results of my simulation, with similar settings, are shown in Figure 4.6(b). Although the features do not align exactly, the method clearly produces the same growth features.

4.3.3 DLA and Fluid Flow

The integration of DLA and simplified fluid flow has been studied by the physics community in the past. In particular, Nagatani and Sagués (Nagatani and Sagués, 1991) models the fluid as a uniform velocity field, and Toussaint et al. (Toussaint et al., 1992) use Lattice Boltzmann-type cellular automata. However, I require no such simplification. Since the DLA and phase field simulations share the p field, integrating phase field methods and with the fluid solver automatically integrates DLA with the full set of Navier-Stokes equations.

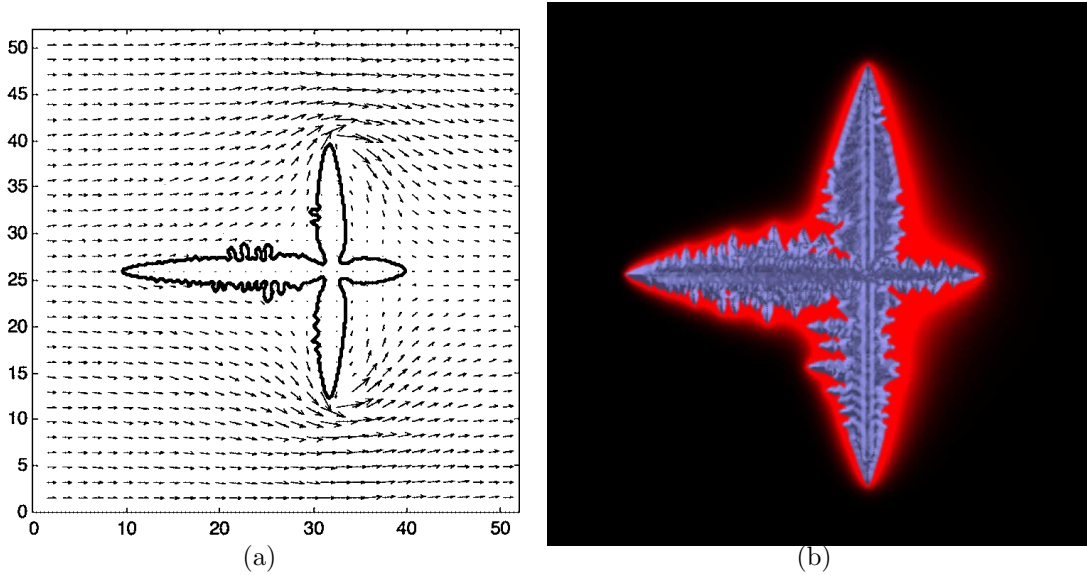


Figure 4.6: A 4-armed dendrite growing in a flow. Left wall is set to inflow, and other walls are set to outflow. (a) Results from (Al-Rawahi and Tryggvason, 2002) (b) Results from my method.

Additionally, the fluid velocities should influence the walker. When the walker is stepped, a random direction is chosen as before, but the fluid velocity of the current grid cell is also added to that direction. It seems as though the velocity should be multiplied by a timestep, but it is unclear what this timestep should be because DLA lacks any notion of time. Using the timestep of the overall simulation dt is not entirely correct, because the timespan simulated by the particle is then $dt * (\#of\ steps)$, not just dt . However, scaling by this value produced acceptable results, so it was used in my current implementation.

4.3.4 User Control

I suggested in the previous chapter a seed crystal map and melting temperature map as controls for the phase field simulation. The hybrid algorithm can be effectively controlled using these same parameters, as well as an additional ‘tunable morphology’ control, and the humidity term H from section 4.3.1.

The melting temperature map is a user-specified field whose values range over $[0,1]$.

A value of 1 indicates fully promoted growth, 0 indicates fully suppressed growth, and intermediate values represent varying degrees of desired growth. The melting temperature map can double as a semantically identical ‘sticking probability’ map for DLA. When the walker is adjacent to the crystal, a random number over $[0,1]$ is chosen. If the number is less than a ‘sticking probability’ (Vicsek, 1984), then the walker freezes; otherwise, it continues walking. In basic DLA, the ‘sticking probability’ is essentially set to 1 everywhere.

Additionally, the user may alternately desire different growth types from the crystal morphology, from the random, lichen-like growth in Figure 3.2.3(c), to the regular, snowflake-like growth in Figure 4.2(b). These effects can be controlled using the multiple-hit averaging technique of Nittman and Stanley (Nittmann and Stanley, 1987). In order for a grid cell to freeze, n walkers must stick at that cell. In basic DLA, $n = 1$, but by increasing n , increasingly regular growth patterns are obtained.

The humidity control described in 4.3.1 allows a way of controlling how ‘branchy’ or ‘frosty’ the results appear. At very high humidity, we obtain the extreme branchiness of the DLA algorithm, and at very low humidity, the smooth features of the phase field algorithm dominate. Usually we would like the leading edge of the ice front to be very branchy, with a rapidly thickening front trailing not too far behind.

4.4 Faster Phase Field Methods

The performance of the hybrid algorithm is limited by the timestep restriction of the phase field methods, so a method for increasing the timestep is desired. I reported in the previous chapter that midpoint and RK4 are unable to increase the timestep enough to justify their expense, so techniques other than linear multistep methods are required.

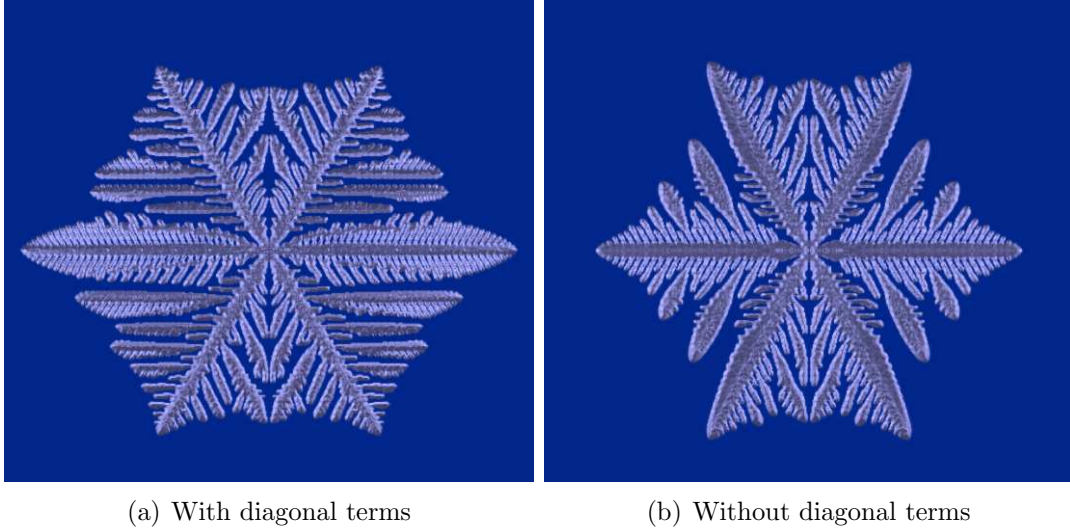


Figure 4.7: Results of a phase field simulation with and without the diagonal terms of the diffusion tensor. While the side branching is noticeably smoother, the overall features remain intact.

Recall the PDE for phase:

$$\begin{aligned} \tau \frac{\partial p}{\partial t} = & \nabla \cdot (\varepsilon(\theta)^2 \nabla p) - \frac{\partial}{\partial x} \left(\varepsilon(\theta) \frac{\partial \varepsilon(\theta)}{\partial \theta} \frac{\partial p}{\partial y} \right) \\ & + \frac{\partial}{\partial y} \left(\varepsilon(\theta) \frac{\partial \varepsilon(\theta)}{\partial \theta} \frac{\partial p}{\partial x} \right) + p(1-p) \left(p - \frac{1}{2} + m(T) \right) \end{aligned}$$

I first observe that the partial derivative terms can be thought of as the sum of the entries in a variable coefficient Hessian matrix. Equations 4.1 and 4.2 resemble the reaction-diffusion equations described in (Turk, 1991; Witkin and Kass, 1991). However, only the diagonal entries of the Hessian are used in (Witkin and Kass, 1991). To see if such a simplification can be applied here, I ran experiments with a forward Euler implementation, omitting the $-\frac{\partial}{\partial x} \left(\varepsilon \frac{\partial \varepsilon}{\partial \theta} \frac{\partial p}{\partial y} \right) + \frac{\partial}{\partial y} \left(\varepsilon \frac{\partial \varepsilon}{\partial \theta} \frac{\partial p}{\partial x} \right)$ term. Although the results are noticeably smoother, the branching features remained the same (Fig. 4.7). Informally we can think of this as truncating higher order terms from the non-linear diffusion operator.

A simplified phase PDE can now be written:

$$\tau \frac{\partial p}{\partial t} = \nabla \cdot (\varepsilon(\theta)^2 \nabla p) + p(1-p) \left(p - \frac{1}{2} + m(T) \right)$$

By applying the identity $\nabla \cdot (\alpha^2 \nabla p) = \nabla \alpha^2 \cdot \nabla p + \alpha^2 \nabla^2 p$, this becomes:

$$\tau \frac{\partial p}{\partial t} = \nabla \varepsilon(\theta)^2 \cdot \nabla p + \varepsilon(\theta)^2 \nabla^2 p + p(1-p) \left(p - \frac{1}{2} + m(T) \right). \quad (4.10)$$

This is a *non-linear advection-reaction-diffusion* equation. If we now apply a second order accurate temporal scheme, then we will be able to take larger timesteps. For compactness of notation, I will abbreviate $\varepsilon(\theta)^2$ to α , and denote the value of p at grid coordinate (i, j) and timestep n as $p_{i,j}^n$.

4.4.1 Second Order Accuracy In Time

The *Lax-Wendroff* scheme is applied to the advection term $\nabla \varepsilon(\theta)^2 \cdot \nabla p$. In the x direction, I replace the old scheme:

$$\frac{\partial \alpha}{\partial x} \frac{\partial p}{\partial x} \approx \frac{\alpha_{i-1,j} - \alpha_{i+1,j}}{\Delta x} \frac{p_{i-1,j}^n - p_{i+1,j}^n}{\Delta x}$$

with the Lax-Wendroff scheme:

$$\begin{aligned} \frac{\partial \alpha}{\partial x} \frac{\partial p}{\partial x} \approx & \frac{\alpha_{i-1,j} - \alpha_{i+1,j}}{\Delta x} \frac{p_{i-1,j}^n - p_{i+1,j}^n}{\Delta x} - \\ & \left(\frac{\alpha_{i-1,j} - \alpha_{i+1,j}}{\Delta x} \right)^2 \frac{p_{i-1,j}^n - 2p_{i,j}^n + p_{i+1,j}^n}{(\Delta x)^2} \end{aligned}$$

The equivalent scheme in the y direction is:

$$\begin{aligned} \frac{\partial \alpha}{\partial y} \frac{\partial p}{\partial y} \approx & \frac{\alpha_{i,j-1} - \alpha_{i,j+1}}{\Delta y} \frac{p_{i,j-1}^n - p_{i,j+1}^n}{\Delta y} - \\ & \left(\frac{\alpha_{i,j-1} - \alpha_{i,j+1}}{\Delta y} \right)^2 \frac{p_{i,j-1}^n - 2p_{i,j}^n + p_{i,j+1}^n}{(\Delta y)^2}. \end{aligned}$$

Next, the *Crank-Nicolson* discretization is applied to the diffusion term, $\varepsilon(\theta)^2 \nabla^2 p$.

I replace the old method,

$$\alpha^2 \frac{\partial^2 p}{\partial x^2} \approx \alpha^2 \left(\frac{p_{i-1,j}^n - 2p_{i,j}^n + p_{i+1,j}^n}{(\Delta x)^2} \right),$$

with the Crank-Nicolson scheme,

$$\alpha^2 \frac{\partial^2 p}{\partial x^2} \approx \frac{\alpha^2}{2} \left(\frac{p_{i-1,j}^n - 2p_{i,j}^n + p_{i+1,j}^n}{(\Delta x)^2} + \frac{p_{i-1,j}^{n+1} - 2p_{i,j}^{n+1} + p_{i+1,j}^{n+1}}{(\Delta x)^2} \right).$$

The equivalent discretization in the y direction is

$$\alpha^2 \frac{\partial^2 p}{\partial y^2} \approx \frac{\alpha^2}{2} \left(\frac{p_{i,j-1}^n - 2p_{i,j}^n + p_{i,j+1}^n}{(\Delta y)^2} + \frac{p_{i,j-1}^{n+1} - 2p_{i,j}^{n+1} + p_{i,j+1}^{n+1}}{(\Delta y)^2} \right).$$

Since this discretization is implicit, a sparse linear system must now be solved.

In practice, Red-Black Gauss-Seidel iteration is a viable solution method. More sophisticated non-symmetric solvers could be applied such as Bi-CG or GMRES, but the system converges to working precision in less than 10 iterations, so it is unlikely that these solvers will give drastically better performance. Conjugate gradient cannot be applied because the system is not symmetric, and finding an optimal relaxation value for SOR is difficult because the matrix eigenvalues change every iteration. More information on iterative solution methods for linear systems is available in any number of texts (Demmel, 1997; Saad, 2003; Trefethen and Bau, 1997).

4.4.2 Performance Analysis

Using this second-order method, the timestep can be quadrupled to 0.0008. If the linear system is solved to working precision, then no significant performance gain is observed. However, experiments have shown that solving the system to within 5×10^{-3} , gives results that are visually indistinguishable from the precise solution, and achieves up to a 2.27x speedup. The results are summarized in Table 4.1.

Resolution	Euler	WP	RP	Speedup
128x128	9 sec	7 sec	4 sec	2.25x
256x256	84 sec	79 sec	37 sec	2.27x
512x512	801 sec	871 sec	392 sec	2.04x
1024 x 1024	6864 sec	8509 sec	3443 sec	1.99x

Table 4.1: Phase field performance over different resolutions. Euler timestep is 0.0002, second order timestep is 0.0008. In WP column, the system is solved to working precision (10^{-8}). In RP column, the system is solved to reduced precision (5×10^{-3}). The last column is the speedup of RP over Euler.

4.5 Implementation and Results

One step of the hybrid algorithm is implemented as:

```

for 1:H
    insert walker onto p field
    simulate walker on p field
end
step phase fields
copy p > 0.5 to obstacle field
step fluid velocities
step density/temperature field

```

The phase field simulation and fluid solver required no significant alteration. The DLA simulation was altered to walk on the p field, insert heat into the T field, and account for fluid velocities. The p field was copied into the obstacle field by a high-level class. With C++ implementations of all three algorithms, only about 100 additional lines of code are necessary to implement the hybrid algorithm on a square grid. To simulate on a hexagonal grid, more significant changes are needed, but the size of the code remains about the same. A displacement map was generated from the simulation results by accumulating the $\frac{\partial p}{\partial t}$ values over the lifetime of the simulation and normalizing the values to the $[0, 1]$ range. The results were then rendered in 3DS Max 5.

I ran the simulation at various physical scales: the microscale of a snowflake, the mesoscale of a pint glass, and the macroscale of an automobile windsheild. Due to the fractal nature of ice, our algorithm scales naturally between a wide variety of physical scales.

In the snowflake image (Fig. 4.13), a solid border has been produced, but the intricate veining internal to the border has been produced as well. This is essentially the internal structure that the crease introduction step from the previous chapter was attempting to capture, but DLA offers a more efficient, physically based method of introducing the same detail. The simulation takes considerable more time per timestep than any of the other simulation because it is started from a much smaller seed crystal than any of the simulations, meaning that each DLA particle must walk for longer before sticking or walking off the simulation domain. The humidity setting also exceeds that of any of the other simulations by an order of magnitude, which means the simulation spends proportionally longer performing DLA each timestep.

In Figure 4.9, frost formation on a car is simulated. While the resolution of the simulation is relatively modest, both small and large scale detail are produced because the DLA algorithm produces features that are on the order of a single grid cell. The shape of the forming ice front is also manipulated by controlling the flow profile of the incoming fluid.

Figure	Resolution	H	Timesteps	Sim. Time	Seconds per step
4.13	1024 x 1024	60000	200	2 hrs	36
4.11	256 x 256	Variable	300	4 min 16 sec	0.85
4.8	512 x 512	100	1600	4 min 32 sec	0.17
4.9	1024 x 1024	4000	350	3 min 35 sec	0.61

Table 4.2: Timing results for simulation, excluding rendering time. For aesthetic effect in Figure 4.11, the humidity was started at 300 and increased by 50 after the 75th timestep. The first figure has a much longer running time per step because its humidity setting is more than 10 times larger than any of the other simulations. The simulation therefore spends proportionally more time performing DLA.

Figure 3.17 shows frost formation on a chilled glass. In this case, the fingering effect on the fringe of the solidification front is reproduced faithfully. Far from the front, the ice formed into a solid plate, but due to the non-uniform growth history, the plate is not entirely flat. Instead the bumpy surface of the ice reflects the surrounding environment map, producing a variety of colorful specular effects that increase the realism of the final image.

All of the simulations were run on a 2.66 GHz Xeon processor, with timing results (excluding rendering time) shown in Table 4.2. In Figure 4.11, the inflow fluid velocity along the top edge was set equal to 0 along the left wall and increased quadratically to 3.5 approaching the right wall. In Figure 4.9, the top edge was set to a parabolic inflow of 3.5 in the center and 0 at the ends. The same simulation was used for the hood, side panel, and windshield. For all simulations, δx , δy were set to $\frac{3}{64}$ to keep the timestep fixed.

4.6 Discussions and Limitations

In Figures 4.9-4.13, I show images of simulated ice forming in a snowflake pattern, on a frozen window pane, on a chilled glass, and on a car in a wintery scene. For two of these, the snowflake and chilled glass, I also present photographs for comparison. Validating results of any simulation can be very challenging, and I found this task especially difficult for the window and car scenes, as outdoor environments contains a plethora of factors that can affect the growth of ice pattern in a significant way.

For Figure 4.13, the snowflake scene, the inset photograph shows that the overall shape and distribution of arms has been reproduced. Most notably, the intricate network of veins internal to the border of the snowflake have been produced. DLA alone can produce the same veins, but cannot produce the thickened border. Phase fields from the previous chapter can produce the thick border, but cannot produce the veins without significant intervention. The hybrid algorithm produces these features automatically.

Validating the chilled glass poses a more complex challenge, as chilled glasses frost over almost instantly when removed from a freezer. For comparison purposes in figure 4.12, the initial conditions of the chilled glass simulation were altered slightly so that some growth also occurred along the top edge of the glass. Although a direct comparison is difficult in the absence of more sophisticated rendering, note that the ‘fingering’ of the ice along the leading edge of the frost has been faithfully reproduced. Far from leading edge, the frost in both the photo and the simulation has formed a solid sheet. Small scale fingering is a feature of diffusion limited growth, and the sheet of frost is a kinetics limited phenomena. Neither DLA nor phase fields can produce both features, but the hybrid algorithm produces both.

The current implementation is limited by the 2D treatment of fluid flow, which assumes that the wind velocities are roughly parallel to the simulation domain. To handle the perpendicular case, a full 3D fluid solver is necessary. The algorithm also cannot handle thick features, such as icicles, which will be covered in the next chapter.

In a general sense, I have developed a novel method of texture synthesis. The statement of the phase field equations as a non-linear advection-reaction-diffusion system shows that they represent a more general class of phenomena than pure reaction-diffusion. In addition to the competitive morphogens usually present in a reaction-diffusion system (Witkin and Kass, 1991), the hybrid algorithm adds two complementary morphogens operating at different scales.

In the absence of a fluid flow and with isotropic growth settings, this synthesis method can be considered a *Laplacian growth* algorithm (Niemeyer et al., 1984). With the addition of anisotropy and fluid flow, it becomes a non-Laplacian growth (Roberts and Knackstedt, 1993) algorithm. As such, it has the potential to increase the realism of other Laplacian phenomena, such as the formation of cracks, the formation of lightning, and the growth of trees.

Several issues exist for further refinement. An unconditionally stable algorithm would be ideal for phase field methods, but the non-linear nature of the equations makes the derivation difficult. In particular, the presence of the $\frac{\partial p}{\partial t}$ term in Eqn. 3.1

introduces a differential coupling between the phase and heat equations that is difficult to discretize in an unconditionally stable manner.

For DLA, ideally an arbitrary anisotropy function could be imposed on a square grid, but while some impressive recent work has produced true isotropy on a square grid (Bogoyavlenskiy, 2001), arbitrary anisotropy remains elusive. For a large humidity, DLA can be the slowest component of the simulation, so potentially faster alternative solution methods, such as the dielectric breakdown model (Niemeyer et al., 1984) and Hastings-Levitov conformal mapping (Hastings and Levitov, 1998), are worth investigation.

I have yet to address the rendering issues associated with ice growth. Ice is composed of highly anisotropic mesofacets that exhibit strong spectral dispersion. As such, it seems to inhabit a mesoscale in between the macroscopic features of textures and the microfacet features of BRDFs, making realistic rendering difficult. Further study is needed to capture their sparkling, rainbow features. A visually plausible approximation will be presented in the next chapter.

4.7 Summary

In Chapter 1, I hypothesized that the main visual characteristics of frost and snowflakes are:

- Growth that can vary continuously between the dendritic and sectorial plate regimes,
- Automatic merging of nearby features that grow together,
- Optical translucency, with specularities in sharp regions.

In Chapter 3, I described how to use phase field methods to capture these characteristics. However, while phase fields methods excel at capturing the second characteristic, the merging of features, it can come at the expense of sharp features in the dendritic

growth regime. In this chapter, I described a method of enhancing these sharp features while still maintaining the front tracking strengths of the phase field method. These new sharp features in turn enhance the third visual characteristic, because the small features create more realistic specularities. To summarize, in this chapter, I have presented a hybrid ice formation algorithm with the following features:

- A physically-based approach that is inspired by the thermodynamics of ice formation.
- A novel discrete-continuous method that combines three techniques: diffusion limited aggregation, phase field methods, and stable fluid solvers.
- A faster, simplified formulation of the phase field method.
- A unified parametrization of the simulations that enables simple artistic control of the visual results.

I have demonstrated the flexibility of the algorithm by simulating over arbitrary 3D surfaces of widely varying physical scale. Whereas the previous chapter covered 2D growth on planar surfaces, this chapter presented a 2.5D approach that can take into account particles and flow conditions from an external 3D world. However, the final results remain 2D. In the next chapter, I will address the problem of fully 3D ice formation. The techniques presented in the previous and current chapter do not extend naturally to fully 3D growth, so new techniques will be introduced.

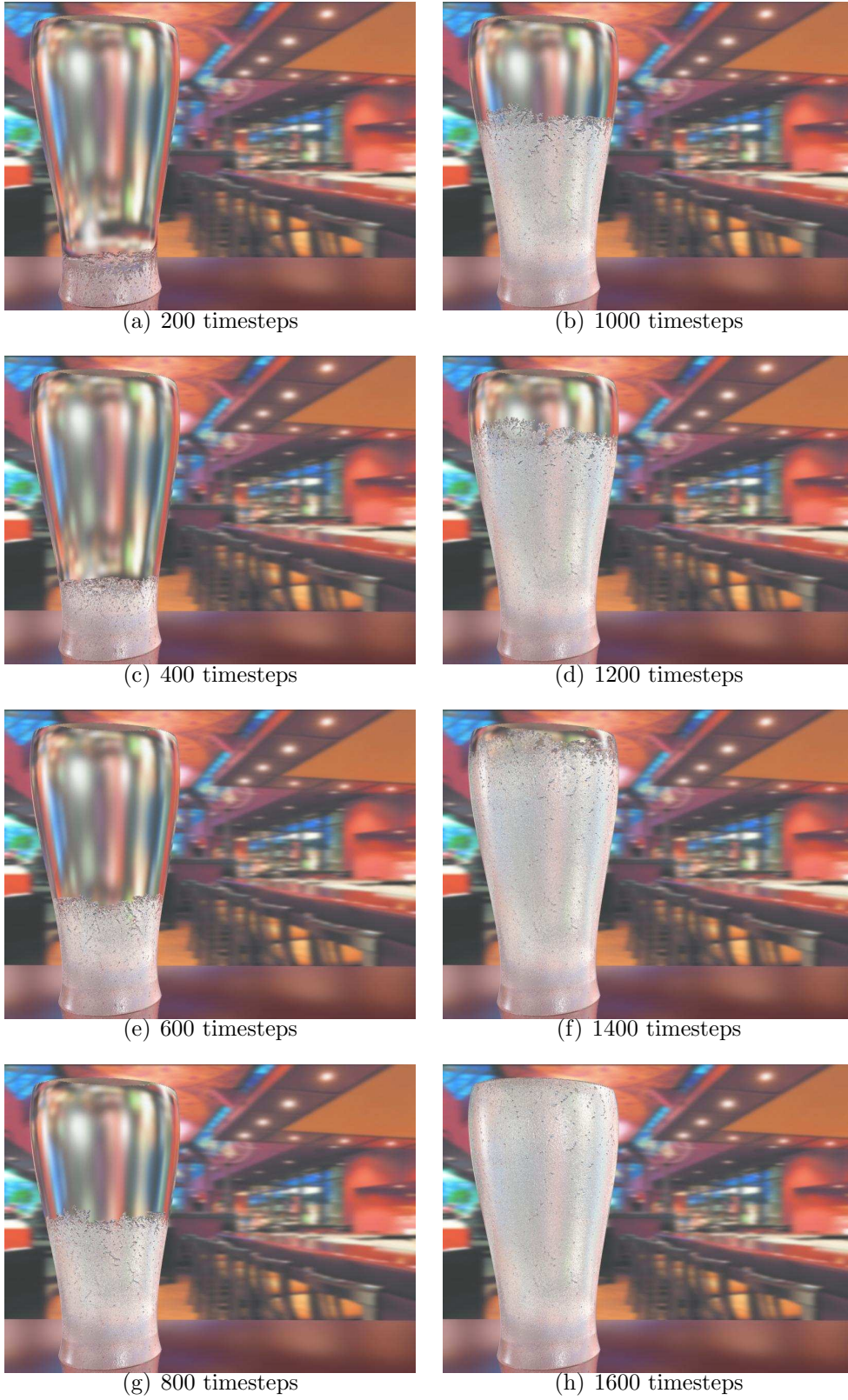


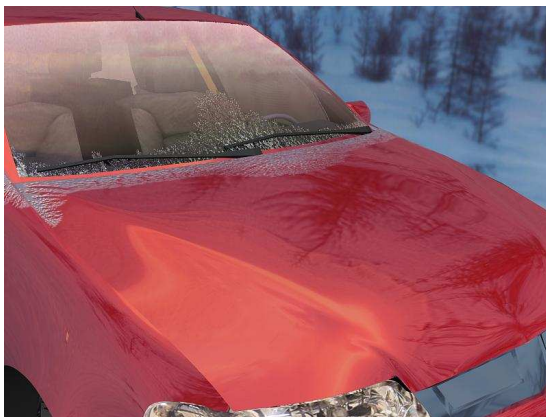
Figure 4.8: Frosty ice forming on a chilled glass.



(a) 1 timesteps



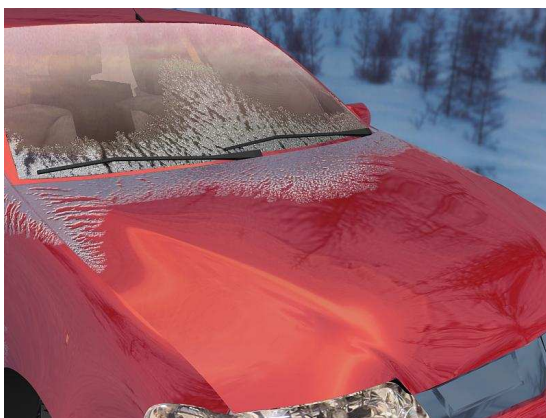
(b) 150 timesteps



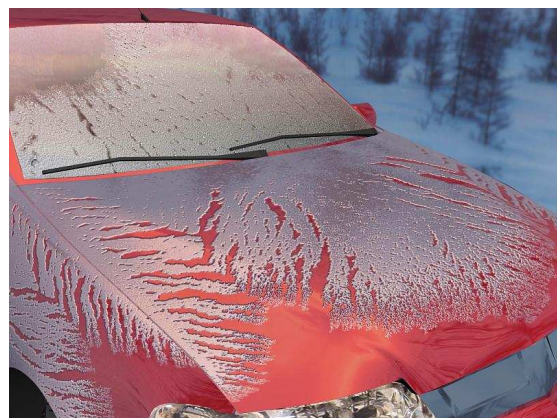
(c) 50 timesteps



(d) 200 timesteps



(e) 100 timesteps



(f) 250 timesteps

Figure 4.9: Ice Accumulated on a car.

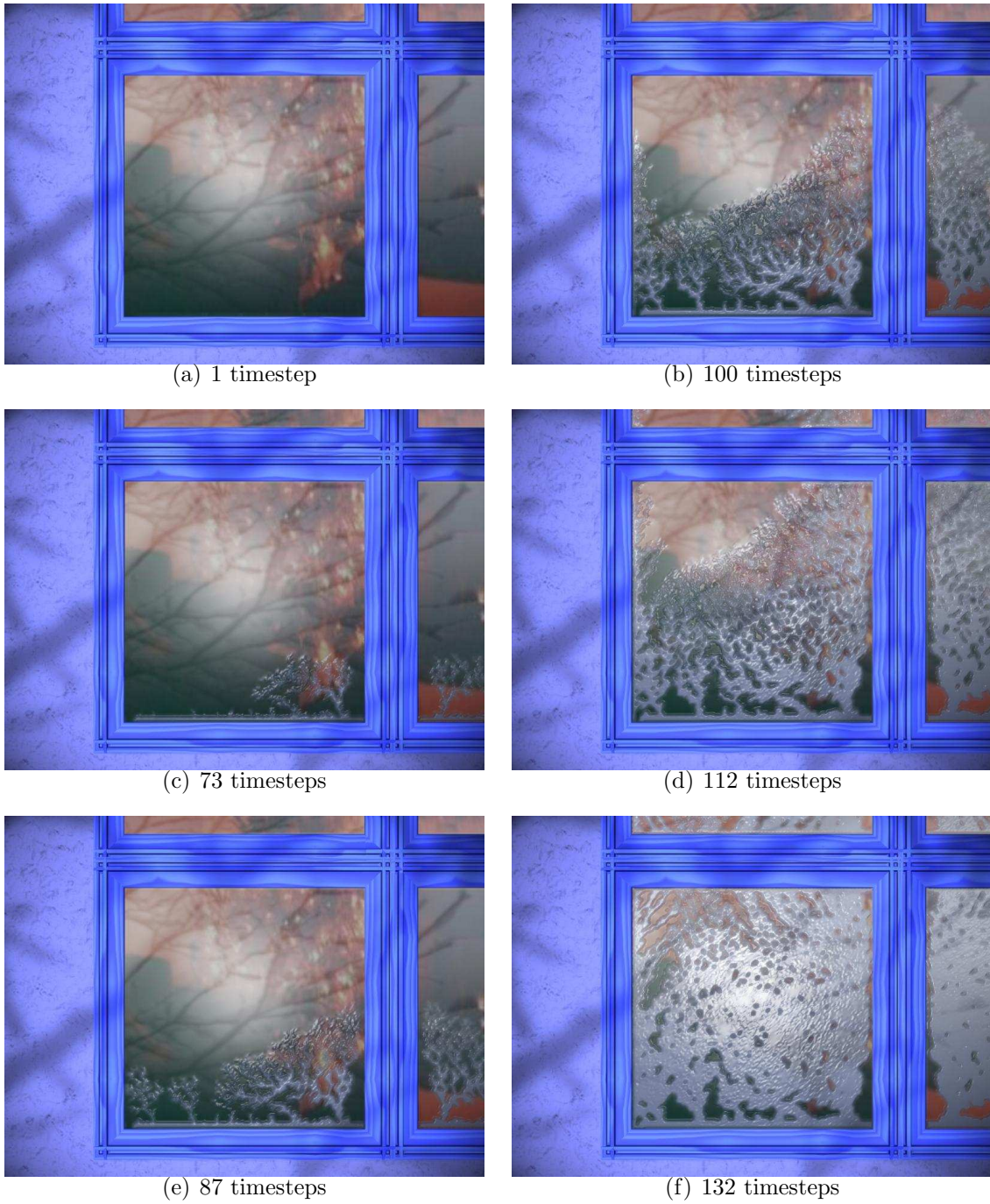


Figure 4.10: Frost forming on a window.

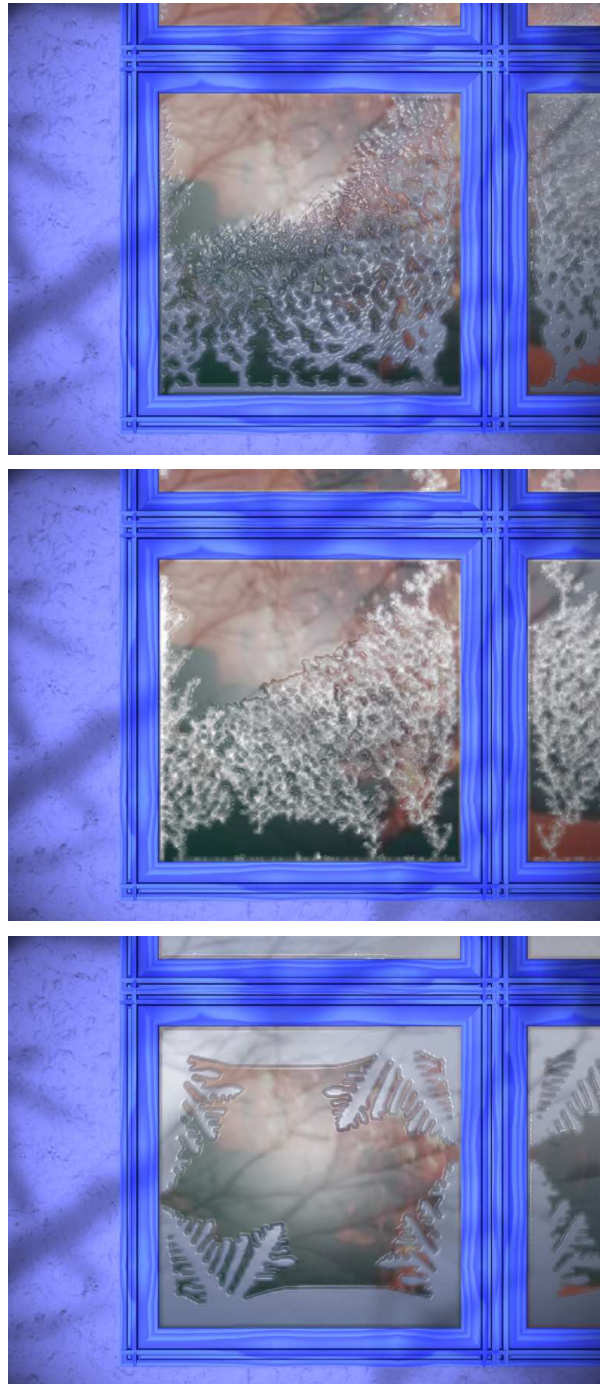


Figure 4.11: **Comparison of algorithms** Top to bottom: The hybrid algorithm; DLA only (method of (Sumner, 2001)); phase fields only (method of (Kim and Lin, 2003))



Figure 4.12: **Validation.** Top: Closeup of modified chilled glass simulation. Bottom: Photograph of ice on a chilled glass.



Figure 4.13: **Snowflake growth** We show how our algorithm can produce microscale detail, such as the arms of a snowflake. **Inset:** Photo of a real snowflake.

Chapter 5

Icicle Growth

In previous chapters I described methods of simulating frost formation using a combination of phase fields, diffusion limited aggregation (DLA), and stable fluid solvers. While these techniques work well for flat, essentially 2D formations, they do not extend naturally to 3D. Phase fields assume that the water supply in the environment is thick and plentiful. In 3D, this would only be the case for something like a freezing lake, which does not qualify as a ‘typical’ winter scene. DLA is essentially a model for vapor deposition, and produces bushy, dendritic structures in 3D that do not bear close resemblance to icicles.

However, the dense optical and geometric complexity of icicles adds appeal and authenticity to any winter scene, so modeling their dynamics is an interesting and worthwhile problem. Large icicle formations have appeared in such recent films as *The Incredibles* and *The Lion, the Witch and the Wardrobe*. In the former, the icicles were modeled as smooth, stylized cones, and in the latter, they had to be hand-molded from plaster and clay. In the absence of a computational model for solidification, realistically modeling these ice formations by hand can be a daunting task. This task becomes even more demanding if an animation of the ice forming is required, as it is unclear what the dynamics of the ice surface should be.

Extending existing graphics algorithms to faithfully simulate these dynamics is difficult, because the set of defining visual features is different. Recent research efforts have found much success in simulating fluids (see e.g. (Selle et al., 2005) and (Feldman

et al., 2005) for recent results), but these algorithms are designed to capture features such as vorticity and splashing. Freezing is instead characterized by sharp icicle tips, and the optical effects caused by surface rippling. The underlying pattern formation mechanisms are different from fluid dynamics, so different algorithms are needed. The techniques from the previous chapter dealt with small-scale, essentially 2D formations such as frost on surfaces or snowflakes. The techniques described assume that the ice crystal is surrounded by a large bath of water, and while an argument can be made that this is the case in 2D, it is clearly not the case in 3D. This makes their extension to the complex 3D cases presented in this chapter difficult.

Simulating large scale ice formation is a challenging task due to the wide range of scales involved. An interesting icicle formation is on the scale of roughly 1 meter, but the tip of an icicle is roughly 2 millimeters in radius, and a thin water film coats the ice that is on the order of tenths of a millimeter in thickness. The thin water layer drives the formation of ripples, and the optics of these ripples give ice its characteristic look. In this chapter, I present a method that captures these various multi-scale phenomena in a single unified simulation.

In previous chapters, I first described a simulation method, and then drew a connection to the Stefan problem. For the formations presented in this chapter, there does not appear to be any viable simulation method available, so I will instead derive one from the original Stefan problem. Usually the Stefan problem examines how ice forms given a virtually infinite supply of water. I am instead interested in the case encountered in a typical wintery scene, where the water supply is severely limited. Therefore, I present the ‘thin-film’ version of the Stefan problem and design a novel method for solving this problem efficiently.

Features on the ice surface frequently merge, so I have elected to use level set methods for the overall simulation (Osher and Fedkiw, 2003; Sethian, 1999). Level set methods tend to smear out small-scale features, so I describe methods of tracking these features separately. I derive an analytical solution for the dynamics of the icicle tip, as well as a curvature-dependant evolution equation for the ice far from the tip. In order

to avoid explicitly tracking a large amount of ripple geometry, I modify an analytical model from physics that poses surface ripples as a Fourier mode along the ice surface. I use this method to defer explicit instantiation of the ripple geometry to render time, which greatly simplifies the level set simulation.

5.1 The Stefan Problem

5.1.1 Background

In math and physics, solidification is usually posed as a Stefan problem. First posed by Josef Stefan (Stefan, 1889) as a model of ocean ice forming in arctic regions, the Stefan problem has since found applications in fields ranging from geology to metallurgy. The richly non-linear behavior of the problem has also attracted considerable interest in mathematics (Hill, 1987; Meirmanov, 1992). An excellent historical overview of the Stefan problem is available in (Wettlaufer, 2001).

There are only a handful of known closed form solutions to the Stefan problem, and these only apply to simple geometries. Stefan originally solved the planar case, and subsequently the case of a sphere (Frank, 1949) and a parabola (Ivantsov, 1947) were derived. These cases are often referred to eponymously as the “Frank sphere” and “Ivantsov parabola” solutions. The derivations of these solutions are available in Chapter 2, and discussed in detail by Saito (Saito, 1996). I will later base the thin film equations on these solutions.

Due to its ability to handle geometry with rapidly changing topology, level set methods have found recent success in solving the Stefan problem numerically. The method was first applied in Sethian and Strain (Sethian and Strain, 1992) as a boundary integral formulation, an alternate formulation was proposed by Chen et al. (Chen et al., 1997) and this approach was later extended to second (Gibou et al., 2003) and fourth order (Gibou and Fedkiw, 2005) accuracy. All of this work dealt with the classical Stefan problem. I am instead interested in applying level set methods to the thin film

case, because it is more appropriate for modeling ice formation in natural scenes.

5.1.2 The Classic Stefan Problem

To review from Chapter 1, Stefan problem is composed of two simple equations. Assume we have a heat field T defined continuously over some computational domain, and an initial ice/water interface Γ . The heat field evolves according to the heat equation

$$\frac{\partial T}{\partial t} = D \nabla^2 T, \quad (5.1)$$

where D denotes a diffusion constant. The ice/water interface then evolves in the normal direction according to

$$\frac{\partial \Gamma}{\partial t} \cdot \mathbf{n} = D \frac{\partial T}{\partial \mathbf{n}}, \quad (5.2)$$

where \mathbf{n} denotes the normal direction. Fluid velocity and the coefficient of expansion of ice are assumed to be negligible. Many different flavors of the Stefan problem are described in Chapter 1 that impose various boundary conditions on the heat field and interface. I select the *one-sided* Stefan problem as the most appropriate for the case of icicle growth. In this case the ice/water interface is assumed to be the freezing temperature of water, T_f , and the temperature of the fluid infinitely far from the interface is set to some undercooled temperature T_u , where $T_u < T_f$. Both of these assumptions are necessary if the crystal is to grow. If the temperature at the crystal surface were greater than T_f , phase transition would not occur, and if the temperature of the fluid were not lower than T_f , then by Eqn. 1.2, no growth would occur.

Additionally, the overall timescale in question is on the order of hours, so I assume that the heat field is essentially in equilibrium. Eqn. 5.1 then simplifies to the Laplace equation

$$\nabla^2 T = 0. \quad (5.3)$$

Note that due to the absence of a timescale, the diffusion constant D can be dropped in this case. This quasi-steady state approximation and the boundary conditions just described are used in all the existing models from glaciology (Maeno et al., 1994; Makkonen, 1988; Szilder and Lozowski, 1994) and physics (Ogawa and Furukawa, 2002; Ueno, 2003) as well.

5.1.3 The Thin Film Stefan Problem

Unlike the classic Stefan problem, I want to model the situation where a thin film of water continuously coats the outside of the ice. I assume that the crystal surface is at freezing temperature T_f , but instead of specifying the undercooled temperature T_u at some infinitely far away boundary, I specify it at a small offset δ from the interface. More formally, I specify this as

$$\Gamma + \delta(\Gamma \cdot \mathbf{n}) = T_u. \quad (5.4)$$

Using this modified boundary condition, I derive thin-film evolution equations that can be solved using level set methods.

The simplest case is an evolving planar interface. In 1D, Eqn. 5.4 simplifies to $\Gamma + \delta = T_u$. Assume that the plane is growing continually in the z direction. Within this coordinate system, we define the current position of the interface as z' . The Laplace equation at z' then integrates to:

$$T(z') = \left(\frac{T_u - T_f}{\delta} z' + T_f \right). \quad (5.5)$$

By inserting the result into Eqn. 1.2, we obtain a constant velocity for the planar case:

$$\frac{d\Gamma}{dt} = D \frac{T_u - T_f}{\delta}. \quad (5.6)$$

This planar solution matches the one obtained in (Ueno, 2003).

The cylindrical solution can be obtained in a manner similar to the classical solution described in (Hill, 1987). For the cylindrical case, we must instead solve the polar Laplace equation,

$$\frac{\partial^2 T}{\partial r^2} + \frac{1}{r} \frac{\partial T}{\partial r} = 0, \quad (5.7)$$

where r is the radial coordinate. We assume the crystal is growing in the positive r direction, and define the current interface position as r' within this coordinate system. The exact method we use to transform Γ to r' will be discussed later. The solution must be of the form:

$$T(r) = A + B \log r.$$

The thin film boundary conditions can be stated as:

$$\begin{aligned} T(r') &= T_f \\ T(r' + \delta) &= T_u. \end{aligned}$$

The constants then solve to:

$$\begin{aligned} A &= T_f - \frac{T_u - T_f}{\log \frac{r' + \delta}{r'}} \log r' \\ B &= \frac{T_u - T_f}{\log \frac{r' + \delta}{r'}} \end{aligned}$$

Applying these two constants, we obtain

$$T(r') = T_f + \frac{T_u - T_f}{\log \left(\frac{r' + \delta}{r'} \right)} (\log r - \log r'). \quad (5.8)$$

We want a velocity equation at r' , so we take the derivative of Eqn. 5.8, solve for $r = r'$, and substitute the result into Eqn. 1.2 to obtain:

$$\frac{\partial \Gamma}{\partial t} = D \frac{\partial T(r')}{\partial r} = D \frac{T_u - T_f}{r' \log\left(\frac{r'+\delta}{r'}\right)}. \quad (5.9)$$

We can obtain a similar solution for the negative curvature case. This corresponds to the case where the ice freezes radially inwards to fill in a cylindrical hole. Following steps similar to those above, we obtain

$$\frac{\partial \Gamma}{\partial t} = -D \frac{T_u - T_f}{r' \log\left(\frac{r'-\delta}{r'}\right)}. \quad (5.10)$$

Eqns. 5.9 and 5.10 can be consolidated into a single velocity equation,

$$\frac{\partial \Gamma}{\partial t} = D \frac{T_u - T_f}{|r'| \log\left(\frac{|r'|+\delta}{|r'|}\right)}. \quad (5.11)$$

This is the equation that the level set solver solves. Note this equation implicitly includes Eqn. 5.6 as well. The planar case corresponds to the case of a cylinder of infinite radius, and in the limit

$$\lim_{r' \rightarrow \infty} D \frac{T_u - T_f}{|r'| \log\left(\frac{|r'|+\delta}{|r'|}\right)} = D \frac{T_u - T_f}{\delta}, \quad (5.12)$$

the planar velocity equation is retrieved. Therefore, Eqn. 5.11 describes the interface velocity of a positive and negative cylinder, as well as a plane. Note that Eqn. 5.11 contains a singularity at $r' = 0$, but this is to be expected, as it corresponds to the spurious physical case of a cylinder with zero radius.

5.1.4 The Thin Film Ivantsov Parabola

In this section I will derive a solution to the thin-film Stefan problem for parabolic geometry. The paraboloid solution drives icicle growth, so it is crucial that it be solved accurately. From a visual simulation standpoint, correctly capturing the velocity of an icicle tip is important because it determines the overall shape of the icicle. If the velocity is too slow, we will get unconvincingly stubby icicles, and if it is too fast, we

will get equally unconvincing needles.

The experimental measurements in Maeno et al. (Maeno et al., 1994) indicate that across a wide range environmental conditions, the radius of the tip of an icicle remains fixed at approximately 2.5 mm. If we are tracking features inside a 1 meter³ cube on a regular grid, in order to resolve the tip using even an extremely coarse 4³ neighborhood, we need at least a 1600³ grid. Even then, it is unclear if numerical smearing would destroy the sharp tips.

I could use adaptive refinement to create a very fine grid around the tip, but I opt for a simpler solution. By using an analytical solution for the growing icicle tip, I can correct the signed distance function at every timestep. I am able to solve for the dynamics of the icicle tip independently because the physics only depend on three *local* factors: the curvature, the ice and air temperatures, and the size of the ‘pendant drop’ on the tip of the icicle.

In crystal growth, the Ivantsov parabola solution is often used to model the growing tip of a dendrite. I conjecture that icicles are the thin film analogs of classic Stefan problem dendrites. There are several different methods of obtaining the Ivantsov parabola solution, but I model the following thin-film derivation after the derivation given in (Saito, 1996). Assume that a parabolic crystal is growing in the z direction with a velocity V . Define a moving frame $z' = z - Vt$ so that at time t , $z' = 0$ always denotes the current position of the parabola tip. We can then define a parabolic coordinate system

$$\begin{aligned}\xi &= r - z' \\ \eta &= r + z' \\ \theta &= \arctan(x/y),\end{aligned}$$

where $r = \sqrt{x^2 + y^2 + z'^2}$. Intuitively, ξ and η each define a paraboloid in space, and their intersection forms a circle. The θ coordinate then defines a point on this circle.

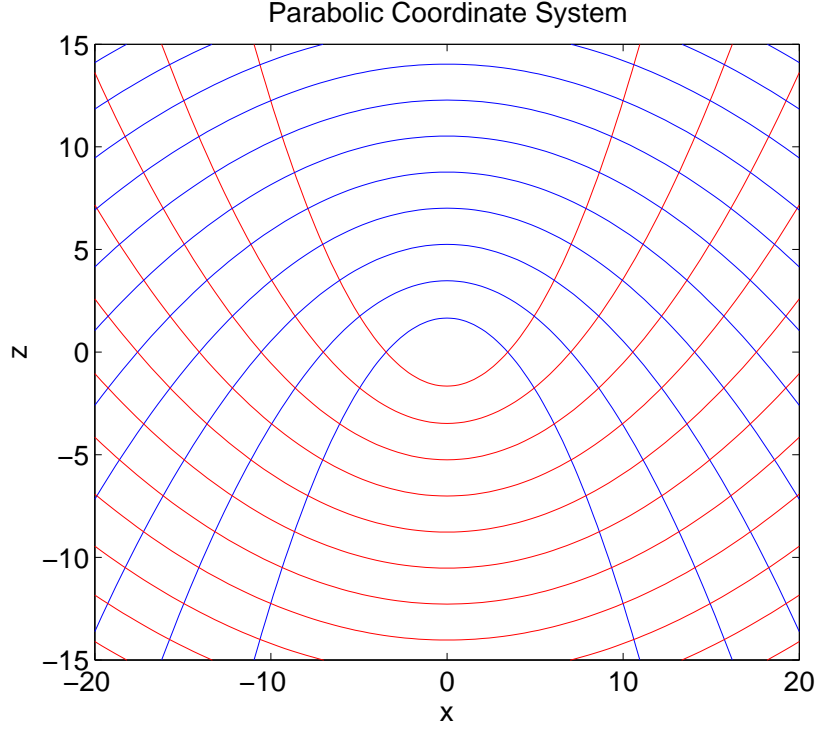


Figure 5.1: **2D slice of parabolic coordinate system:** Red lines are parabolas of constant ξ , and blue lines are constant η . Note how the distance between adjacent lines increases far from the tip.

(See Fig. 5.1.4)

The overall interface is a paraboloid η' , which is defined as the η that contains the current tip z' . The Laplace equation in parabolic coordinates becomes

$$\frac{\partial}{\partial \eta} \left(\eta \frac{\partial T}{\partial \eta} \right) + \frac{1}{l_D} \left(\eta \frac{\partial T}{\partial \eta} \right) = 0, \quad (5.13)$$

and Eqn. 1.2 simplifies to

$$\frac{\partial T}{\partial \eta} = \frac{1}{l_D}, \quad (5.14)$$

where l_D denotes the diffusion length. It appears that this equation no longer describes a velocity, but it is implicit in the l_D term. The thin film boundary conditions can then be stated as $\eta' = T_f$ and $\eta' + \delta = T_u$. Due to the parabolic coordinate system,

the second boundary condition is only meaningful near the tip. As shown in Fig. 5.1.4, the normal distance between two adjacent values of η increases as the distance from the tip increases. Therefore, far from the tip, the distance between the two will be much greater than δ . Fortunately, since we are only interested in values near the tip, far away inaccuracies are irrelevant. Similar arguments are made when using the Ivantsov parabola to approximate dendrite tips in crystal growth. In these cases, the Ivantsov parabola obviously does not correctly model the side branches on a dendrite. However, since these branches occur relatively far from the tip, the parabola is still a reasonable approximation. Using these boundary conditions, the parabolic Laplace equation integrates to

$$T(\eta) = \frac{C_p(T_u - T_f)}{L} \left(1 - \frac{\int_{\eta'}^{\eta} \frac{e^{-\frac{\eta}{l_D}}}{\eta}}{\int_{\eta'+\delta}^{\eta'} \frac{e^{-\frac{\eta}{l_D}}}{\eta}} \right). \quad (5.15)$$

where L is the latent heat, and C_p is the specific heat. Inserting this result into Eqn. 5.14, we obtain

$$\begin{aligned} \frac{C_p(T_u - T_f)}{L} &= \frac{\eta'}{l_D} e^{\frac{\eta'}{l_D}} \int_{\eta'}^{\eta'+\delta} \frac{e^{-\frac{\eta}{l_D}}}{\eta} \\ &= \frac{\eta'}{l_D} e^{\frac{\eta'}{l_D}} \left(\int_{\eta'}^{\infty} \frac{e^{-\frac{\eta}{l_D}}}{\eta} - \int_{\eta'+\delta}^{\infty} \frac{e^{-\frac{\eta}{l_D}}}{\eta} \right). \end{aligned} \quad (5.16)$$

By applying exponential integral notation $E_1(P) = \int_P^{\infty} \frac{e^{-x}}{x}$ and a change of variables using the Peclet number $P = \frac{\eta'}{l_D}$, this equation can be rewritten as

$$\frac{C_p(T_u - T_f)}{L} = P e^P \left(E_1(P) - E_1\left(P + \frac{\delta}{l_D}\right) \right). \quad (5.17)$$

Velocity can be solved for by substituting the identity $P = \frac{\eta' V}{2D}$, where V is the tip velocity and D is the thermal diffusivity. Like the classic Ivantsov parabola solution, Eqn. 5.17 is difficult to integrate explicitly, so I solve it numerically. Similar to the method used in the classic case, I first approximate $E_1(P)$ with its Puiseux series

symbol	definition	value
T_f	freezing temperature	0°C
T_u	undercooled temperature	-4.9°C
L	latent heat of fusion	$3.3 \times 10^8 \text{ J/m}^3$
D	thermal diffusion constant	$1.3 \times 10^{-7} \text{ m}^2/\text{s}$
C_p	specific heat	$4.2 \times 10^6 \text{ J/(Km}^3\text{)}$
h_0	thickness of water layer	10^{-4} m
k	wavenumber	600
n	solid over liquid thermal conductivities	3.92
ε	initial ripple amplitude	$1 \times 10^{-4} \text{ m}$
σ_r	ripple amplification rate	$5.2 \times 10^{-4} \text{ s}^{-1}$
v_p	ripple translational velocity	$-6.1 \times 10^{-7} \text{ m/s}$

Table 5.1: Symbols and values. Values are from (Ueno, 2003).

$$E_1(P) = \gamma + \ln P + \sum_{n=1}^{\infty} \frac{(-1)^n P^n}{n!n}, \quad (5.18)$$

where γ is the Euler-Mascheroni constant, and then solve for V using Newton iteration.

In contrast to Eqn. 5.17, the classic Ivantsov relation is

$$\frac{C_p(T_u - T_f)}{L} = Pe^P E_1(P),$$

so the thin film version adds an extra $E_1\left(P + \frac{\delta}{l_D}\right)$ term to account for the modified boundary condition.

5.2 A Ripple Formation Model

The equations we have presented so far will produce sharp icicle tips, and smooth features far from the tip. However, other non-smooth features occur in ice formations. This is most visible as ripples along the surface of an icicle. In this section, we present a method of simulating these features.

Until recently, the formation of these features was poorly understood. Pattern formation of this type is usually explained in terms of Mullins-Sekerka theory (Mullins

and Sekerka, 1964), but Mullins-Sekerka theory predicts the formation of patterns at all wavelengths, whereas experiments show that ice ripples only form at a wavelength of roughly 1 cm. Recently, (Ueno, 2003) showed that one of the elements of Mullins-Sekerka theory, the Gibbs-Thomson effect, does not apply in the case of ice ripple formation, and proposed an alternate formation model.

The Ueno model can be stated in one dimension as

$$u(x, t) = \epsilon e^{\sigma_r t} \sin(k(x - v_p t)), \quad (5.19)$$

where x and t are spatial and temporal coordinates, ϵ is the amplitude of the initial ripple, k is a wavenumber, and σ_r and v_p are defined as

$$\sigma_r = \frac{V}{h_0} \left(\frac{-1.5\alpha\mu Pe + \mu(36 - 1.5\alpha\mu Pe)}{36 + \alpha^2} + n\mu \frac{-0.7\alpha\mu Pe - \alpha^2 + \mu(36 - 0.7\alpha\mu Pe)}{36 + \alpha^2} \right) \quad (5.20)$$

$$v_p = -\frac{V}{\mu} \left(\frac{-0.25\alpha^2\mu Pe + \mu(6\alpha + 9\mu Pe)}{36 + \alpha^2} + n\mu \frac{6\alpha - \frac{7}{60}\alpha^2\mu Pe + \mu(6\alpha + \frac{21}{5}\mu Pe)}{36 + \alpha^2} \right). \quad (5.21)$$

Eqn. 5.19 describes a sine wave that amplifies in time according to σ_r and translates in the negative x direction with a velocity v_p . The remaining symbols are computed according to the following formulas:

$$\alpha = 2 \cot \theta \cdot h_0 k + a^2 h_0 k^3 \quad (5.22)$$

$$\mu = k h_0 \quad (5.23)$$

$$Pe = \frac{g \sin \theta h_0^4 k}{2\kappa\nu\mu} \quad (5.24)$$

$$a = \sqrt{\frac{2\gamma}{g\rho \sin \theta}}. \quad (5.25)$$

Where $\kappa = 1.3 \times 10^{-7}$ m²/s, $\nu = 1.8 \times 10^{-6}$ m²/s, $\gamma = 7.6 \times 10^{-2}$ N/m, $\rho = 10^3$ Kg/m³,

and $g = 9.8 \text{ m/s}^2$.

Intuitively, we can think of Eqn. 5.19 as a sine wave being transported along the ice surface, which amplifies in time by a factor σ_r and climbs up the length of the icicle with a velocity v_p . The representation is attractive because allows us to track just a single ‘creation time’ scalar during the simulation, and leave the instantiation of ripple geometry to the renderer.

If we use Eqn. 5.19 directly in our simulation, unnaturally symmetric ripples are obtained. This is because in the Ueno model, the translational velocity v_p is assumed to be constant. A brute force method of introducing more visual variety would be to take the derivative of Eqn. 5.19 and integrate it at every grid point, at every timestep. Such an equation would take the form:

$$\frac{dy}{dt} = \delta e^{\sigma_r t} (\sigma_r \sin(k(x - v_p t)) - k v_p \cos(k(x - v_p t))). \quad (5.26)$$

By applying a trigonometric identity, we can convert this to a Fourier mode of wavenumber k .

$$\begin{aligned} \frac{dy}{dt} = \delta e^{\sigma_r t} & ((\sigma_r \cos(k v_p t) - k v_p \sin(k v_p t)) \sin(kx) - \\ & (k v_p \cos(k v_p t) + \sigma_r \sin(k v_p t)) \cos(kx)) \end{aligned} \quad (5.27)$$

However, using this equation would impose a small timestep restriction on the simulation, and since the timescale in question is on the order of hours, I would like to avoid such a restriction.

Instead, I observe that v_p variable can be interpreted as the average translational velocity of the interface over the lifetime of the ripple. Various environmental conditions cause this average velocity to fluctuate over time, so I can imitate this physical noise using numerical noise. I elect to use an easily controlled Perlin noise with a 1 cm wavelength. At render time, each vertex does a lookup into a 3D Perlin noise function and uses it to jitter v_p . In addition to avoiding a timestep restriction, this approach also decouples the small scale detail almost entirely from the level set simulation. When

designing ice patterns, the small scale ripple details can then be tweaked without having to rerun the simulation.

5.3 A Level Set Solver

5.3.1 Background

I will now describe how to solve the equations from the previous sections using level set methods (Osher and Fedkiw, 2003; Sethian, 1999). Level set methods can simulate interfaces with rapidly changing topology by embedding the interface as an isosurface in a higher-dimensional function, which is usually a signed distance function ϕ . The function is then evolved according to the equation

$$\frac{\partial \phi}{\partial t} + \mathbf{v} \cdot \nabla \phi = 0, \quad (5.28)$$

where \mathbf{v} is some velocity field. Because the ice interface often merges, I have decided to use level set methods in this work. I specifically use the narrow band level set method (Adalsteinsson and Sethian, 1995a), where the narrow band is tracked using an unbalanced octree, much as in Losasso et al. (Losasso et al., 2004).

For the spatial derivatives, I use a fifth order Hamilton Jacobi Weighted Essentially Non-Oscillatory (HJ-WENO) scheme (Liu et al., 1996). In its simplest form, level set methods use first order upwinding to timestep the simulation. The usual method of obtaining a second order accurate derivative would be to take a weighted average of both the upwind and downwind neighbors. However, while this discretization accounts for more terms in the Taylor expansion, from a physical standpoint it is incorrect. Using downwind information to estimate what is fundamentally an upwind quantity only introduces unrelated information into the computation. Higher order methods can then be obtained by using more neighbors from the upwind direction.

Using strictly upwind neighbors can lead to problems in some cases, because if the stencil crosses a discontinuity, spuriously large derivatives can be obtained. Es-

entially Non-Oscillatory (ENO) schemes (Harten et al., 1987) are a method of detecting such discontinuities that decides when to use to upwind neighbors and when downwind neighbors will suffice. Using ENO schemes, third order accuracy can be achieved. Whereas ENO schemes select only one set of neighboring points to estimate the derivative, Weighted ENO (WENO) schemes use a weighted combination of all possible neighboring point sets. In this manner, fifth order accuracy is obtained.

In my simulations, there are substantial discontinuities in the distance field near the medial axis of the icicles. This is not a problem once the icicles have grown sufficiently thick that their derivative stencils no longer use grid cells near the medial axis, but when the icicle is initially forming, this can cause spuriously noisy results. By using a HJ-WENO scheme, these artifacts are greatly reduced.

For the time discretization, I used second order timestepping via the midpoint rule. Fluid simulation techniques in graphics usually use Total Variational Diminishing Runge Kutta (TVD-RK), but for second order accuracy TVD-RK reduces to midpoint rule. I have found that using this scheme also appears to give results that are less prone to spurious numerical noise.

In graphics, a hybrid particle level set method (Enright et al., 2002a) has recently been successful in simulating the Navier-Stokes equations because it uses Lagrangian particles to re-introduce smeared out small scale detail. In this chapter, I capture the small scale detail using alternate methods, so a basic level set solver suffices.

5.3.2 The Velocity Field

In order to evolve an existing ice interface, we must specify a velocity \mathbf{v} . I choose to approximate the interface as locally cylindrical, and use Eqn. 5.11 to compute a velocity in the normal direction. I plug the maximum principal curvature at each grid point into r' , since this describes essentially the largest osculating cylinder at that point. Sethian (Sethian, 1999) describes the following method of computing Gaussian curvature K and mean curvature H in level sets:

$$K = \frac{\phi_x^2(\phi_{yy}\phi_{zz} - \phi_{yz}^2) + \phi_y^2(\phi_{xx}\phi_{zz} - \phi_{xz}^2) + \phi_z^2(\phi_{xx}\phi_{yy} - \phi_{xy}^2)}{(\phi_x^2 + \phi_y^2 + \phi_z^2)^2} +$$

$$\frac{2(\phi_x\phi_y(\phi_{xz}\phi_{yz} - \phi_{xy}\phi_{zz}) + \phi_y\phi_z(\phi_{xy}\phi_{xz} - \phi_{yz}\phi_{xx}) + \phi_x\phi_z(\phi_{xy}\phi_{yz} - \phi_{xz}\phi_{yy}))}{(\phi_x^2 + \phi_y^2 + \phi_z^2)^2}$$

and

$$H = \frac{(\phi_{yy} + \phi_{zz})\phi_x^2 + (\phi_{xx} + \phi_{zz})\phi_y^2 + (\phi_{xx} + \phi_{zz})\phi_z^2}{(\phi_x^2 + \phi_y^2 + \phi_z^2)^2}$$

$$- \frac{2(\phi_x\phi_y\phi_{xy} + \phi_x\phi_z\phi_{xz} + \phi_y\phi_z\phi_{yz})}{(\phi_x^2 + \phi_y^2 + \phi_z^2)^2}.$$

The maximum principal curvature can then be computed as the larger root κ of the quadratic $\kappa^2 - 2H\kappa + K = 0$.

Eqn. 5.11 is only defined along the interface, whereas we require velocities over the entire narrow band. Since curvature is defined over the entire domain, I use it to compute values for Eqn. 5.11 everywhere. This approach does not seem to distort the distance field too badly, so it works well in practice.

Robust curvature information is crucial to obtaining meaningful velocities, but as curvature is a second order geometric quantity, a first order reinitialization scheme can create spurious curvature values at the interface. While curvature in level set methods can be noisy in general, first order reinitialization can produce garbage values. Trivially incorrect values can commonly occur, such as negative curvature in convex regions and vice versa.

Sethian (Sethian, 1999) describes a second order reinitialization method, but this is only second order for ϕ overall; it is still first order accurate at the interface. In order to achieve fully second order reinitialization, I use the reinitialization method described by Chopp (Chopp, 2001). Chopp achieves fully second order accurate fast marching by locally fitting a cubic interpolant over a 4^3 neighborhood at each grid point adjacent to the interface. The weights of this cubic interpolant are obtained by solving a linear system at each grid point. Fortunately, the system is insensitive

to the actual distance values, so an LU decomposition can be computed once for this system, and solving for the interpolant at each grid point only involves forward and backwards substitution. Once the weights of the interpolant have been obtained, the actual distance value is computed using Newton iteration.

5.3.3 Inserting the Icicle Tips

In section 5.1.4, I derived the velocity of a parabolic icicle tip, with the goal of tracking these small scale paraboloids separate from the level sets and using them to correct the signed distance function. I now show how to perform this correction. The equation for a translating paraboloid pointing in the negative y direction is

$$y(x, z) = \frac{x^2}{2R} + \frac{z^2}{2R} - Vt, \quad (5.29)$$

where again R is the radius of curvature, V is velocity, and t is time. I assume that the paraboloid is circularly symmetric, so we can instead solve the 2D case

$$y(x) = \frac{x^2}{2R} - Vt. \quad (5.30)$$

The squared distance from any point in space (p_x, p_y) to any point on this parabola is then defined as

$$S = (p_x - x)^2 + \left(p_y - \left(\frac{x^2}{2R} - Vt \right) \right)^2, \quad (5.31)$$

where S is the squared distance. If we want to then find the minimum distance to the parabola, we must find the zeros of the derivative of S ,

$$\frac{dS}{dx} = -2(p_x - x) - \frac{2}{R}x(p_y - Vt - \frac{x^2}{2R}). \quad (5.32)$$

I find the roots of this equation numerically. The second derivative of S is very flat around the roots of interest, making Newton-Raphson a poor choice for a solver. Fortunately, fairly tight bounds on the location of the root can be obtained, making

the bisection method viable. The bisection method only guarantees convergence over intervals that already contain the root of interest, so we need a method of providing such an interval. Since a parabola is symmetric about the y axis, we can solve for the value of the root over the positive x domain (excluding $x = 0$) without loss of generality. Observe that over this half space, Eqn. 5.32 can only have one root: the point of minimum distance. Trivially, the distance function is guaranteed to increase monotonically as x travels away from the point of minimum distance.

Therefore, if the point (p_x, p_y) is outside the parabola, i.e. if $p_y < y(p_x)$, then the root is guaranteed to be in the interval $\langle 0, p_x \rangle$. Conversely, if the point is inside the parabola, the root is guaranteed to be in the interval $\langle 0, \sqrt{2R(p_y + Vt)} \rangle$, where the positive solution is always selected from the square root.

These intervals guarantee convergence of the bisection method over any (p_x, p_y) where $p_x > 0$. However, we still require a method of computing a distance value when $p_x = 0$. For any point $(0, p_y)$, if the point is outside the parabola, the closest point will always be the tip of the parabola, from which distance value can be computed directly. If the point is inside the parabola, the tip is still the closest point if $p_y \leq R$. If $p_y > R$, we encounter a problem, as Eqn. 5.32 now has two roots: one at the point of minimum distance, and one at $x = 0$. But, if we are careful to perform the bisection method over $[\varepsilon, \sqrt{2R(p_y + Vt)}]$, where ε is some value near machine precision, then we will obtain the correct root.

Compared to a direct method such as cubic formula, the bisection method appears to perform about twice as fast, and is a good deal more robust and precise. Therefore, I prefer to use it as the distance field solution method here.

With this method, I correct the signed distance field of the level set solver. At every timestep, given the current position of a paraboloid, I compute the exact distance field values for a 4^3 neighborhood around the tip and overwrite the values in the level set distance field.

5.3.4 Tracking the Ripples

The last component of the level set solver is a ripple tracking method. In section 5.2, I described the ripples as a translating sine wave. I couple the ripple formation equation, Eqn. 5.19, to the level set solver using the time variable t .

The variable t in Eqn. 5.19 represents the length of time that a ripple has existed, not the overall time that the simulation has been running. In order to obtain this t , we need to track the creation time of each ripple. Since the icicle tips are the fastest moving features in the simulation, whenever the icicle tip solution is used to correct the signed distance function, I set the creation time in those grid cells to the current time. The initial ice front at the beginning of the simulation is given a creation time of $t = 0$.

We encounter the same problem when tracking the creation times that we did with the velocities; they are only defined along the interface. But, we need a method of ensuring that as the interface moves, the creation time moves with it. To accomplish this, we apply the method of fast extension velocities described in (Adalsteinsson and Sethian, 1999). Instead of extending a velocity off of the front, we extend the creation time. Briefly, the method copies information off the front to all possible future locations of the front. Thus, after a single timestep, the stored creation time at a point on the interface will be the same as it was at the beginning of the timestep.

5.4 Rendering

I interface the level set solver with a renderer by performing marching cubes on the distance field, and sending the triangles to 3Delight, a RenderMan implementation. The creation time information is interpolated per vertex and sent to the renderer as well. A displacement shader then computes Eqn. 5.19, applies noise to the interface velocity, and generates the ripple geometry on a per pixel basis.

Ice presents a challenging rendering scenario because refraction, reflection, and multiple scattering make up the bulk of the visual detail. The reflection and refraction com-



Figure 5.2: **Ray traced icicle star:** Icicle star with ray traced Fresnel wetness model from (Jensen et al., 1999).

ponents can be dealt with by using the two layer wetness model described in Jensen et al. (Jensen et al., 1999). The model consists of two distinct Fresnel reflections, one at the air/water interface, and one at the water/ice interface. For simplicity, I always assume that the reflection ray at the water/ice interface undergoes total internal reflection.

Even with this simplification, every eye ray that hits the ice is split into three. Each of these rays must also sample the environment map, which takes at least 64 samples to reasonably suppress noise. This means at least 192 rays must be shot for each eye ray that hits the ice surface. After paying this admittedly high computational cost, the resulting ice still looks too transparent, almost like glass. An example can be seen in Figure 5.4. The multiple scattering effects in the core need to be taken into account to increase the realism.

Accounting for the multiple scattering effects is more difficult than pure refraction, because an appropriate model does not appear to yet exist. An obvious choice is to use

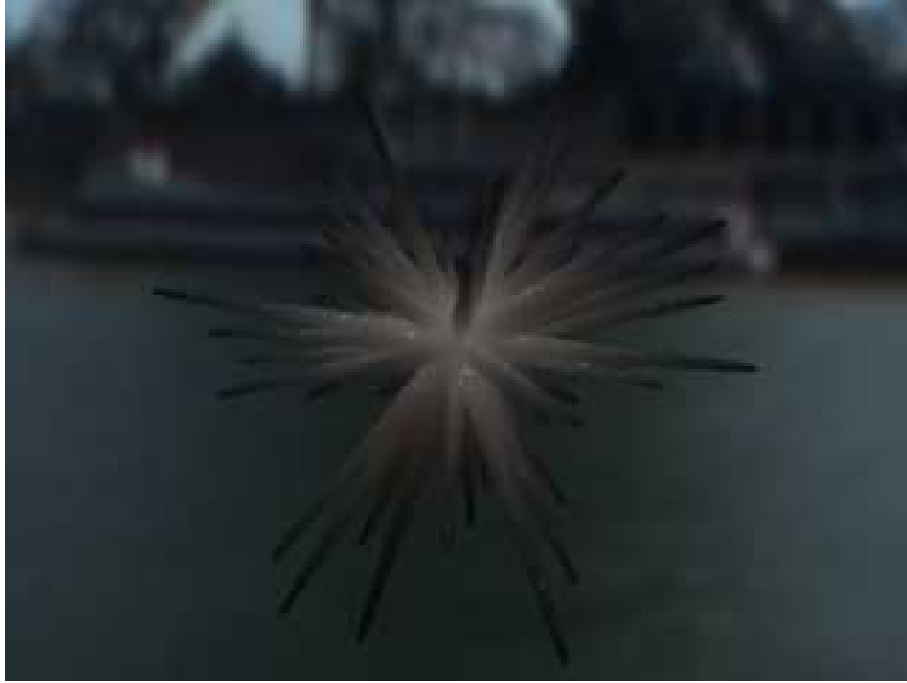


Figure 5.3: **BSSRDF icicle star:** Icicle star with only BSSRDF model from (Jensen et al., 2001a).

the dipole approximation (Jensen et al., 2001b), but this model is not well suited to ice. The model assumes that the scattering medium is fairly homogeneous, but in the case of ice, the medium varies continuously from transparent at the surface to highly scattering at the core. It appears that even the recent multi-layer work (Donner and Jensen, 2005) cannot be applied, since it handles multiple discrete scattering layers, but not a continuum. Additionally, the model dipole model approximates the surface as a semi-infinite plane, and this assumption breaks down at the sharp icicle tips.

Solving these issues rigorously is beyond the scope of this paper. Instead, I will describe a method that provides reasonable visual results. Near the root of the icicle, the medium is sufficiently thick and the curvature sufficiently flat that the dipole approximation gives visually plausible values. Near the tips, the dipole approximation returns unnaturally dark values. This artifact can be seen in Figure 5.4. Fortunately, we know that thin features usually denote newly created ice, which is nearly transparent. Therefore, I also use the dipole approximation as a blending factor between the

the multiple scattering color and the purely refracted ray color.

5.5 Results and Validation

I have used the described algorithm to simulate ice formation in several scenes, and also validated portions of the model against experimental data. The code was compiled using ICL 8, and the timings were obtained on a 3 Ghz Pentium 4. All simulations take place on a virtual 256^3 grid.

In Figure 5.7 I simulated ice forming on a fountain. The fountain was left running during a cold day, and the overflowing water froze into ice. In order to introduce visual variety into the icicles, I jittered the position of each icicle tip by 1 mm each timestep. The simulation averaged 12 seconds a timestep and completed in 30 minutes. The natural handling of merging icicles is visible in this scene, as well the straightforward handling of boundary conditions. Growth is prohibited on the inside of the fountain by merely clamping $\frac{\partial \phi}{\partial t} = 0$ on the interior of the fountain. Aside from specifying the initial growth locations, the scene was modeled with a minimum of user intervention. The icicle tips were inserted at random locations along the edge of the growing front.

In Figure 5.8 I simulated ice forming on a rooftop. The icicles were jittered by 1 mm in this case as well. The simulation averaged 2.5 seconds a timestep and completed in 5 minutes. This scene was also modeled with a minimum of user intervention. The initial growth position was specified along the rain gutter, and icicle tips were then placed at random along its length. A Halton sequence pseudo-random number generator was needed to obtain a good distribution however.

In order to demonstrate the flexibility of the model, I simulated an Andy Goldsworthy (Goldsworthy, 1990) sculpture in Figure 5.5. Mr. Goldsworthy is an artist who constructs sculptures from natural materials, in this case a star made of real icicles. This formation could not occur naturally, because gravity forces a downwards water flow. However, our model implicitly flow water in any direction by re-orienting the parabolic tips. For an animation of this ‘zero-gravity’ star growing, see the attached

video. The simulation averaged 5.1 seconds per timestep and completed in 18 minutes. Again, a minimum of user intervention was required, and icicle tips were placed along the surface of the initial sphere using a spherical Halton sequence (Wong et al., 1997).

I have not found Eqn. 5.17 elsewhere in the literature, so to test its validity we have compared it against experimental data. There is a limited amount of data available on the type of ice growth I am modelling, but Maeno et al. (Maeno et al., 1994) provides experimental data on icicle tip velocities under a range of undercoolings. In order to make a comparison to their data, I must select appropriate values for η' and δ . The η' value can be interpreted as the radius of curvature of the icicle tip. As stated earlier, experiments show that this value is 2.5 mm. The availability and stability of this value is quite fortunate, because as mentioned in Chapter 2, the Ivantsov relation can only solve for the product of the radius and velocity, not the velocity itself. Considerable research effort has gone into imposing an additional constraint that can separate these two quantities, giving rise to a so-called ‘solvability theory’. However, in the presence of a stable, experimentally observed value, I do not need to appeal to any such theory.

The value of δ on the icicle surface is usually on the order of 1×10^{-4} m, but this value represents the water thickness along the icicle wall, not at the tip. At the tip, a pendant drop forms that is roughly the same radius as the underlying crystal. Therefore, I estimate the value of δ at the tip to be 2.5 mm as well.

Fig. 5.5 shows how the predicted values compare to experimental data. I compute tip velocities over a variety of undercoolings, and compare the results to those of the classic Ivantsov relation. As stipulated by Eqn. 1.2, as the undercooling increases, the growth rate must increase as well. The classic solution predicts much slower growth and consistently undershoots the data. This is to be expected, because in the classic case, the temperature gradient at the tip has been ‘stretched’ by the infinitely far away boundary condition. While this experimental data set appears to be quite noisy, the thin-film solution appears to be in fair agreement, and I have found that it generates visually convincing results.

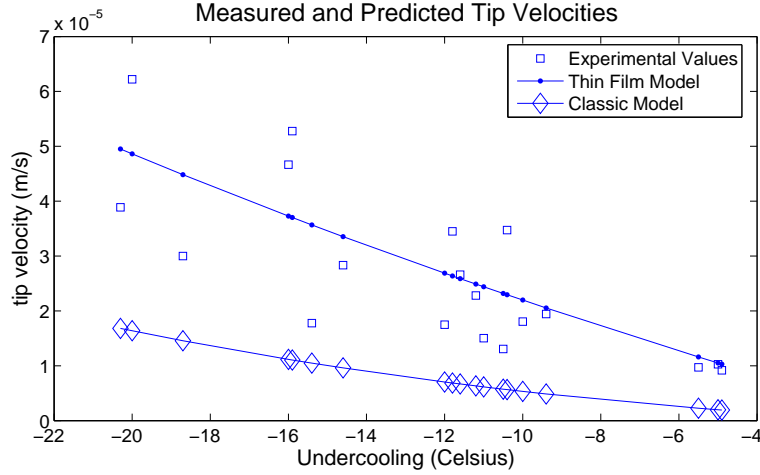


Figure 5.4: **Experimental validation:** The thin film model passes through the center of the data set, while the classic Ivantsov solution predicts much slower growth rates than those measured.

5.6 Summary

I have presented an efficient physically based method for simulating 3D ice formations that are typically found in winter scenes. The model is, to my knowledge, the most complete approach currently available. In Chapter 1, I listed the following as the main visual characteristics of icicle formation:

- Conical geometry that is much longer than it is wide,
- Automatic merging of nearby icicle roots,
- Optical effects caused by surface rippling.

In this chapter, these characteristics were captured by using the following techniques:

- A level set approach to the thin-film Stefan problem,
- An analytical solution for the tip of an icicle that appears to be in agreement with experimental data,

Run number	undercooling	velocity
8401	-5	3.7
8402	-5.5	3.5
8403	-4.9	3.3
8404	-10.4	12.5
8405	-9.4	7
8406	-10	6.5
8407	-10.5	4.7
8408	-15.9	19
8409	-16	16.8
8410	-14.6	10.2
8411	6.4	6.4
8412	22.4	22.4
8413	14	14
8414	10.8	10.8
8901	8.21	8.21
8902	12.42	12.42
8903	9.58	9.58
8904	6.3	6.3
8905	5.41	5.41

Table 5.2: Icicle growth data from (Maeno et al., 1994). Undercooling is dimensionless, and velocities are in mm/hr.

- A non-linear, curvature-driven evolution equation for the ice front far from the icicle tip,
- A method for simulating surface ripples that avoids the need to track small scale geometry in the simulation,
- A unified simulation framework for modeling complex ice dynamics.

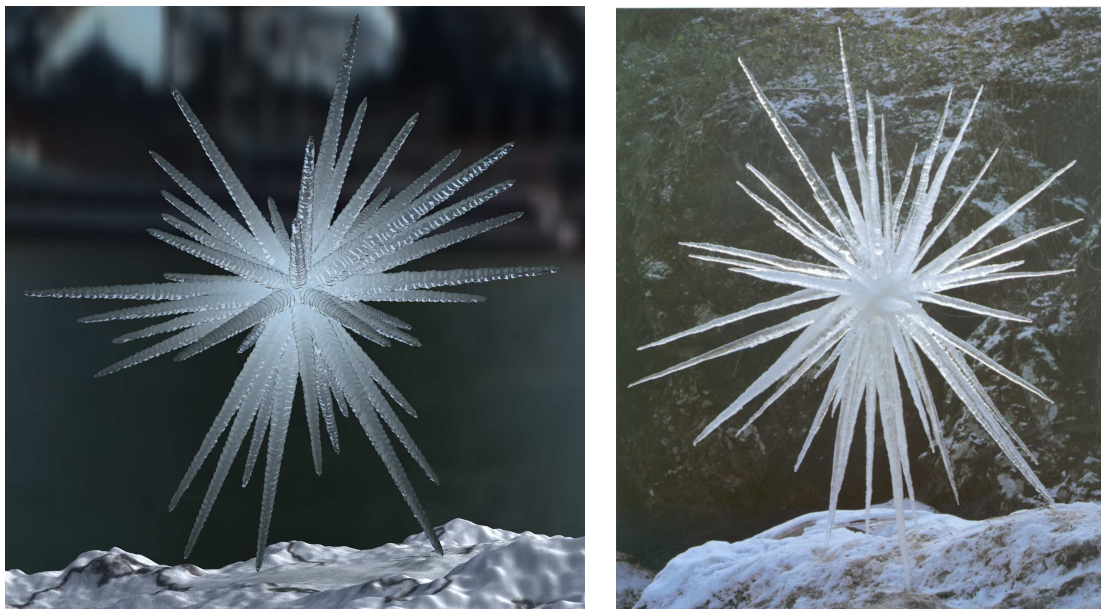


Figure 5.5: **Icicle Star:** Inspired by an Andy Goldsworthy sculpture, we simulated the growth of an icicle star. Goldsworthy is an artist who constructs sculpture from natural materials, in this case icicles. While this formation cannot occur in nature, our user controls allow such a ‘zero gravity’ star to be grown. The simulation completed in 18 minutes.

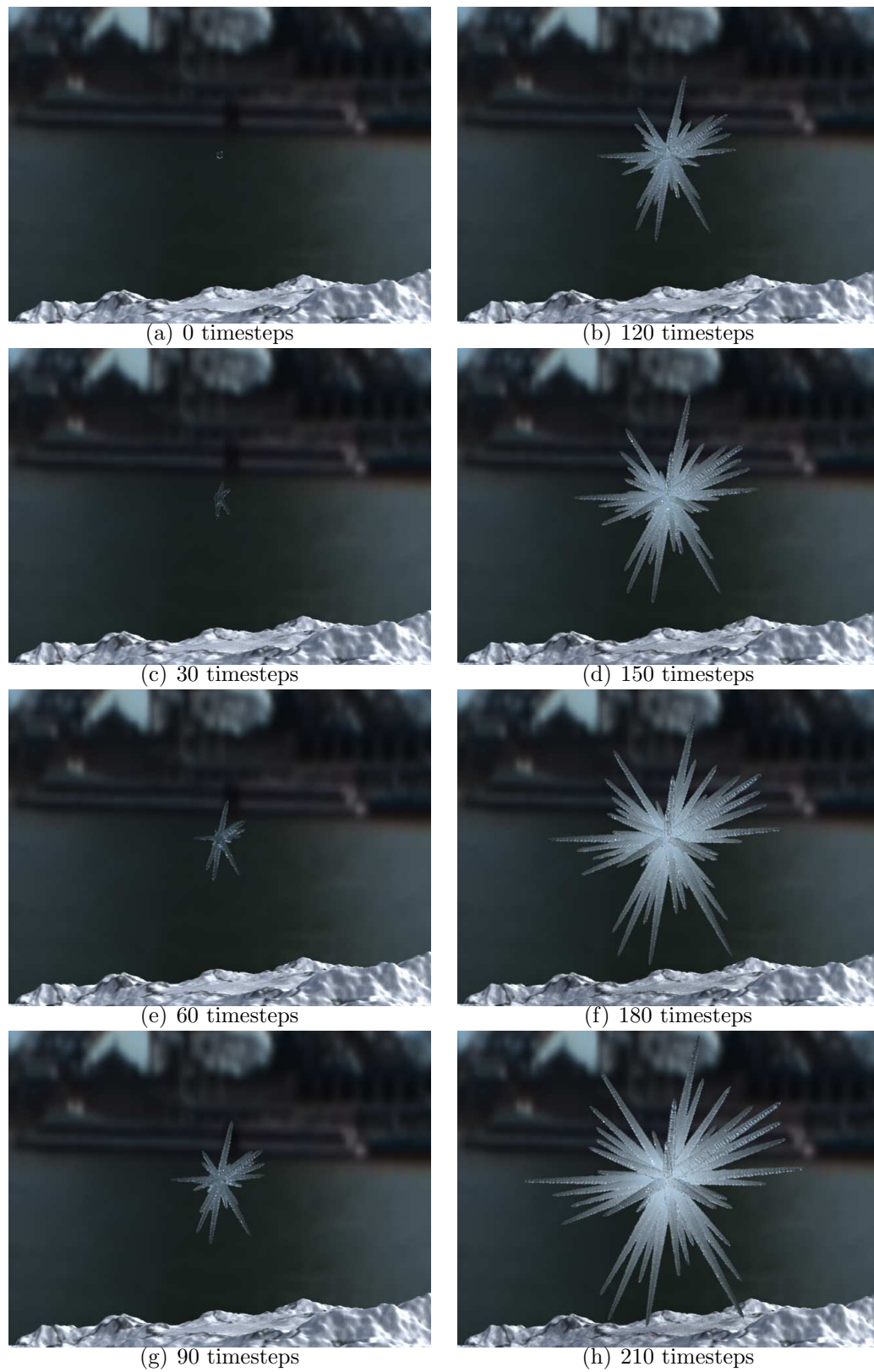


Figure 5.6: **Icicle star forming:** Frames from the icicle star forming.

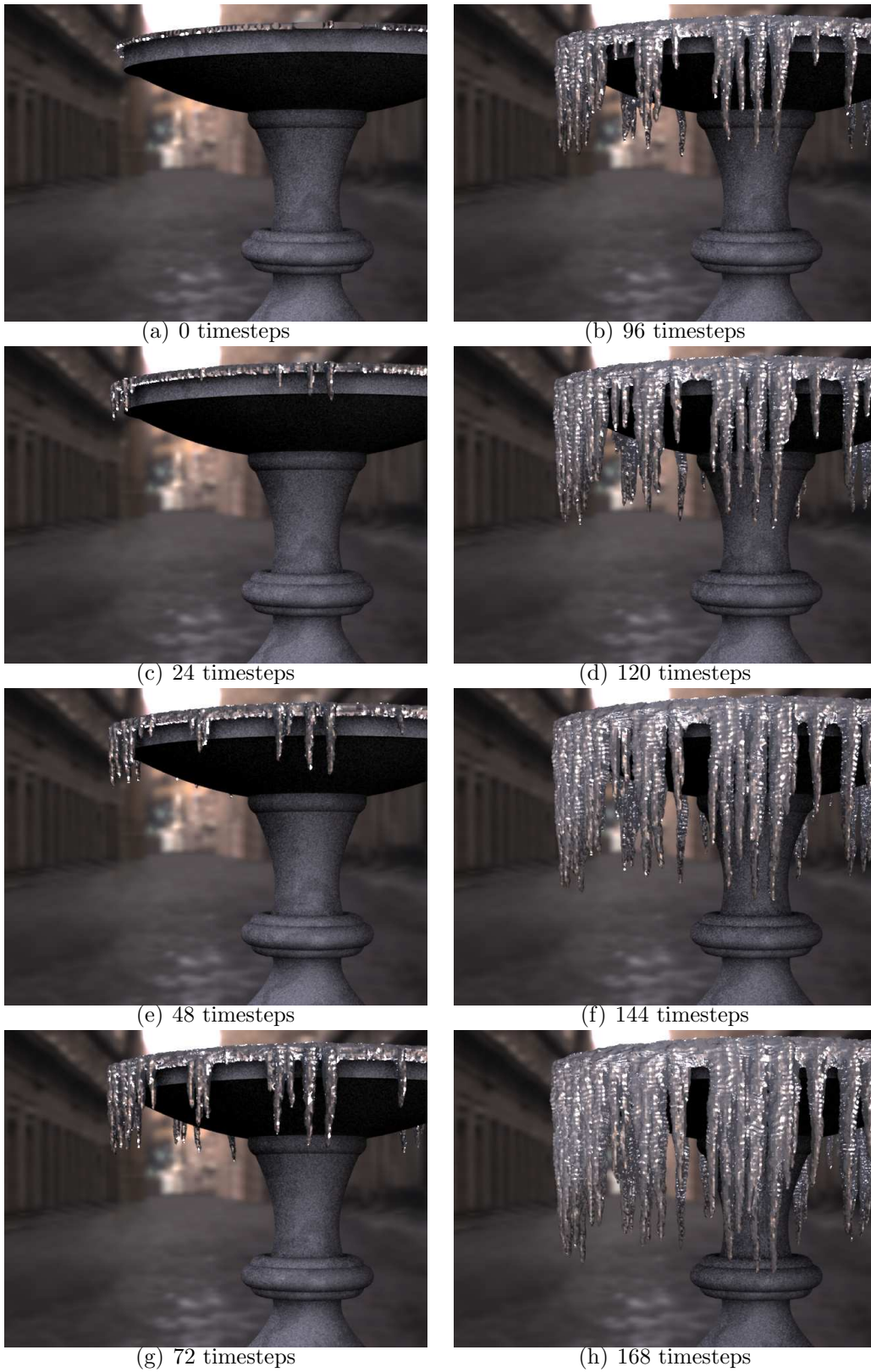


Figure 5.7: **A freezing fountain:** Ice forms in a fountain one morning when the temperature dips below freezing. This simulation completed in 30 minutes.

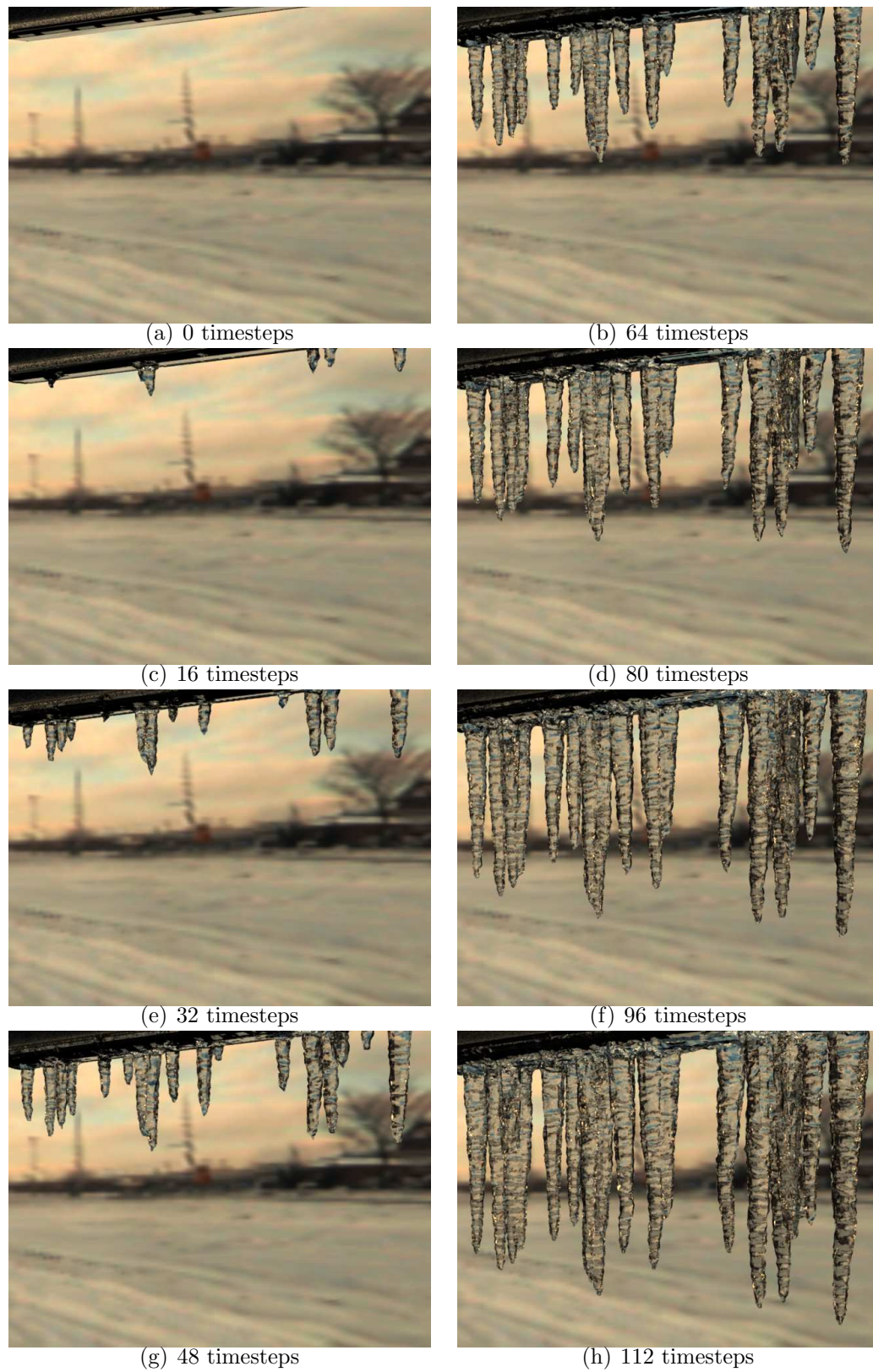


Figure 5.8: **Ice forming on a roof:** Icicles form from the snow melt running off down a roof. This simulation completed in 5 minutes.

Chapter 6

Conclusion

In this dissertation, I have presented several methods of simulating the formation of ice. A rich variety of visual phenomena arise from solidification under different physical conditions, and different methods are necessary to capture each of these situations. The methods I presented are sufficiently distinct that they require unique computational considerations, but physically, all of the approaches can be understood in the context of the Stefan problem.

6.1 Summary of Results

I have presented the phase field method in the context of visual simulation. The phase field method is derived from free energy equations, and can generate a wide variety of patterns that span both the sectorial plate and dendritic growth regimes. The phase field method is an Eulerian simulation technique that can be computationally intensive, so I have presented three optimization methods to reduce this workload. First, the phase field equations are only non-zero around the neighborhood of the ice/water interface, so computation can be restricted to a band around this interface. Second, the Eulerian simulation grid maps naturally to textures on the GPU, so the SIMD nature of the phase field simulation can be exploited by using graphics hardware. Finally, by ignoring the off-diagonal terms of the diffusion tensor in the phase field equations, the diffusion operator can be made entirely implicit, allowing larger timesteps to be taken.

The Eulerian nature of the phase field method allows it to handle topological change naturally and maps easily to the GPU. However, these advantages come at a cost, because Eulerian grids typically suffer from smoothing artifacts. I proposed two different methods of dealing with these artifacts. First, I described a physically-inspired method of introducing crease detail along the medial axis of the simulation results. Second, by examining the process of solidification, I proposed a physically-based method of integrating phase fields with a Lagrangian particle-based algorithm known as Diffusion Limited Aggregation (DLA). Lagrangian simulations can be viewed as the dual of Eulerian simulations, and suffer from the opposite problem. Whereas Eulerian simulation suffers from smoothing, Lagrangian simulation produces unnaturally sharp features. By combining the two methods, I obtained an algorithm that combines the advantages of both methods. In order to take into account the influence of wind flow in the surrounding environment, I also described a method of integrating a fluid simulation into both the phase field and DLA simulations.

Finally, I described a method of simulating the formation of icicles by phrasing the formation mechanisms as a thin-film Stefan problem. There are no existing simulation models that capture the visual characteristics of icicles, so I derived the relevant velocity equations for a level set simulation. I also described a method of simulating ripple formation that avoids tracking a large amount of small scale geometry while also avoiding additional timestep restrictions. The resulting algorithm is quite efficient, with all of the presented simulations completing in a matter of minutes.

6.2 Limitations

All of the presented simulation methods capture their respective visual characteristics effectively, but these methods also have limitations.

6.2.1 Phase Fields and DLA

Despite the optimizations presented for phase fields, they still remain fairly computationally intensive. Ideally an unconditionally stable version would be derived, allowing arbitrarily large timesteps to be taken. This is difficult due to the presence of the $\frac{\partial p}{\partial t}$ term in Eqn. 3.1. A linearization may be possible that circumvents this term. It is possible that an analytic patch such as that use in Chapter 5 may also be used on a coarse grid to track sharp features, thus reducing the computational workload. Even if an unconditionally stable scheme is derived, the large timesteps would undoubtedly introduce smoothing artifacts. Stable fluids (Stam, 1999b) suffers from vorticity damping, an issue that was addressed using a CFD technique called vorticity confinement (Fedkiw et al., 2001). A similar technique would probably need to be developed for phase fields.

As it is used in Chapter 4, DLA is restricted to have anisotropy aligned with the underlying grid. In nature, formations may display anisotropy in a local sense, but they do not appear to be aligned on any sort of global grid. In other words, while dendrites may all display six-armed anisotropy, the actual θ angles that the arms take will differ from case to case. This limitation could perhaps be dealt with by use of multiple grids with different alignments, although the additional bookkeeping would significantly complicate implementation. Recent work (Bogoyavlenskiy, 2001) describes a method of removing grid anisotropy entirely from a on-lattice DLA simulation. Once these effects have been removed, it may be possible to introduce arbitrary anisotropy functions. More work is necessary to determine if this is in fact the case.

The running time of DLA can also be problematic, as it involves a Monte Carlo step whose time complexity is difficult to bound. Alternate methods such as the dielectric breakdown model (DBM) presented in Chapter 4 or more recent conformal mapping methods (Hastings and Levitov, 1998) may offer a method of accelerating computation. Many acceleration techniques have been proposed for DLA, so incremental performance gains are available via these techniques as well. Some of these methods, such as the method of hierarchical maps (Ball and Brady, 1985), assume that the existing cluster

has been preprocessed into a tree data structure. This preprocess becomes significantly more complicated in the context of the hybrid algorithm from Chapter 4 because the phase field simulation evolves the cluster as well. A good deal of the coherence that the hierarchical maps approach assumes is therefore broken. While it may be possible for the phase field simulation to incrementally update the tree data structure, additional work is necessary to determine the specifics of such an update.

6.2.2 Icicle Simulation

The icicle growth model presented in Chapter 5 derives a good deal of its speed advantage from the fact that it does not explicitly handle the water flow over the surface of the ice. While this enables the simulation to take very large timesteps, it also limits the types of growth that the simulation can handle. In particular, the thickness of the water layer along the surface of the icicle is assumed to be constant over the lifetime of the simulation. In nature, this is not always true, and different thicknesses give rise to different visual phenomena. Icicles can shield other icicles from water flow, creating different growth conditions that could halt growth in some regions altogether. Additionally, wind forces can also influence the final shape of the icicle, stretching the profile of the icicle into a ‘blade’ shape, or curving the path of the icicle tip. It may be possible to capture these effects without introducing an explicit water simulation. From a user control standpoint, a water thickness may be assigned to each icicle tip as it is inserted, generating more visual variety. A more physically based approach would be to compute something analogous to an ambient occlusion term (Landis, 2002) for each portion of the icicle surface, and then estimate a water inflow rate based on the amount of occlusion from other icicles.

Formations analogous to stalagmites usually form beneath icicles where the pendant drop continually dripped to form a roughly conical formation. Since I do not explicitly model water flow, these formations will need additional work to capture. They do not appear to be a straightforward extension of the treatment used in Chapter 5 however, because the water supply is a steady drip, not a thin film. Visually similar ‘drip castle’

formations were presented by Carlson et al. (Carlson et al., 2002), so similar techniques can perhaps be applied to the case of ice formation as well.

There are still some ice formation phenomena that the techniques in this dissertation cannot capture. Hoarfrost is the case where frost forms in large plates that jut out from the surface of objects. This case of solidification is somewhere between the frost formations handled by phase fields and the icicle formations handled by level sets. Locally, hoarfrost is planar, but globally it is fully 3D, extending from frozen surfaces in thornlike formations. While hoarfrost is not uncommon in winter scenes, it is uncommon enough that the average viewer does not ‘expect’ to see it. A new simulation method would most likely need to be designed to handle this case, but the overall visual realism would be minimally impacted, so I chose not to address it in this dissertation.

6.2.3 Rendering Issues

A drawback of all of the methods described in this thesis is that an efficient, physically based rendering method is not currently available. While the goal of this dissertation is simulation and not rendering, the two problems are interrelated, because a full rendering solution may require additional information from the simulation. The sparkling, spectrally dispersive reflections of frost may require mesofacet information from the phase field and DLA simulations that they currently cannot resolve. While the role of microfacets in reflection (Cook and Torrance, 1982) and efficiently rendering the rainbow effects of diffraction (Stam, 1999a) have been addressed in the past, the glittering reflections off of frost are not a direct extension of either case, so additional work is necessary. I observed in Chapter 5 that the multiple scattering properties of icicles are inhomogeneous and continuously vary throughout the icicle volume. The variance of these scattering parameters are not currently tracked anywhere in the simulation, and for a full physically based rendering algorithm to be effective, this information may become necessary. The physical mechanisms that give rise to this variance in scattering are unclear however, so computing and tracking these quantities is more than a straightforward extension of the work presented here.

6.3 Future Work

Assuming the limitations described above are overcome, there still remains the problem of user interaction. In the prototype systems described in the thesis, user interaction methods were added in a fairly ad-hoc manner, essentially evolving as various workflow kinks were discovered during the production of examples. If procedural pattern generation techniques are to gain wider use in production environments, better user interaction techniques will need to be developed. Similar to rendering, fast preview of results is essential to a smooth workflow, so efficient, approximate techniques would be useful. However, guaranteeing that an approximate solution accurately captures the visual cues of a higher quality simulation poses significant challenges.

Optimization approaches to user control have recently emerged in graphics (McNamara et al., 2004), which allow the user to provide a very high level description of the desired simulation results. Most of the complexity of the simulation is abstracted away from the user, allowing novice users with only a basic understanding of the underlying physics to generate non-trivial effects. These methods have been successfully applied to smoke and water simulation, but they could potentially be applied to any of the techniques described in this dissertation. All of the techniques involve a very large set of user parameters however, many of which have yet to be thoroughly investigated. It is unclear which of these parameters are the best suited for an optimization setting.

While phase fields and fluid flow map well to graphics hardware, DLA is a serial algorithm that does not map as well to the SIMD computation model. There are results (Kaufman et al., 1995) that suggest that DLA can be parallelized, with multiple random walkers computing simultaneously. However, it is unclear how much of this computation can be parallelized before the essential fractal nature of the resulting structure is lost. It appears that this number is not fixed, and is a function of the current aggregate size. Many parallel walkers early on in the simulation will create very non-fractal results, while the same number of walkers on a larger aggregate will produce results that is perceptually indistinguishable from serial results.

While there is some work that attempts to capture phase transition between the three most common states of matter (Carlson et al., 2002; Losasso et al., 2005), the treatment of solid to liquid transition and vice versa can be somewhat ad hoc. Although the papers are somewhat sparse on details, it appears that the solid/liquid boundary advances according to a constant value, not the derivative in the normal direction that the Stefan problem dictates. Therefore, a unified, physically consistent approach that visually captures all three common states of matter and all the phase transitions in between is still a direction for future work. The problem presents additional scale disparities in both space and time, which in turn gives rise to new thermodynamic considerations. Certainly the problem of tracking a fluid layer that is tenths of a millimeter is a challenging problem within itself.

The mix of numerical and analytical techniques I used in Chapter 5 here could be adapted to visual simulation of thin film fluid flow. This is a crucial element of a solver that handles phase transitions, since transitions usually initiate as a thin layer. For example, a burning candle or a melting ice sculpture at first produces a thin, uneven liquid layer. Current techniques need a dense grid to capture the surface tension effects in this thin layer, but the techniques from Chapter 5 could potentially be used to resolve these features on a much coarser grid. The ‘drippy’ shape of a melting wax front, for example, can be viewed as a case of viscous fingering, which is a physical phenomenon closely related to the formation of icicle tips. Whereas I treat icicle tips as a case of Mullins-Sekerka instability (Mullins and Sekerka, 1964), viscous fingering is an analogous fluid case known as the Saffman-Taylor instability (Saffman and Taylor, 1958). A variant of the Ivantsov parabola could be used to explicitly capture the finger tips in this case. Additionally, a variant of the ripple formation model I used could be used to capture the rippling of a thin fluid surface running down a surface. The phenomenon is known as “Benney’s wave” (Benney, 1966), and is similar to the case of icicle rippling. The waves translate at a much faster rate than icicle ripples, and in the opposite direction. But, the wavelengths involved are quite similar, suggesting that similar techniques could be applied.

On the physics side, while Mullins-Sekerka theory predicts the formation of dendrites in an infinite bath, there is no equivalent theory for the thin film case. Such a theory would predict the locations of icicle initiation, allowing the simulation to automatically place the parabolic tips. Finally, due to the similarity between the heat and mass transfer equations, recent results (Short et al., 2005) also suggest that methods similar to the ones I used for icicle growth could be used to simulate stalactite formation.

All of the numerical techniques used in this dissertation, as well as the fundamental physics of solidification, are still active areas of research. Substantial progress has been made in understanding the mechanisms that give rise to the complex visual features of ice, but many fundamental open questions still exist. For example, the thermodynamics of fluids under shear flow, ie heat flow along the thin water layer on the surface of an icicle, is still not well understood (Jou et al., 2001). It is indeed curious that while the Stefan problem is a common mathematical thread that runs through all the techniques in this dissertation, the computational aspects of these techniques vary so widely. Perhaps as phase transition becomes better understood, all of the visual phenomena I describe in this dissertation will eventually be handled by a single, elegant, unified model. I look forward to that day.

Appendix A

Cg Implementation of Phase Fields

The following Cg code simulates both the p and T fields in the phase field equations. The p variable is packed into the red channel of the 'phaseField' texture, and the T variable is packed into the blue channel. The ε term in Eqn. 3.2 is computed in a separate program because it performs a different set of finite differences. The results are packed into the 'eField' texture.

```
//-----
// File : phaseTexture.cg
//-----
// originally written by Mark J. Harris as ReactionDiffusion.cg to support
// Grey-Scott reaction diffusion
//
// modified by Theodore Kim to support phase field simulation
//-----
// Permission to use, copy, modify, and distribute this software and its
// documentation for any purpose is hereby granted without fee, provided that
// the above copyright notice appear in all copies and that both that
// copyright notice and this permission notice appear in supporting
// documentation.
//
// The author(s) and The University of North Carolina at Chapel Hill make no
// representations about the suitability of this software for any purpose.
// It is provided "as is" without express or implied warranty.
struct v2f : vertex2fragment
{
```

```

float4 texCoord    : TEX0;
};

fragout main(v2f IN,

              // dimensions of the current window
              uniform float4      windowDims,

              // simulation parameters
              uniform float4      iceParams,

              // current timestep
              uniform float       timestep,

              // texture containing the values of  $\epsilon$ 
              uniform samplerRECT eField,

              // texture containing the phase field variables
              // the red channel is the phase variable  $\phi$ 
              // the blue channel is the heat variable  $T$ 
              uniform samplerRECT phaseField)
{
    fragout OUT;

    // get neighbors of current pixel
    float4 rightPhase = f4texRECT(phaseField, IN.texCoord + fixed2(1,0));
    float4 leftPhase  = f4texRECT(phaseField, IN.texCoord + fixed2(-1,0));
    float4 downPhase  = f4texRECT(phaseField, IN.texCoord + fixed2(0,-1));
    float4 upPhase    = f4texRECT(phaseField, IN.texCoord + fixed2(0,1));

    // get neighbors of  $\epsilon$  term

```

```

float3 leftE  = f3texRECT(eField, IN.texCoord + fixed2(-1,0));
float3 rightE = f3texRECT(eField, IN.texCoord + fixed2(1,0));
float3 downE  = f3texRECT(eField, IN.texCoord + fixed2(0,-1));
float3 upE    = f3texRECT(eField, IN.texCoord + fixed2(0,1));

// compute the off-diagonal partial derivatives
float pdydx = (rightE.z - leftE.z) * windowDims.z;
float pdxdy = (upE.y - downE.y)    * windowDims.z;

// compute the on-diagonal partial derivatives (the Hessian)
float4 centerPhase = f4texRECT(phaseField, IN.texCoord);
float4 dx = (-2.0 * centerPhase + leftPhase + rightPhase) *
            windowDims.w;
float4 dy = (-2.0 * centerPhase + upPhase + downPhase) *
            windowDims.w;
float laplacian = f1texRECT(eField, IN.texCoord) * (dx.x + dy.x);

// compute the potential (the cubic reaction term)
float m = iceParams.x *
        atan(iceParams.y * (centerPhase.z - centerPhase.y));
m = (centerPhase.z - centerPhase.y == 0.0f) ? 0.0f : m;
float potential = centerPhase.x * (1.0f - centerPhase.x) *
                (centerPhase.x - 0.5f + m);

// compute the final  $\frac{\partial p}{\partial t}$ 
float phaseDt = ((pdxdy - pdydx) + laplacian + potential) *
                iceParams.z;

// timestep the  $p$  field
OUT.col.r = centerPhase.x + phaseDt * timestep;

```

```

// timestep the $T$ field
OUT.col.g = centerPhase.y +
            ((dx.y + dy.y) + phaseDt * iceParams.w) * timestep;
OUT.col.b = centerPhase.z;

float ICE_expansion = 0.00025f;
OUT.col.a = (OUT.col.r > 0.5f) ? centerPhase.w + phaseDt * ICE_expansion :
                                centerPhase.w;

return OUT;
}

```

Because it performs a separate set of finite differences, the ε term in Eqn. 3.2 is computed in the separate program, listed here.

```

//-----
// File : eTexture.cg
//-----
// originally written by Mark J. Harris as ReactionDiffusion.cg to support
// Grey-Scott reaction diffusion
//
// modified by Theodore Kim to support phase field simulation
//-----
// Permission to use, copy, modify, distribute and sell this software and its
// documentation for any purpose is hereby granted without fee, provided that
// the above copyright notice appear in all copies and that both that
// copyright notice and this permission notice appear in supporting
// documentation.
//
// The author(s) and The University of North Carolina at Chapel Hill make no
// representations about the suitability of this software for any purpose.
// It is provided "as is" without express or implied warranty.

```



```

struct v2f : vertex2fragment
{
    float4 texCoord    : TEX0;
};

fragout main(v2f IN,
             uniform samplerRECT phaseField,
             uniform float4      windowDims,
             uniform float4      iceParams)
{
    fragout OUT;

    // get neighboring pixels
    float right = f1texRECT(phaseField, IN.texCoord + fixed2(1,0));
    float left  = f1texRECT(phaseField, IN.texCoord + fixed2(-1,0));
    float down  = f1texRECT(phaseField, IN.texCoord + fixed2(0,-1));
    float up    = f1texRECT(phaseField, IN.texCoord + fixed2(0,1));

    // compute partial derivatives
    float2 partial = float2((right - left), (up - down));
    partial *= windowDims.z;

    // compute a theta direction
    float magnitude = length(partial);
    float theta = (magnitude > 0.0f)
        ? acos(clamp(partial.x / magnitude, -1.0f, 1.0f))
        : 0.0f;
    theta = (partial.y < 0.0f) ? 2.0f * 3.1415926535897931f - theta
        : theta;

    // compute  $\epsilon$ 

```

```

float e = iceParams.x *
    (1.0f + iceParams.y *
        cos(iceParams.z * (theta - iceParams.w)));
float2 eedTheta = e * -iceParams.x * iceParams.z *
    iceParams.y *
    sin(iceParams.z * (theta - iceParams.w));
eedTheta *= partial;

// store various forms of  $\epsilon$ 
OUT.col.r = e * e;
OUT.col.g = eedTheta.x;
OUT.col.b = eedTheta.y;

return OUT;
}

```

Bibliography

- Adalsteinsson, D. and Sethian, J. (1995a). A fast level set method for propagating interfaces. *Journal of Computational Physics*, 118:pp. 269–277.
- Adalsteinsson, D. and Sethian, J. (1995b). A level set approach to a unified model for etching, deposition, and lithography, i: Two-dimensional simulations. *J. Comp, Phys.*, 120(1):128–144.
- Adalsteinsson, D. and Sethian, J. (1995c). A level set approach to a unified model for etching, deposition, and lithography, ii: Three-dimensional simulations. *J. Comp, Phys.*, 122(2):348–366.
- Adalsteinsson, D. and Sethian, J. (1997). A level set approach to a unified model for etching, deposition, and lithography, iii: Re-deposition, re-emission, surface diffusion, and complex simulations. *J. Comp, Phys.*, 138(1):193–223.
- Adalsteinsson, D. and Sethian, J. (1999). The fast construction of extension velocities in level set methods. *Journal of Computational Physics*, pages 2–22.
- Al-Rawahi, N. and Tryggvason, G. (2002). Numerical simulation of dendritic solidification with convection: Two-dimensional geometry. *Journal of Computational Physics*, 180:471–496.
- Anderson, D., McFadden, G., and Wheeler, A. (2000). A phase-field model of solidification with convection. *Physica D*, 135:175–194.
- Atkinson, K. (1989). *An Introduction to Numerical Analysis*. John Wiley & Sons.

- Ball, R. and Brady, R. (1985). Large scale lattice effect in diffusion-limited aggregation. *J. Phys. A: Math. Gen.*, 18:L809–L813.
- Baxter, W. V., Wendt, J., and Lin, M. C. (2004). IMPaSTo: A realistic model for paint. In *Proceedings of the 3rd International Symposium on Non-Photorealistic Animation and Rendering*, pages 45–56.
- Beckermann, C., Diepers, H., Steinbach, I., Karma, A., and Tong, X. (1999). Modeling melt convection in phase-field simulations of solidification. *Journal of Computational Physics*, 154:468–496.
- Ben-Jacob, E., Goldenfeld, N., Langer, J. S., and Schön, G. (1983). Dynamics of interfacial pattern formation. *Physical Review Letters*, 51:19301932.
- Ben-Jacob, E., Goldenfeld, N., Langer, J. S., and Schön, G. (1984). Boundary-layer model of pattern formation in solidification. *Physical Review A*, 29:330–340.
- Benney, D. (1966). Long waves on liquid films. *Journal of Mathematical Physics*, 45:150.
- Bentley, W. (1902). NOAA photo library. <http://www.photolib.noaa.gov/historic/nws/nwind27.htm>.
- Bentley, W. and Humphreys, W. (1962). *Snow Crystals*. Dover Publications.
- Bodenschatz, E., Imbuhl, R., and Rehberg, I. (2003). Focus on pattern formation. *New Journal of Physics*, 5.
- Bogoyavlenskiy, V. A. (2001). Mean-field diffusion-limited aggregation: A density model for viscous fingering phenomena. *Physical Review E*, 64:066303.
- Bolz, J., Farmer, I., Grinspun, E., and Schröder, P. (2003). Sparse matrix solvers on the gpu: Conjugate gradients and multigrid. *Proc. of ACM SIGGRAPH*.
- Brener, E. and Mel'nikov, V. (1991). 2-dimensional dendritic growth at arbitrary peclet number. *Adv. Phys.*

- Buka, A., Börzsonyi, T., Éber, N., and Tóth-Katona, T. (2001). Patterns in the bulk at the interface of liquid crystals. *Lecture Notes in Physics*, pages 298–318.
- Caginalp, G. and Chen, X. (1992). Phase field equations in the singular limit of sharp interface problems. In Gurtin, M. and McFadden, G., editors, *On the Evolution of Phase Boundaries*, volume 43, pages 1–27. Springer Verlag.
- Canny, J. (1986). A computational approach to edge detection. *IEEE Transactions on Pattern Analysis and Machine Intelligence*, 8(6):pp. 679–698.
- Carlson, M., Mucha, P., III, B. V. H., and Turk, G. (2002). Melting and flowing. *Proc. of ACM SIGGRAPH Symposium on Computer Animation*.
- Carlson, M., Mucha, P. J., and Turk, G. (2004). Rigid fluid: animating the interplay between rigid bodies and fluid. *ACM Trans. Graph.*, 23(3):377–384.
- Chen, S., Merriman, B., Osher, S., and Smereka, P. (1997). A simple level set method for solving stefan problems. *Journal of Computational Physics*, 135:8–29.
- Chen, Y., Xia, L., Wong, T.-T., Tong, X., Bao, H., Guo, B., and Shum, H.-Y. (2005). Visual simulation of weathering by gamma-ton tracing. *ACM Trans. Graph.*, 24(3).
- Chopp, D. (2001). Some improvements of the fast marching method. *Journal of Scientific Computing*, 23:230–244.
- Clavet, S., Beaudoin, P., and Poulin, P. (2005). Particle-based viscoelastic fluid simulation. In *Symposium on Computer Animation 2005*, pages 219–228.
- Cook, R. and Torrance, K. (1982). A reflectance model for computer graphics. *ACM Transactions on Graphics*, 1:7–24.
- Demmel, J. (1997). *Applied Numerical Linear Algebra*. SIAM.
- DeRose, T., Kass, M., and Troung, T. (1998). Subdivision surfaces in character animation. *Proc. of ACM SIGGRAPH*.

- Desbenoit, B., Galin, E., and Akkouche, S. (2004). Simulating and modeling lichen growth. *Proc. of Eurographics 2004*.
- Donner, C. and Jensen, H. W. (2005). Light diffusion in multi-layered translucent materials. *ACM Trans. Graph.*, 24(3).
- Dorsey, J. and Hanrahan, P. (1996). Modeling and rendering of metallic patinas. *Proc. of SIGGRAPH*, pages 378–396.
- Dorsey, J., Pedersen, H. K., and Hanrahan, P. (1996). Flow and changes in appearance. In *SIGGRAPH '96: Proceedings of the 23rd annual conference on Computer graphics and interactive techniques*, pages 411–420.
- Eden, M. (1961). A two dimensional growth process. In *Proceedings of the Fourth Berkeley Symposium on Mathematical Statistics and Probability*.
- Enright, D., Fedkiw, R., Ferziger, J., and Mitchell, I. (2002a). A hybrid particle level set method for improved interface capturing. *Journal of Computational Physics*, 183:83–116.
- Enright, D., Marschner, S., and Fedkiw, R. (2002b). Animation and rendering of complex water surfaces. *Proc. of SIGGRAPH*, pages pp. 736–744.
- Family, F., Platt, D. E., and Vicsek, T. (1987). Deterministic growth model of pattern formation in dendritic solidification. *Journal of Physics A*, 20:L1177–L1183.
- Fearing, P. (2000). Computer modeling of fallen snow. *Proc. of SIGGRAPH*, pages 37–46.
- Fedkiw, R., Stam, J., and Jensen, H. W. (2001). Visual simulation of smoke. *Proc. of SIGGRAPH*, pages 15–22.
- Feldman, B. E., O'Brien, J. F., and Klingner, B. M. (2005). Animating gases with hybrid meshes. In *Proceedings of ACM SIGGRAPH 2005*.

- Fix, G. (1983). Free boundary problems, theory and applications. In Fasans, A. and Primicero, M., editors, *Research Notes In Mathematics*, volume 2. Pitman.
- Foster, N. and Fedkiw, R. (2001). Practical animation of liquids. *Proc. of SIGGRAPH*, pages pp. 15–22.
- Foster, N. and Metaxas, D. (1996). Realistic animation of liquids. In *Proceedings GI '96*, pages 204–212.
- Frank, F. (1949). The influence of dislocation on crystal growth. *Disc. Faraday Soc.*, 5:48–54.
- Frank, F. C. (1974). Descartes' observations on the amsterdam snowfalls of 4, 5, 6 and 9 february 1634. *Journal of Glaciology*, 13(69):535–539.
- Galoppo, N., Govindaraju, N., Henson, M., and Manocha, D. (2005). Lu-gpu: Efficient algorithms for solving dense linear systems on graphics hardware. In *Proceedings of the ACM/IEEE SC—05 Conference*.
- Gibou, F. and Fedkiw, R. (2005). A fourth order accurate discretization for the laplace and heat equations on arbitrary domains, with applications to the stefan problem. *J. Comput. Phys.*, 202:577–601.
- Gibou, F., Fedkiw, R., Caflisch, R., and Osher, S. (2003). A level set approach for the simulation of dendritic growth. *J. Sci. Comput.*, 19:183–199.
- Goktekin, T. G., Bargteil, A. W., and O'Brien, J. F. (2004). A method for animating viscoelastic fluids. *ACM Transactions on Graphics (Proc. of ACM SIGGRAPH 2004)*, 23(3):463–468.
- Goldsworthy, A. (1990). *Andy Goldsworthy: A Collaboration with Nature*. Harry N Abrams.

- Govindaraju, N., Redon, S., Lin, M., and Manocha, D. (2003). Cullide: Interactive collision detection between complex models in large environments using graphics hardware. *ACM SIGGRAPH/Eurographics Graphics Hardware*.
- Griebel, M., Dornseifer, T., and Neunhoffer, T. (1997). *Numerical Simulation in Fluid Dynamics: A Practical Introduction*. SIAM.
- Haji-Sheikh, A. (1988). Monte carlo methods. In Minkowycz, W., Sparrow, E., Schneider, G., , and Pletcher, R., editors, *Handbook of Numerical Heat Transfer*, pages 673–723. John Wiley and Sons.
- Halperin, B., Hohenberg, P., and Ma, S. (1974). Renormalization group methods for critical dynamics. *Physical Review B*, 10:139–153.
- Harlow, F. and Welch, E. (1966). Numerical calculation of time-dependent viscous incompressible flow of fluids with free surface. *Physics of Fluids*, 8.
- Harris, M. J., Coombe, G., Scheuermann, T., and Lastra, A. (2002). Physically-based visual simulation on graphics hardware. *Proc. 2002 SIGGRAPH / Eurographics Workshop on Graphics Hardware*.
- Harten, A., Engquist, B., Osher, S., and Chakravarthy, S. (1987). Uniformly high-order accurate essentially non-oscillatory schemes iii. *Journal of Computational Physics*, 71:231–303.
- Hastings, M. (2001). Fractal to nonfractal phase transition in the dielectric breakdown model. *Physical Review Letters*, 87(17).
- Hastings, M. and Levitov, L. (1998). Laplacian growth as one-dimensional turbulence. *Physica D*, 116:244–252.
- Hill, J. M. (1987). *One-dimensional Stefan Problems: an Introduction*. John Wiley & Sons.
- Hooke, R. (1665). *Micrographia*. Dover Publications.

- Hoppe, H. (1994). *Surface reconstruction from unorganized points*. PhD thesis, University of Washington.
- Ivantsov, G. (1947). Temperature field around the spherical, cylindrical and needle-crystals which grow in supercooled melt. *Dokl Akad Nauk USSR*, 58:67.
- Jahne, B. (1997). *Digital Image Processing: Concepts, Algorithms, and Scientific Applications*. Springer Verlag.
- Jensen, H. (2001). *Realistic Image Synthesis Using Photon Mapping*. AK Peters.
- Jensen, H., Legakis, J., and Dorsey, J. (1999). Rendering of wet materials. *Rendering Techniques '99*, pages 273–282.
- Jensen, H., Marschner, S., Levoy, M., and Hanrahan, P. (2001a). A practical model for subsurface light transport. *Proceedings of SIGGRAPH 2001*.
- Jensen, H., Marschner, S., Levoy, M., and Hanrahan, P. (2001b). A practical model for subsurface light transport. *Proceedings of SIGGRAPH 2001*, pages 511–518.
- Jones, M. and Chen, M. (1994). A new approach to the construction of surfaces from contour data. *Computer Graphics Forum*, 13(3):pp. 75–84.
- Jou, D., Casas-Vázquez, J., and Criado-Sancho, M. (2001). *Thermodynamics of Fluids Under Flow*. Springer-Verlag.
- Kass, M. and Miller, G. (1990). Rapid, stable fluid dynamics for computer graphics. In *Proceedings of SIGGRAPH 1990*, pages 49–57.
- Kaufman, H., Vespignani, A., Mandelbrot, B., and Woog, L. (1995). Parallel diffusion-limited aggregation. *Physical Review E*, 52:5602–5609.
- Kepler, J. (1611). *The Six-Cornered Snowflake*. Oxford Univ. Press. Translated by L. L. Whyte, 1966.

- Kharitonsky, D. and Gonczarowski, J. (1993). A physically based model for icicle growth. *The Visual Computer*, pages 88–100.
- Kim, T. and Lin, M. (2003). Visual simulation of ice crystal growth. *Proc. of ACM SIGGRAPH / Eurographics Symposium on Computer Animation*.
- Kim, T. and Lin, M. (2004). Physically based modeling and rendering of lightning. *Proc. of Pacific Graphics 2004*.
- Kobayashi, R. (1993). Modeling and numerical simulations of dendritic crystal growth. *Physica D*, 63:pp. 410–423.
- Landis, H. (2002). Production-ready global illumination. In *Siggraph course notes #16*.
- Langer, J. S. (1986). Models of pattern formation in first-order phase transitions. In Grinstein, G. and Mazenko, G., editors, *Directions in Condensed Matter Physics*, pages 165–186. World Scientific.
- Langer, M. S., Zhang, L., Klein, A., Bhatia, A., Pereira, J., and Rekhi, D. (2004). A spectral-particle hybrid method for rendering falling snow. In *Rendering Techniques 2004: Eurographics Symposium on Rendering*, pages 217–226.
- Liu, X., Osher, S., and Chan, T. (1996). Weighted essentially non-oscillatory schemes. *Journal of Computational Physics*, 126:202–212.
- Losasso, F., Gibou, F., and Fedkiw, R. (2004). Simulating water and smoke with an octree data structure. *Proc. of SIGGRAPH*, pages 457–462.
- Losasso, F., Irving, G., Guendelman, E., and Fedkiw, R. (2005). Melting and burning solids into liquids and solids. *IEEE TVCG*.
- Maeno, N., Makkonen, L., Nishimura, K., Kosugi, K., and Takahashi, T. (1994). Growth rates of icicles. *Journal of Glaciology*, 40:319–326.
- Makkonen, L. (1988). A model of icicle growth. *Journal of Glaciology*, pages 64–70.

- Malladi, R., Sethian, J., and Vemuri, B. (1995). Shape modeling with front propagation: A level set approach. *IEEE Trans. on Pattern Analysis and Machine Intelligence*, 17(2).
- Mandelbrot, B. (1982). *The Fractal Geometry of Nature*. W H Freeman.
- Mandelbrot, B. and Evertsz, C. (1990). The potential distribution around growing fractal clusters. *Nature*, 348:L143–L145.
- McNamara, A., Treuille, A., Popovic, Z., and Stam, J. (2004). Fluid control using the adjoint method. *ACM Transactions on Graphics*, 23(3):449–456.
- Meakin, P. (1983). Diffusion-controlled cluster formation in two, three, and four dimensions. *Physical Review A*, 27:604–607.
- Meirmanov, A. (1992). *The Stefan problem*. W. De Gruyter expositions in mathematics.
- Messinger, B. (1953). Equilibrium temperature of an unheated icing surface as a function of air speed. *J. Aero. Sci.*, pages 29–42.
- Mullins, W. and Sekerka, R. (1964). Stability of a planar interface during solidification of a dilute binary alloy. *Journal of Applied Physics*, 35(2):444–451.
- Myers, T. and Hammond, D. (1999). Ice and water film growth from incoming supercooled droplets. *International Journal of Heat and Mass Transfer*, 42:PP2233–2242.
- Nagatani, T. and Sagués, F. (1991). Morphological changes in convection-diffusion-limited deposition. *Physical Review A*, 43:2970–2976.
- Nakaya, U. (1954). *Snow Crystals, Natural and Artificial*. Harvard University Press.
- Niemeyer, L., Pietronero, L., and Wiesmann, H. J. (1984). Fractal dimension of dielectric breakdown. *Physical Review Letters*, 52:1033–1036.

- Nishita, T., Iwasaki, H., Dobashi, Y., and Nakamae, E. (1997). A modeling and rendering method for snow by using metaballs. *Computer Graphics Forum*, 16(3):357–364.
- Nittmann, J. and Stanley, H. E. (1987). Non-deterministic approach to anisotropic growth patterns with continuously tunable morphology: the fractal properties of some real snowflakes. *Journal of Physics A*, 20:L1185–L1191.
- Ogawa, N. and Furukawa, Y. (2002). Surface instability of icicles. *Physical Review E*, 66:041202.
- Osher, S. and Fedkiw, R. (2003). *Level Set Methods and Dynamic Implicit Surfaces*. Springer Verlag.
- Osher, S. and Sethian, J. (1988). Fronts propagating with curvature-dependent speed: Algorithms based on hamilton–jacobi formulations. *Journal of Computational Physics*, 79:12–49.
- Plapp, M. and Karma, A. (2000). Multiscale finite-difference-diffusion-monte-carlo method for simulating dendritic solidification. *Journal of Computational Physics*, p. 165:592–619.
- Provatas, N., Goldenfeld, N., and Dantzig, J. (1999). Adaptive mesh refinement computation of solidification microstructures using dynamic data structures. *Journal of Computational Physics*, 148:p. 265.
- Rasmussen, N., Enright, D., Nguyen, D., Marino, S., Sumner, N., Geiger, W., Hoon, S., and Fedkiw, R. (2004). Directable photorealistic liquids. In *SCA '04: Proceedings of the 2004 ACM SIGGRAPH/Eurographics symposium on Computer animation*, pages 193–202.
- Rebelo, L., Debenedetti, P., and Sastry, S. (1998). Singularity-free interpretation of the thermodynamics of supercooled water ii. *Journal of Chemical Physics*, 109(2):pp. 626–633.

- Roberts, A. and Knackstedt, M. (1993). Growth in non-laplacian fields. *Physical Review E*, 47:2724–2728.
- Runions, A., Fuhrer, M., Lane, B., Federl, P., Rolland-Lagan, A., and Prusinkiewicz, P. (2005). Modeling and visualization of leaf venation patterns. *ACM Trans. Graph.*, 24:702–711.
- Saad, Y. (2003). *Iterative Methods For Sparse Linear Systems*. SIAM.
- Saffman, P. and Taylor, G. (1958). The penetration of a fluid into a porous medium or hele-shaw cell containing a more viscous liquid. *Proceedings of the Royal Society of London, Serial A*, 245:312–329.
- Saito, Y. (1996). *Statistical Physics of Crystal Growth*. World Scientific.
- Sander, L. (2000). Diffusion limited aggregation: A kinetic critical phenomenon? *Contemporary Physics*, 41(4):203–218.
- Selle, A., Rasmussen, N., and Fedkiw, R. (2005). A vortex particle method for smoke, water and explosions. In *Proceedings of ACM SIGGRAPH 2005*, pages 910–914.
- Sethian, J. (1999). *Level Set Methods and Fast Marching Methods*. Cambridge University Press.
- Sethian, J. and Strain, J. (1992). Crystal growth and dendritic solidification. *J. Comput. Phys.*, 98:231–253.
- Shewchuk, J. R. (1994). An introduction to the conjugate gradient method without the agonizing pain. Technical report, Carnegie Mellon University.
- Shewchuk, J. R. (1996). Triangle: Engineering a 2D Quality Mesh Generator and Delaunay Triangulator. In Lin, M. C. and Manocha, D., editors, *Applied Computational Geometry: Towards Geometric Engineering*, volume 1148 of *Lecture Notes in Computer Science*, pages 203–222. Springer-Verlag. From the First ACM Workshop on Applied Computational Geometry.

- Short, M. B., Baygents, J. C., Beck, J. W., Stone, D. A., III, R. S. T., and Goldstein, R. E. (2005). Stalactite growth as a free-boundary problem: A geometric law and its platonic ideal. *Physical Review Letters*, 94(1):018501.
- Stam, J. (1999a). Diffraction shaders. In *SIGGRAPH '99: Proceedings of the 26th annual conference on Computer graphics and interactive techniques*, pages 101–110.
- Stam, J. (1999b). Stable fluids. *Proc. of SIGGRAPH*, pages 121–128.
- Stefan, J. (1889). Über einige probleme der theorie der wärmeleitung. *Sitzungsberichte de Mathematisch- Naturawissenschaftlichen Classe der Kaiserlichen, Akademie der Wissenschaften*, 98:473–84.
- Sud, A., Otaduy, M. A., and Manocha, D. (2004). Difi: Fast 3d distance field computation using graphics hardware. 23.
- Sumner, R. (2001). Pattern formation in lichen. Master’s thesis, Massachusetts Institute of Technology.
- Szilder, K. and Lozowski, E. (1994). An analytical model of icicle growth. *Annals of Glaciology*, 19:141–145.
- Touissaint, J.-C., Debierre, J.-M., and c Turban, L. (1992). Deposition of particles in a two-dimensional lattice gas flow. *Physical Review Letters*, 68:2027–2030.
- Trefethen, L. and Bau, D. (1997). *Numerical Linear Algebra*. SIAM.
- Turing, A. (1952). The chemical basis of morphogenesis. *Philosophical Transactions of the Royal Society B*, 237:37–72.
- Turk, G. (1991). Generating textures on arbitrary surfaces using reaction-diffusion. *Proc. of SIGGRAPH*, pages 289–298.
- Ueno, K. (2003). Pattern formation in crystal growth under parabolic shear flow. *Physical Review E*, 68:021603.

- Ueno, K. (2004). Pattern formation in crystal growth under parabolic shear flow ii. *Physical Review E*, 69:051604.
- Vicsek, T. (1984). Pattern formation in diffusion-limited aggregation. *Physical Review Letters*, 53:2281–2284.
- von Koch, H. (1906). Une méthode géométrique élémentaire pour l'étude de certaines questions de la théorie des courbes planes. *Acta Mathematica*, 30:pp. 145–174.
- Wei, X., Li, W., and Kaufman, A. (2003). Interactive melting and flowing of viscous volumes. *Proceedings of Computer Animation and Social Agents 2003*.
- Wettlaufer, J. (2001). *The Stefan Problem: Polar Exploration and the mathematics of moving boundaries*. Styria Verlag.
- Witkin, A. and Kass, M. (1991). Reaction-diffusion textures. *Proc. of SIGGRAPH*, pages pp. 299–308.
- Witten, T. and Sander, L. (1981). Diffusion-limited aggregation, a kinetic critical phenomenon. *Physical Review Letters*, 47(19):pp. 1400–1403.
- Wong, T.-T., Luk, W.-S., and Heng, P.-A. (1997). Sampling with hammersley and halton points. *Journal of Graphics Tools*.
- Yokoyama, E. and Kuroda, T. (1990). Pattern formation in growth of snow crystals occurring in the surface kinetic process and the diffusion process. *Physical Review A*, page p. 41.